Experimental study of the kinetics of two systems : DNA complexation by the NCp7 protein and probe dynamics in a glassy colloidal suspension

Piotr Klajner

UNIVERSITÉ DE STRASBOURG

ÉCOLE DOCTORALE DE PHYSIQUE ET CHIMIE-PHYSIQUE

Institut de Physique et Chimie des Matériaux de Strasbourg

THÈSE

présentée par :

Piotr Marek KLAJNER

soutenue le : **11 05 2011**

pour obtenir le grade de : **Docteur de l'université de Strasbourg**

Discipline/ Spécialité : Physique et Chimie-Physique

Experimental study of the kinetics of two systems: DNA complexation by the NCp7 protein and probe dynamics in a glassy colloidal suspension

---

THÈSE dirigée par :
  M. MÜNCH Jean-Pierre   Professeur, Université de Strasbourg
  M. HÉBRAUD Pascal   Chargé de Recherche, CNRS-Université de Strasbourg

RAPPORTEURS :
  M. CHATENAY Didier   Directeur de Recherches, CNRS-ENS
  M. FREYSSINGEAS Eric   Maitre de Conférence, ENS de Lyon

AUTRES MEMBRES DU JURY :
  M. TUREK Philippe   Professeur, Université de Strasbourg

Abstract

In the first part of this thesis, we study the kinetics of the complexation of a double-stranded DNA by NCp7 protein. To do this, we study the evolution of mechanical properties of DNA and its complexation by stretching the DNA/NCp7 complex with a optical trap. We observed that the persistence length of the complex decreases progressively during the complexation. Using a statistical model we describe the evolution of the flexibility of DNA complexed with NCp7. Our main result is that the fraction ϕ of base pairs that have reacted is not a linear function of time at low ϕ. We interpret our results assuming that the adsorption of NCp7 on DNA is highly cooperative. In the second chapter, we describe the dynamics of probe particles in a colloidal glassy suspension of Laponite. Laponite is a colloidal discoidal particle of 25 nm in diameter and 0.92 nm thick. We take advantage of evanescent wave microscopy, and follow the movement of fluorescent latex particles. Then we image these particles. We show that for a movement that has a single characteristic time scale, it is simply a linear function of time. We find that, whatever their size, the motion of probe particles can be described by a succession of two dynamic modes, where the fastest mode corresponds to the diffusion of particles in a viscoelastic fluid.

Dans la première partie de cette thèse, nous étudions la cinétique de la complexation d'un double brin d'ADN par la protéine NCp7. Pour ce faire, nous étudions l'évolution des propriétés mécaniques de l'ADN au fur et mesure de sa complexation, en étirant la complexe ADN/NCp7 l'aide d'un montage de piégeage optique. Nous avons observé que la longueur de persistance du complexe diminue au fur et mesure de la complexation. En utilisant un modèle statistique décrivant l'évolution de la flexibilité de l'ADN complexé par NCp7. Notre principal résultat est que la fraction ϕ de paires de bases ayant réagi n'est pas une fonction linéaire du temps aux faibles ϕ. Nous interprétons nos résultats en supposant que l'adsorption de NCp7 sur l'ADN est fortement coopérative. Dans

deuxième chapitre, nous décrivons la dynamique de particules sondes dans une suspension vitreuse colloïdale de Laponite. La Laponite est une particule colloïdale discoïdale de 25 nm de diamètre et de 0.92 nm d'épaisseur. Nous utilisons une expérience de microscopie en onde évanescente, et suivons le mouvement de particules fluorescentes de latex. Nous imageons ensuite ces particules. Nous montrons que, pour un mouvement possédant une seule échelle de temps caractéristique, elle est simplement une fonction linéaire du temps. Nous obtenons que, quelle que soit leur taille, le mouvement des particules sondes peut tre décrit par une succession de deux modes dynamiques, où le mode le plus rapide correspond la diffusion des particules dans un fluide viscoélastique.

To my Parents, Sabina and Stanisław Klajner

Acknowledgements

First of all I would like to pay my deepest thank to my PhD advisors: Jean-Pierre Münch and Pascal Hébraud, for the support they provided. You both helped me to solve scientific problems and fight with French administration when needed. Many thanks for that you encouraged me to come to Strasbourg and to begin this thesis, which turned out to be one of the most challenging adventures so far... Let me reveal my special appreciation for Pascal's patience and enormous help in completing that project.

I am also grateful to my close friends: Vinka and Ninka Faramarzi, Fuchao Jia, Mouhamad Khalil, thanks to whom my faith in people is still strong and steadfast.

Another uncountable debt of thanks is due to my Polish friends: Marta, Jacek, Matylda, and Agata Arabski, Beata and Marek Basta, Rafał Jasiak, Paweł Machała, Marzena Materska, Patrycja Polińska, Filip Schleicher, Wojciech Szewc, Łukasz Zosiak, whose presence around me helped to avoid a homesickness and did not let me forget the mother tongue in a foreign country. Connected by the same choice of place to live or work, we spent together many moments discussing, helping each other or just having fun.

I thank all my colleagues from Strasbourg for making my life much more pleasant with simple "Bonjour" and warm smile every morning. Guys, I will miss our small talks at 10:00 with a delicious cup of espresso.

My thanks are equally addressed to people who I have a great pleasure to work with: Soulaimane Kaloun, Jean-Pierre Vola, Stefan Haacke, Samy Boukari, Sebastien Harlepp, and Paul-Antoine Hervieux. Thank you for your help and nice cooperation.

I would like to thank Ralf Bundschuh and Richard Fishel and his group from the Ohio State University for listening to the alpha version of my thesis presentation and giving me important comments.

Let me also express my gratitude to my Mom—Sabina, Dad—Stanislaw and Sister—Gosia for their never-ending help and support.

At the end I would like to thank my marvelous Wife, Marcelinka, for continuously pushing me towards finishing the thesis and never losing the faith in me. I am very grateful for all you have given me in my life.

Short Contents

Contents

Preface

In this thesis we study the dynamics of two systems:

* ⋆ the complexation of DNA and a nucleocapsid protein NCp7,

* ⋆ the dynamics of the probe particles in the colloidal suspension of Laponite in its glassy phase.

NCp7 is a nucleocapsid protein of an HIV-1 virus, and is a component of Gag polyprotein. It has a chaperone protein activity in various stages of the cycle of infection by HIV. Specifically, its role is to facilitate the rearrangement of nucleic acid sequences to their most stable conformations. NCp7 is a small protein of 55 amino acids that contains two zinc finger of CCHC type that are essential to retroviral replication.

In the first part of this thesis we study the kinetics of the complexation of a double-stranded DNA by NCp7. To do this, we study the evolution of mechanical properties of DNA as a measure of its complexation by stretching the complex of DNA/NCp7 using an optical trap setup. We observed that the persistence length of the complex decreases proportionally to the complexation.

Using a statistical model describing the evolution of flexibility of DNA complexed with NCp7. From measurement of the persistence length, we deduce the fraction of base pairs of DNA having reacted with NCp7.

In the second part of the thesis we study the soft glasses that are intrinsically non-equilibrium systems, whose dynamics is slowed in a disordered phase. The description of their dynamics is extremely complex, and long relaxation times that are associated characterize the occurrence of dynamic heterogeneities.

We describe the dynamics of probe particles in a glassy colloidal suspension of Laponite. Laponite is a discoidal colloidal particle of 25 nm in diameter and 0.92 nm thick. We prepare a suspension of Laponite in which we disperse a small fraction of fluorescent latex particles of diameter 20 nm to 100 nm.

We use an evanescent wave microscopy experiment and follow the movement of fluorescent latex particles. Then we image these particles. To characterize their movement, we create a binary image and then define a time correlation function at time t as the

fraction of pixels in which a particle has remained imaged in the time interval $[0, t]$. So defined, the correlation function does not take into account the reappearance of the image of a particle in a given pixel. For this reason, the correlation function is decreasing by definition and is used to describe fluctuations defined with low statistics. We show that for a movement having a single characteristic time scale, it is simply a linear function of time.

Part I

DNA complexation by the NCp7 protein

Chapter 1

Introduction

1.1 DNA, RNA, viruses and NCp7

We are interested in the interaction between the NCp7 protein and DNA. This protein plays a role in the viral infection by HIV.

In the introductory part I give a general overview of DNA, RNA and viruses—their structure and physical properties.

1.1.1 DNA, RNA

All living cells on Earth, without any known exception, store their hereditary information in the universal language of deoxyribonucleic acid (DNA) sequences. The monomers are strung together in a long linear sequence that encodes the genetic information.

Structure

DNA is built from simple subunits, called *nucleotides*, each consisting of a sugar-phosphate molecule with a nitrogen-containing sidegroup, called base, attached to it (Fig. 1.1A). The bases are of four types (adenine, guanine, cytosine and thymine), corresponding to four distinct nucleotides, labeled A, G, C and T. A single strand of DNA consists of nucleotides joined together by sugar-phosphate linkages (Fig. 1.1B). Note that the individual sugar-phosphate units are asymmetric, giving the backbone of the strand

The graph was removed because of copyright restrictions.

Figure 1.1: **(A)** Building block of DNA. **(B)** DNA strand. **(C)** Templated polymerization of new strand. **(D)** Double-stranded DNA. **(E)** DNA double helix. [52]

a definite directionality, or polarity. A DNA molecule is highly negatively charged. Through templated polymerization (Fig. 1.1C), the sequence of nucleotides in an existing DNA strand controls the sequence in which nucleotides are joined together in a new DNA strand; T in one strand pairs with A in the other and G in one strand with C in the other. The new strand has a nucleotide sequence complementary to that of the old strand and a backbone with opposite directionality, i.e. GTAA... of the original strand and ... TTAC in complementary one. Normally DNA molecule consists of two complementary strands (Fig. 1.1D). The two strands twist around each other forming a double helix (Fig. 1.1E)—a strong structure that can accommodate any sequence of nucleotides without changing its basic structure.

The chemical structures of DNA and RNA are very similar. There are two differences—RNA contains the sugar ribose instead of DNA's deoxyribose, so a type of ribose that lacks one oxygen atom, making the DNA less susceptible to hydrolysis. The second difference is that the RNA has the base uracil (U) while DNA contains thymine (T), which have similar base-pairing properties. Unlike DNA, most RNA molecules are single-stranded. Single-stranded RNA molecules adopt very complex three-dimensional structures, since they are not restricted to the repetitive double-helical form of double-

stranded DNA. RNA is made within living cells by RNA polymerases, enzymes that act to copy a DNA or RNA template into a new RNA strand through processes known as transcription or RNA replication, respectively. [48]

Physical properties

The physical structure of double-stranded DNA is determined by the fact that its character is amphiphilic. [43] That means that one part of DNA chain (the phosphate backbone) is hydrophilic and another one (bases) is hydrophobic. Along with the flexibility of backbone, this amphiphilic character is a cause of double-helical structure of DNA. Double-stranded DNA occurs as a ladder which is twisted around its axis right-handed. The diameter of such twisted double-helix is 2.37 nm. [43] The twisting angle between adjacent base pairs is 34.6° and the distance between two neighbor nucleotides is 0.33 nm. Number of base pairs coincided with the full twist (360°) of DNA double-helix is $\simeq$ 10.4. [43] That full twist repeats itself in every 3.4 nm (Figure 1.2). Between two molecules of deoxyribose attached to complementary base pairs, there is a space creating grooves, which go along the whole DNA chain. Both of the N-glycosidic bonds connecting deoxyribose with base pairs are on the same side of double helix. Therefore the size of the grooves is not identical. They are 0.22 nm or 0.12 nm wide and are called major and minor groove, respectively. [3]

DNA in solution is not rigid but is continually changing its conformation due to the thermal fluctuations. Therefore, the bending stiffness of DNA is measured by the persistence length. It is defined as the distance over which the direction of a polymer segment persists, in the time or ensemble average, owing to limited flexibility of the polymer. It means the length of the DNA along which a thermally excited bend of 1 radian typically occurs (the DNA is essentially straight over shorter distances). For DNA the persistence length is $\simeq$ 50 nm ($\simeq$ 150 bp). This value is larger than the persistence length of synthesized polymers: DNA is referred to as semi-flexible. The flexibility of DNA is due to the fact that the covalent P-O (phosphate-oxygen) bonds can freely rotate around, so adjacent PO^- and deoxyribose rings can rotate freely. DNA chain may be described with the Worm-Like Chain model (WLC). [49]

The graph was removed because of copyright restrictions.

Figure 1.2: Physical structure of DNA.

1.1.2   Viruses

General information

Viruses are parasitic agents literally, having the same basic structure. They consist of a core of nucleic acid surrounded by protein. They can not reproduce on their own, they reproduce themselves in the cells, often with disastrous results to the host organism. They have no metabolic systems of their own, but rather depend on the mechanism of synthesis of a living host cell, by which the viruses exploit normal cellular metabolism by provide their own genetic information, namely, the nucleic acid in the host cell. Accepts the host cell nucleic acid products and components to manufacture new viruses, according to the genetic information it contains. The viruses infect bacteria (bacteriophages), plants, animals and humans.

Individual viruses contain only one type of nucleic acid, DNA or RNA. The DNA or RNA genome can be linear or circular and single- or double-stranded. A single-stranded

nucleic acid can have plus or minus polarity. RNA-based viruses are called retroviruses, because they are duplicated in a host cell using the reverse transcriptase enzyme to produce DNA from its RNA genome.

Almost all of the viruses code protein sheath or capsid, containing the nucleic acid and determining their antigenicity. The capsid is composed of a few molecules of different proteins repeatedly called capsomeres. In some viruses, specialized enzymes are stored in the capsid.

Many animal viruses form an envelope around the capsid molecules rich in proteins, lipids and glycoproteins. Although some elements of the envelope are derived from the host cell membrane, the envelope contains proteins derived from viral genes as well.

The graph was removed because of copyright restrictions.

Figure 1.3: Different kinds of viruses. [47]

A virus infection can be considered as a set of instructions, similarly to a computer program. A computer's operation is followed the instructions in its operating program, not unlike a cell is directed by DNA-coded instructions. A new program can be introduced into the computer that causes changes in its tasks and transfer all its energy into another activity, such as making copies of the introduced program. The new program is not able to make copies of itself when it is outside the computer. The introduced program, like a virus, is simply a set of instructions.

Similarly, viruses can reproduce themselves only when they enter cells and use the cellular machinery of their hosts. Viruses encode their genes on a single type of nucleic acid, DNA or RNA, but viruses need ribosomes and enzymes for protein synthesis. Viruses are able to reproduce because their genes are translated into proteins by the genetic machinery of the cell. These proteins lead to the production of copies of virus

called viral replication.

At the first stage, when the virus encounters a cell, it adsorbs to specific receptors on the cell surface with either the capsid or in enveloped viruses, using envelope proteins. Then, the penetration by viruses and intracellular release of nucleic acid occurs. Uncoating involves the release of the nucleic acid of the capsid and is apparently activated by cellular enzymes, possibly with a contribution of cell membranes as well. Next a proliferation of viral components takes place: the virus-encoded protein synthesis and capsid noncapsid, replication of nucleic acid by viral and cellular enzymes. Finally, all of the replicated nucleic acid and protein capsid is new after a release of progeny virus from the cell.

Replication

Various processes are observed for the types and configurations of the viral genome.

The replication of viral DNA into DNA-virus takes place in the cell nucleus. Some of them have their own replicases. The smaller ones, that do not have any information for their own DNA polymerase, encode polypeptides that modify cellular polymerases so that DNA sequences are mainly replicated.

Since eukaryotic cells do not possess the enzymes RNA replication, RNA viruses should provide the RNA-dependent RNA polymerase (called replicase) which is thus in all cases of virus-encoded proteins and, in some cases, are the components of the viral particle.

In the single-stranded RNA viruses, the complementary strands of the genome are produced first, then transcribed into daughter strands. They therefore show the same polarity as the viral genome and are used in the assembly of new viral progeny.

The genome of the double-stranded RNA consists of several segments of dsRNA. A translatable sense-strand RNA functions, first, as the mRNA and later as a matrix for the synthesis of antisense-strand RNA. An RNA-dependent RNA polymerase is part of the viral particle.

The genome of retroviruses consists of two segments of single stranded RNA and is transcribed by an enzyme in the virion (reverse transcriptase) into complementary DNA. 1.4 DNA is made up to make double-stranded DNA and integrated into the genome of the cell. Transcription into sense-strand of RNA is the basis for both mRNA

The graph was removed because of copyright restrictions.

Figure 1.4: Flow of information from RNA to DNA in retroviruses. [50]

and viral genomic RNA in the viral progeny.

Host response

Cell death occurs eventually as a consequence of an infection with many viral species. The destruction of cells usually involves the production of viral progeny. Virus production associated with cell death, called "lytic viral life cycle", is the reason (along the immunological phenomena) for which the disease manifests itself in the organism. Viral replication directly results in the destruction of cells in the infection process called necrosis (cytocidal infection).

The apoptosis is observed when the virus triggers a cascade of cellular events leading to cell death in most cases, breaking the cycle of viral replication.

In case of non-cytocidal infection, viral replication does not destroy the host cell, but can be destroyed by secondary immunological reactions.

Latent infection occurs when the viral genome is inside the cell, resulting in neither viral replication nor cell destruction.

Viral infection can transform the host cell into a cancer cell, that viral replication may or may not occur depending on the virus and /or cell type involved.

HIV and AIDS

The virus causes a disease, acquired immunodeficiency syndrome (AIDS) and was reported first time in the United States in 1981. It was not long before the infectious agent, a retrovirus called human immunodeficiency virus (HIV) was identified in the laboratories in France and the United States. Study revealed that HIV is a virus closely related to the chimpanzee virus, which suggests a recent host expansion to humans from chimpanzees in Central Africa.

Infected humans have decreased resistance to infection and almost all of them eventually die from diseases not serious for uninfected individuals. Rarely those who contract AIDS survive longer than a few years untreated. Transmission of HIV from an infected person to healthy one occurs by transfer of body fluids, such as blood, semen, or vaginal fluid, or the use of non-sterile needles, between infected and healthy individuals poses a severe risk. In addition, HIV-infected mothers can pass the virus on to their unborn children during fetal development.

The incidence of AIDS is growing rapidly in the United States. It is estimated that more than 33 million people worldwide are infected with HIV. Many, perhaps all of them, will eventually die with AIDS. Over 16 million people have already died since the outbreak of the epidemic. The incidence of AIDS is already high in many African countries and is growing by 20% worldwide.

How HIV weakens the immune system

In normal individuals, specialized cells guard the bloodstream, attacking and destroying any invading bacteria or viruses. In AIDS patients, this army of defenders is defeated. One special kind of white blood cell, called a CD4+ T cell is required to rouse the defending cells to action. In AIDS patients, the virus homes in the CD4+ T cells, infecting and killing them until none are left.

Without these crucial cells of the immune system, the body can not conduct a defense against invading bacteria or viruses. AIDS patients die of infections that a healthy person could fight off.

Clinical symptoms do not usually begin to develop after a long latency period, usually 8 to 10 years after initial infection with HIV. Meanwhile, HIV carriers have no clinical symptoms, but are apparently very infectious, which makes the spread of HIV very

difficult to control. The reason why HIV remains hidden for so long seems to be that its cycle of infection continues for the 8- to 10-year latent period without doing serious harm to the infected person. Eventually, however, a random mutational event in the virus allows it to quickly overcome the immune defense, starting AIDS.

The graph was removed because of copyright restrictions.

Figure 1.5: HIV structure. [45]

The cycle of HIV infection

Human immunodeficiency virus (HIV, see Fig. 1.6) is a retrovirus—a kind of a virus belonging to the RNA viruses group, which transfers its genetic information from RNA to DNA and not from DNA to RNA. 1.4 HIV causes acquired immunodeficiency syndrome (AIDS), which is a lethal disease. It can mutate very rapidly (65 times more frequently than an influenza virus). During the infection the retroviral reverse transcriptase enzyme synthesizes double-stranded DNA (dsDNA) being the copy of RNA of the virus, which integrates with the genome of a host and works as a matrix to replicate the virus and express its genes. Figure 1.7 shows typical life cycle of the HIV retrovirus.

The HIV virus infects and eliminate the essential cells if the immune system, destroying the body's ability to defend itself against cancer and infections.

⋆ Attachment

When HIV is introduced into the bloodstream of humans, the virus particle that circulates throughout the body but only infect CD4 + cells. Each particle has an HIV glycoprotein (called gp120) on its surface a protein that precisely fits a cell-surface marker protein called CD4 on the surfaces of immune system cells called macrophages and T cells. Macrophages are infected first.

The graph was removed because of copyright restrictions.

Figure 1.6: HIV structure. [45]

⋆ Entry into macrophages

After docking onto the CD4 receptor of macrophage, HIV requires a second macrophage receptor, called CCR5, to push through the cell membrane. After gp120 binds to CD4, it goes through a conformational change that allows it to bind to CCR5. This suggests that after the conformational change, the second receiver passes the gp120-CD4 complex through the cell membrane, which triggers the content of the HIV virus into the cell by endocytosis.

⋆ Replication

Once inside the macrophage, the HIV particle takes off its protective coat. This releases virus RNA floating in the cytoplasm, with a reverse transcriptase stored also within the shell of the virus. The enzyme synthesizes a double strand of DNA complementary to RNA of the virus, often making mistakes and so that introducing the mutations. This double stranded DNA directs the host cell machinery to produce many copies of the virus. HIV does not rupture and kill the cells of macrophage it infects.

Instead, new viruses are released from the cell by exocytosis. HIV summarizes a large number of viruses in this manner, a challenge to the immune system during a period of years.

⋆ Entry into T cells

Meanwhile, HIV continues to replicate and mutate. Finally, by chance, HIV alters the gene for gp120 in a manner that causes the gp120 protein to change its second-receptor submission. This new form of gp120 protein prefers to bind instead to

a different second receptor (CXCR4) a receptor that occurs on the surface of T lymphocyte CD4+ cells. Then, within a short time, T cells of the body become infected by HIV. This has deadly consequences, as new viruses leave the cell by disrupting the cell membrane, killing the infected T cell. Thus, the transition to the second receptor CXCR4 is rapidly followed by a sharp drop in the number of T cells This destruction of T cells blocks the body's immune response and leads directly to the onset of AIDS, cancers and opportunistic infections free to invade the defenseless body.

The graph was removed because of copyright restrictions.

Figure 1.7: Life cycle of the HIV retrovirus.

The future of HIV treatment

New discoveries about how HIV works continue to fuel research on fight against HIV. For example, scientists are testing drugs and vaccines that act on receptors of HIV, research on the possibility of blocking CCR5 and looking for defects in the structure of receptors of HIV among people who are infected with HIV but have not developed AIDS.

⋆ Combined treatment

A variety of drugs inhibit HIV in laboratories. These include AZT and its analogues (which inhibit the replication of the virus nucleic acid) and protease in-

hibitors (which inhibit the cleavage of the large polyprotein encoded by *gag*, *pol* and *env* genes into functional capsid, enzyme and envelope segments.

A variety of combination therapy does not really seem to be able to eliminate HIV from the body. Although the virus disappears from the bloodstream, its traces can still be detected in the lymph tissue of patients. When combination therapy is stopped, virus level in the blood again increases. Because of request therapy schedules and many side effects, long-term combination therapy does not appear to be a promising approach.

⋆ The use of a defective gene to fight against HIV/AIDS

In subsequent research, a defect was found in one of nine genes in the strain of HIV. This gene is called *nef* (negative factor) and the defective version of the *nef* in HIV appears to be missing some pieces. Viruses with the defective gene may have reduced reproductive capacity, allowing the immune system to keep the virus in check. A potential application of this discovery is its use in the development of drugs that inhibit HIV proteins responsible for the virus replication speed. It seems that the protein produced by the *nef* gene is one of these critical HIV proteins with defective forms of *nef* and does reproduce itself. Research is currently underway to develop a drug that targets the *nef* protein.

⋆ Chemokines

In the laboratory, chemicals called chemokines appear to inhibit HIV infection by binding to and blocking the co-receptors CCR5 and CXCR4. People infected with HIV for a long time who have not contracted AIDS prove to have high levels of chemokines in their blood.

The search for HIV-inhibiting chemokines is intensive. However not all of the results are promising. Researchers report that in their tests, the levels of chemokines were not different between patients whose disease was not progressing and those in whom it was rapidly progressing.

The function of chemokines is to attract white blood cells to infected areas. Chemokines work in small quantities and in local areas, but chemokines in mass numbers can cause inflammation which is worse than the initial infection. Injections of chemokines can inhibit the ability of the immune system to respond to local chemokine, or may even cause the rupture of the inflammatory response control. Thus, scientists warn that injecting chemokines could make patients more suscep-

tible to infections and they continue to research other methods of using chemokines to treat AIDS.

1.1.3 Nucleocapsid

Combination of a genome and a protein coat is called nucleocapsid (NC). Most part of the retrovirus's genome contains three genes called *gag*, *pol* and *env* (see Fig. 1.8), which contain information needed to make the structural proteins for new virus particles—*gag* codes capsid proteins, *pol* codes enzymes engaged in virus replication and *env* codes proteins occurring in lipid coat of a virus.

LTR	*gag*	*pol*	*env*	LTR
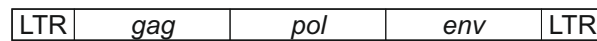
Figure 1.8: Retrovirus genome. [48]

The NC protein, being a part of Gag polyprotein, plays the role of the nucleic acid chaperone in many stages of viral infection. [33] It means that that it facilitates the rearrangement of nucleic acids into conformations containing the maximum number of complementary base pairs—they are more stable than the original structure. This ability is of crucial importance in the life cycle of the retrovirus, [22] because it stimulates the two strand transfers required for reverse transcription.

HIV-1 nucleocapsid protein (NCp7, see Fig. 1.9) is a small (55 amino acids, 7 kDa), highly positively charged protein, which is necessary for HIV-1 replication and is a promising drug target [33]. It contains two CCHC-type zinc fingers (see Fig. 1.10), which are essential to perform retroviral replication.

Characterization of the structure, properties and functions of this protein is of wide interest. [54] Many groups all over the world are investigating the possibility to use NC as a target in HIV-1 chemotherapy. [33]

1.2 Characterization of nucleic acid/NC interactions

The interaction of the DNA with the ligands is very important to fundamental intracellular processes, e.g. DNA replication, transcription or the regulation of gene expression. Small molecules may bind DNA either covalently (irreversible process), or non-covalently

The graph was removed because of copyright restrictions.

Figure 1.9: 3D model of NCp7 protein.
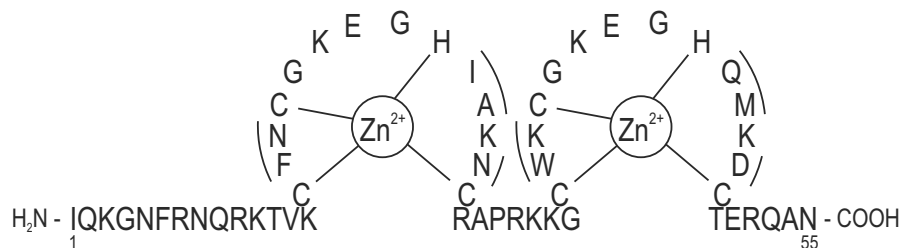
Figure 1.10: (A) Amino acid sequence and two-zinc-finger structure of HIV-1 NC (pNL4–3 isolate, GenBank accession no. AF324493). Differences between the two zinc-finger motifs are indicated by a solid curved line. [24]

(reversible process). NC facilitates annealing by destabilizing the RNA secondary structure via preferential binding of its zinc fingers to ssRNA and by inducing short-ranged attraction between nucleic acid molecules. [42]

The interaction between NCs and nucleic acids induce a structural change of nucleic acids macromolecules (either RNA or DNA). This interaction thus modifies the mechanical properties of the macromolecule itself. Here, I will show that the measurement of the mechanical properties of nucleic acid/nucleocapsid protein allows to characterize both the thermodynamic quantities of the interaction and the structural changes induced by the complexation.

Like other retroviral NCs, HIV-1 NC is a multifunctional protein. It binds nucleic acids non-specifically through electrostatic interactions of the basic residues with the phosphodiester backbone of nucleic acids and also exhibits sequence-specific binding to runs of Gs or T/UGs through interactions that involve the zinc fingers (reviewed in ref. 3). Importantly, NC is a nucleic acid chaperone, which means that it facilitates remod-

eling of nucleic acid structures to form the most thermodynamically stable conformations. [42] As the protein concentration is increased, NC stimulates strand transfer. [40]

1.2.1   Force-extension measurements of DNA molecules

Force-extension of DNA macromolecule

The unique helical structure formed by two intertwined and base-paired strands determines its elastic behavior.

At low forces, the main contribution to the elastic response is of entropic origin. Indeed, keeping the DNA at a fixed end-to-end distance, one forbids a tremendous number of conformations, lowering the entropy of the DNA molecule. The further one pulls, the more conformational states are forbidden and hence the higher this entropic force is. The force required to stretch the molecule increases dramatically.

At high forces, a transition occurs and the conformation of the dsDNA changes from the double helix to a ladder. During this transition, DNA gains almost a factor two in length without the need to pull harder. These regimes and the highly nonlinear elasticity of double-stranded DNA are shown on Figure 1.11, when the force versus the extension is measured for a single DNA molecule. [46]

The graph was removed because of copyright restrictions.

Figure 1.11: Force-extension curves for single molecules of dsDNA (red triangles) and ssDNA (right black line). A theoretical curve for dsDNA is shown as the left black line. The overstretching transition appears to be a transition from dsDNA to ssDNA. [46]

When the DNA is (almost) pulled tight, the length of the DNA contour starts to increase by stretching the DNA backbone. This is the enthalpic regime, whose slope ($F(\delta x)$) gives us information about the interaction energy between DNA base pairs. At

about 62 pN a transition is observed[11]: very small additional force is needed to expand the DNA molecule to 1.7 its contour length.[20] The plateau appears close to the length of fully extended B-form DNA and represents a tension-induced structural transition. This is a process of reversible transformation of bases from the helical B-form DNA (B-DNA) to a stretched ladder structure (S-DNA).[11] The transition from B-DNA into S-DNA (B-S transition) is very sharp, indicating a high level of cooperativity of the B-S transition.[27]

Before the transition, the flexibility of a DNA molecule may be characterized by its persistence length, L_p.[14] The probability that two segments separated by a distance L along the molecule are aligned is given by $\exp(-L/L_\mathrm{p})$.[31] The stiffer the chain, the longer the persistence length. For dsDNA in physiological salt conditions, the persistence length is approximately 50 nm.[19]

Worm-like chain (WLC) model

Worm-like chain model assumes that polymer behaves as a long 1-dimensional flexible rod, whose contour length is much longer than the persistence length, so that the polymer can bend due to thermal fluctuations.

The graph was removed because of copyright restrictions.

Figure 1.12: Definition of contour length, L_c, persistence length, L_p, position vector $\vec{r}$ and s the length.[53]

Let us call $\rho^{-1} = \frac{\partial^2 r}{\partial s^2}$ the inverse radius of curvature. Then the bending energy per unit length is $\frac{1}{2}\kappa\left(\rho^{-1}\right)^2$. L_p is the characteristic bending length under thermal fluctuations:

$$\frac{k_{\mathrm{B}}T}{L_{\mathrm{p}}} \sim \frac{1}{2}\kappa\left(\rho^{-1}\right)^2 \sim \frac{1}{2}\kappa\frac{1}{L_{\mathrm{p}}{}^2} \tag{1.1}$$

so that:

$$L_{\mathrm{p}} \sim \frac{1}{2}\frac{\kappa}{k_{\mathrm{B}}T} \tag{1.2}$$

In the case of simple springs one can write the Hooke's law to calculate the force, F, arising from the displacement, z, of the spring's end from its equilibrium position:

$$F = -kz \tag{1.3}$$

where k is the spring constant. The negative sign is because the restoring force always acts in the opposite direction of the displacement. At the lowest forces the DNA molecule behaves as an entropic Hookean spring and for forces smaller than $k_{\mathrm{B}}/L_{\mathrm{p}}$ it gives:

$$F = \frac{3k_{\mathrm{B}}T}{2L_{\mathrm{p}}}\left(\frac{z}{L_{\mathrm{c}}}\right) \tag{1.4}$$

For dsDNA the Hooke's constant is $k_{DNA} = 3k_{\mathrm{B}}T/2L_{\mathrm{p}}L_{\mathrm{c}}$. For example for a 10 μm dsDNA molecule this constant is approximately 10^{-5} pN nm^{-1}.

For a wider force range, Marko and Siggia [9] proposed the following formula to approximate the force-extension relation given by the WLC model:

$$F = \frac{k_{\mathrm{B}}T}{L_{\mathrm{p}}}\left[\frac{1}{4\left(1 - \frac{z}{L_{\mathrm{c}}}\right)^2} - \frac{1}{4} + \frac{z}{L_{\mathrm{c}}}\right] \tag{1.5}$$

where F is the force, z is an end-to-end distance extension, L_{c} is the contour length of

the chain, L_p is the persistence length of the chain, k_B is the Boltzmann constant and T is the temperature.

This approximate formula describes well the behavior at low forces, where DNA acts as a Hookean spring. Then it differs from the exact solution of the WLC model by as much as 10% for $z/L_c \sim 0.5$. It overestimates the increase of force needed to increase the length of DNA when its length is close to L_c. This may lead to overestimation of the value of L_p of the order of 5%. Bouchiat et al. [16] subtracted the Marko-Siggia interpolation formula from the exact numerical solution of the WLC model and expressed the residuals as a seventh-order polynomial, which led to an accuracy better than 0.01% over the useful extension range. The formula is as follows:

$$F = \frac{k_B T}{L_p} \left[\frac{1}{4 \left(1 - \frac{z}{L_c} \right)^2} - \frac{1}{4} + \frac{z}{L_c} + \sum_{i=2}^{i \leq 7} \alpha_i \left(\frac{z}{L_c} \right)^i \right] \tag{1.6}$$

with $\alpha_2 = -0.5164228$, $\alpha_3 = -2.737418$, $\alpha_4 = 16.07497$, $\alpha_5 = -38.87607$, $\alpha_6 = 39.49944$ and $\alpha_7 = -14.17718$.

1.2.2 Modification of the mechanical behavior when DNA is complexed

The influence of the small ligands on DNA may be observed as a change in mechanical properties of the DNA. It is then possible to determine the binding mechanism.

Mechanical properties of DNA are characterized by:

* ⋆ its flexibility (in the entropic region), characterized by the persistence length,

* ⋆ its elasticity (in the enthalpic region), characterized by its Young modulus,

* ⋆ the possibility to transform the double helix into the ladder.

When complexation occurs, it induces a change of the DNA structure. This leads to modification of the flexibility, of the strength of interaction forces between base-pairs and thus a change of elasticity. Consequently, the B-S transition will also be

The graph was removed because of copyright restrictions.

Figure 1.13: Force-extension data (red crosses) for λ phage dsDNA (48,502 bp) pulled by magnetic beads in 10 mM Na$^+$ buffer. The data are fit to a WLC model solved numerically (WLC exact) or using Equation 3 (WLC interpolated), both assuming $L_\mathrm{p} = 53$ nm. [19]

affected. The mechanical properties are sensitive to changes of structure. Depending on the interaction, different structural alterations occur. They can be revealed by force-extension measurements. Below I concisely describe those interactions.

Different types of interaction

There are several ways of interaction: [38]

★ Cross-linking

Cross-linkers are small molecules that bind DNA irreversibly, forming inter-strand (opposite strands) or intra-strand (the same strand) cross-links between specific dsDNA bases. One of the examples is cisplatin, used in cancer chemotherapy, which binds dsDNA. It decreases the cooperativity of the melting transition and demonstrates slow binding kinetics. The lack of hysteresis in the presence of cisplatin suggests that the two single strands are very close to each other after cross-linking, which allows them to re-anneal on the timescale of the stretching

experiment. [18] Figure 1.14 shows the change of mechanical properties of dsDNA as a function of the time of the reaction of cisplatin on the DNA. After 1 hour the hysteresis between stretching and relaxation almost disappears. After 24 hours the overstretching plateau rose up to 73 pN, which means a large reduction in the cooperativity of the transition.

The graph was removed because of copyright restrictions.

Figure 1.14: A single molecule of DNA is stretched between an AFM-tip and a substrate immediately after adding an excess of cisplatin (a). The progress of the chemical reaction is then followed on the same molecule: after 1 h (b) the molecule is shortened and the hysteresis between stretching and relaxation has vanished. After 24 h of reaction (c) the molecule is saturated with cisplatin, resulting in a less cooperative overstretching transition that ends at 73 pN and further shortening of the molecule is seen. The inset shows the superposition of 30 curves obtained on different molecules. [23]

⋆ Intercalation

Ethidium bromide is a well-studied dye, which intercalates into DNA without sequence specificity. [23] Figure 1.15 shows the force-extension curve dependence on different concentrations of ethidium bromide. The increased slope of the transition regime indicates the reduction in cooperativity as compared to the curve for DNA in pure buffer.

The DNA is extended when the intercalation takes place. It is caused by the insertion of the intercalator between two adjacent base pairs. [4] The length extension

for B-DNA is approximately 3.4 Å per intercalator, so it approximately doubles the two base-pairs distance.

For high concentrations of ethidium bromide increase in contour length and decrease in persistence length is observed, both at low and high forces.

The graph was removed because of copyright restrictions.

Figure 1.15: Force-extension curve of a single molecule of DNA in pure buffer (a) and in the presence of 0.44 μg ml^{-1} (b) and 2.2 μg ml^{-1} (c) ethidium bromide, referring to approximately 1 molecule of ethidium bromide per 10 and 2 bp, respectively. With increasing concentration of ethidium bromide the overstretching plateau shortens while the force at the end of the transition increases to 110 pN. At high concentrations the hysteresis between stretching and relaxation is drastically reduced. [23]

⋆ Groove binding

Most of the molecules binding to dsDNA grooves are positively charged. Binding is mostly due to electrostatic interaction and is assisted by hydrogen bonds and van der Waals interactions. [23] Berenil, well-known minor groove binder, increases the melting force and preserves melting transition cooperativity.

Figure 1.16 shows effect of berenil on DNA. At low concentration berenil changes the force-extension curve only in the low force regime, which is typical for minor groove binders, which barely change B-DNA structure. Shape of the last curve is much different, but this is related to intercalation of berenil, which occurs at high concentration.

The graph was removed because of copyright restrictions.

Figure 1.16: A single molecule of DNA is stretched in pure buffer (a). After berenil is added in a concentration of 1.5 µg ml^{-1} (approximately 1 molecule per 4 bp) the force curve only deviates from the previous curves in the low force regime, indicating a minor deviation from the native conformation (b). Increasing the concentration of drug to 15 µg ml^{-1} (approximately 1 molecule of berenil per 0.4 bp) results in a drastic change in the force curve: hysteresis is reduced and the force at the end of the transition is increased to 95 pN (c). [23]

Melting of double-stranded DNA

The presence of HIV-1 NC lowers the free energy of DNA melting, ΔG. It falls from $\sim 2k_\mathrm{B}T$ to $\sim 1k_\mathrm{B}T$ for 10 nM HIV-1 NC, destabilizing the DNA duplex. NC facilitates the rearrangement of the structure of nucleic acids, by the significant lowering of the cooperativity and stability of DNA helix-coil transition, in order to form the lowest energy state. Destabilization of dsDNA is due to NC's preferential binding to ssDNA.[22] The helix-coil transition free energy (ΔG) is significantly reduced in the presence of HIV-1 NC. This decrease of melting force energy manifests itself at high NC concentration by a separation of the strands.

The stability of the helix with respect to the coil form of DNA is determined by ΔG change from helix to coil state. It is taken from the area between the stretching curves for single- and double-stranded DNA.[24] This decrease of melting force energy may be measured by comparing ssDNA and dsDNA's force-extension curves.

The graph was removed because of copyright restrictions.

Figure 1.17: NC binding decreases the effective length of ssDNA. The data shown (black squares) are for l-DNA relaxed in 10 mM Hepes, pH 7.5, 25 mM [Na$^+$], following a stretch of dsDNA to 80 pN in the presence of 7 nM NC. The solid line is a fit to the data in which ssDNA was stretched in 150 mM NaCl. b is the extension of the DNA molecule per base pair. (Inset) The stretch (empty square) and relaxation (black triangle) curve for dsDNA in 25 mM ionic strength without NC. [22]

In the absence of a DNA binding protein, forces greater than 140 pN are required in order to completely separate two DNA strands by stretching. [17] When dsDNA is stretched to 80 pN in the presence of NC at 25 mM ionic strength, the relaxation curve is similar to that of ssDNA (see Figure 1.17). This suggests that under low salt conditions in the presence of NC complete separation of the two DNA strands takes place.

In comparison with normal ssDNA molecule, higher force is needed to extend the NC-bound ssDNA. That means that NC binding reduces the ssDNA contour length and significantly changes its stretching behavior.

Moreover, for kinetic properties, the small hysteresis observed during the stretching suggests that NCp7 can quickly release the ssDNA to allow rapid re-annealing of the two complementary strands. [33]

Complexation of DNA with proteins: Thermodynamic aspects

The dsDNA force-extension curve is very sensitive to the presence of NC protein. Cruceanu et al. [32] follow the variation of the force-extension curve as a function of the protein

The graph was removed because of copyright restrictions.

Figure 1.18: Force-extension curve of dsDNA (solid line) and the FJC model for ssDNA stretching (dotted line) in the absence (a) and the presence (b) of 7 nM HIV-1 NC. [38]

concentration c to estimate the equilibrium binding constant of the protein to DNA.

After the addition of the NC, the most noticeable change in DNA stretching and relaxation behavior is the significant increase in the slope of the force-induced melting transition (see Figure 1.19).

The graph was removed because of copyright restrictions.

Figure 1.19: Stretching (solid lines) and relaxing (dashed lines) curves for λ-DNA in the presence of the NCp7. Protein concentrations are indicated in the figure. The stretching and relaxing curves in the absence of protein are also shown (black solid line and filled diamonds, respectively). [32]

The force transition width ΔF is the difference in forces over which the DNA molecule switches from ds-state do ss-state. This difference is arbitrarily measured between the points at which the tangent line intersects tangent lines to the dsDNA and ssDNA extension curves (see Figure 1.20).

The graph was removed because of copyright restrictions.

Figure 1.20: Stretching curves for λ-DNA in the absence of protein (open circle), in the presence of NCp7 protein (closed circle) and for ssDNA with NC bound on it (closed triangle). Stretching curves for dsDNA (open square) and ssDNA (open triangle), fit to standard polymer models, in the absence of protein are also shown. The method used to determine ΔF, the force transition width, is shown schematically. [32]

The values of the transition width obtained are then plotted as a function of protein concentration c, like in Figure 1.21. The slope of the linear region of this plot is used to estimate the binding constant.

The graph was removed because of copyright restrictions.

Figure 1.21: Dependence of the transition width ΔF on the protein concentration. Each data point for the NC protein is given as the mean standard error. The solid lines are linear fits to the data in the low concentration limit. $\delta F = (5.02 \pm 0.97) \cdot c$, where δF is the difference between ΔF in the presence of protein and ΔF in the absence of protein. [32]

It is assumed that:

$$\text{DNA}_{\text{bp}} + \text{NC} \underset{}{\overset{K}{\rightleftharpoons}} \text{NCDNA}_{\text{bp}} \tag{1.7}$$

where DNA_{bp} is an unbound DNA base pair, NC is nucleocapsid, K is the binding constant of protein to DNA and NCDNA_{bp} is a DNA_{bp} bound to a NC. Another assumption is that one NC protein binds to one DNA base-pair.

Under these assumptions, below the saturation of protein concentrations, the fraction of DNA binding sites bound by protein, ϕ, is very small, $\phi \ll 1$ and increases linearly with the concentration of the protein c:

$$K = \frac{[\text{NCDNA}_{\text{bp}}]}{\left([\text{NCDNA}_{\text{bp}}^0] - [\text{NCDNA}_{\text{bp}}]\right)\left([\text{NC}^0] - [\text{NCDNA}_{\text{bp}}]\right)} \simeq \frac{[\text{NCDNA}_{\text{bp}}]}{[\text{NCDNA}_{\text{bp}}^0]\,c} \simeq \frac{\phi}{c} \tag{1.8}$$

where $\left[\text{NCDNA}_{\text{bp}}^0\right]$ and $\left[\text{NC}^0\right]$ are the initial concentrations of DNA and NC, respectively. Consequently:

$$\phi = K \cdot c \tag{1.9}$$

Assuming that the change in the transition width, δF, is proportional to the fraction of sites bound by protein, ϕ, up to the saturated situation, it may be also written as:

$$\delta F(c) = \phi \cdot \delta F_{\text{sat}} \tag{1.10}$$

where $\delta F = \Delta F - \Delta F_0$ and ΔF_0 is the transition width in the absence of protein and δF_{sat} is the transition width at saturation.

Combining equations 1.9 and 1.10 it is possible to estimate the protein-DNA equilibrium binding constant:

$$K = \frac{1}{\delta F_{\text{sat}}} \cdot \frac{\delta F(c)}{c} = \frac{1}{\delta F_{\text{sat}}} \cdot \frac{\mathrm{d}\,\delta F(c)}{\mathrm{d}\,c}\bigg|_{c \to 0} \qquad (1.11)$$

$$K = \frac{1}{\delta F_{\text{sat}}} \cdot \frac{\delta F(c)}{c} = \frac{1}{\delta F_{\text{sat}}} \cdot \frac{\mathrm{d}\,\delta F(c)}{\mathrm{d}\,c}\bigg|_{c \to 0} \qquad (1.12)$$

Thus, the adsorption of the protein onto DNA modifies the mechanical properties of double-stranded DNA. As a consequence the change of flexibility and the change of the slope of B-S transition may be used to characterize this equilibrium quantitatively.

Complexation of DNA with proteins: Kinetic study

The affinity is a thermodynamic quantity, related to the difference of free energy of NCp7 in solution and NCp7 complexed with DNA.

Nevertheless, in the case of DNA/protein interaction, the potential landscape of the interaction might be extremely complex. It can involve a mix of intermediate states, leading to slow kinetic interaction.

For instance, in the case of the protein has to adopt the correct configuration in order to bind to DNA.

The kinetics of adsorption may moreover be controlled by interaction between complexed and free proteins. Due to these interactions, proteins may prefer to bind DNA close to an already bound protein: this is a cooperativity phenomenon.

The cooperative binding of proteins to DNA is very important for the regulation of gene expression, because it allows a sensitive response to small changes in protein concentration. Although the structural basis of the cooperativity is not fully understood, it is known that long-range cooperativity is possible through loops, formed by the association of two DNA-binding proteins. Specific protein-protein interactions or a generic cooperativity resulting from structural distortions induced by the binding of a protein to DNA may be related to cooperativity at shorter distances. [15]

As a consequence of cooperativity the number of adsorbed proteins per unit time is a non-monotonous function, that goes through a maximum values when the number of

already adsorbed sites is high enough so that a new protein finds easily an adsorption site close to a bound protein, but low enough, so that the fraction of empty adsorption sites remains important.

Our goal

We will be interested in studying the time evolution of the persistence length of DNA. We are going to characterize the evolution of L_p in time from the force-extension measurements performed on optical trap. We will then present a model to relate L_p and the fraction of DNA binding sites bound by protein, ϕ, in order to deduce the rate of complexation as a function of time. Finally, we will be able to compute kinetic constants of the reaction.

Although the equilibrium properties of the DNA-protein complexation have been studied and measured, the kinetics of adsorption is much less described.

We thus wish to study the kinetics od DNA-NCp7 interaction. We will use force-extension experiments to follow the change of mechanical properties of the formed complex as a function of time. We will characterize these changes by the evolution of the persistence length and of the cooperativity of the B-S transition as a function of time.

We will show that both observables lead to values of the fraction of DNA binding sites bound by protein, ϕ. This evolution is thus interpreted as showing cooperative adsorption. From a quantitative analysis of our results we will deduce the kinetic constant of adsorption of NCp7 onto DNA far/close to an already adsorbed protein.

Chapter 2

Experiment, results, and discussion

2.1 Principle of the measurement

As mentioned before, the later stage of the retroviral life cycle is characterized by the RNA reverse transcribed into proviral cDNA [32]. This process involves several transfer steps of strands which require major rearrangement of the secondary DNA structure. While this restructuring results in a lower free energy of the nucleic acid molecules and is therefore spontaneous, it occurs to be extremely slow. [32] NCp7 has been shown to significantly accelerate these reactions. [32] Hence it seems to be important to examine the kinetics of adsorption of NCp7 to DNA.

In order to understand the effects of the processing of NC on its nucleic acid chaperone and binding activities, we examine the interaction of NCp7 with DNA performing single molecule experiments. Single molecule DNA stretching, also referred to as force-induced melting (FIM), provides valuable information regarding the interaction between nucleic acids and proteins or small molecules that bind to dsDNA. The FIM technique may also reveal insights into the kinetics of protein-DNA interactions. This is accomplished by comparison of the force-extension profiles during DNA stretching and relaxation cycles in the absence and presence of protein. [26, 28, 29, 32]

To learn how NCp7 binds with DNA, we needed to recognize the structure of NCp7-DNA complex. We measured its mechanical properties which relate to the structural details. The mechanical properties of DNA alone and then DNA-NCp7 complex have been studied using the optical tweezers.
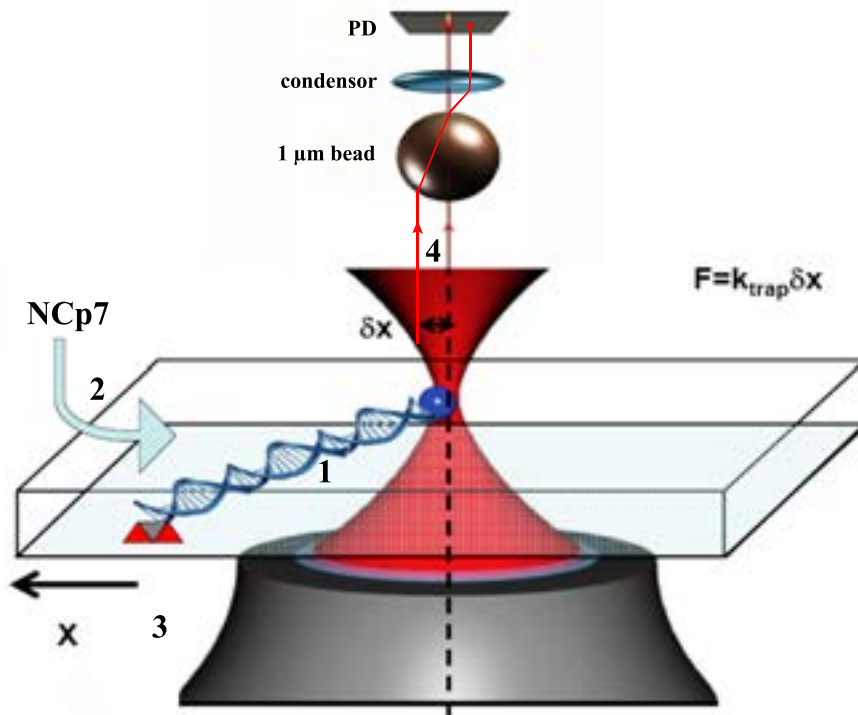
Figure 2.1: Optical trap scheme.

Optical tweezers enable us to apply forces of pN order and to stretch single DNA molecule precisely. They exhibit a strong stability and feedback. In low force regime, double-stranded DNA reveals entropic elastic response. As the force increases enthalpic stretching of the base pairs takes place and results in a much stiffer response. Then a transition between a double helix and a ladder occurs, which takes place at a constant force called melting force. This results in an increase of the length of DNA. The manifestation of this transition between DNA structures is plateau on the force-extension curve, which appear at characteristic force of 62 pN.

With DNA stretching by optical tweezers, we are able to determine dependence of the fraction of binding sites of DNA bound by protein on time. In addition, we can obtain information on the effect of each protein on force-induced DNA melting, i.e. strand separation due to an external pulling force. In turn, this enables us to determine the effect of each protein on DNA duplex stability and on the kinetics of the strand separation and annealing.

We anchored one end of the DNA to the glass surface. On the second one we attached the streptavidin bead and trapped with IR laser beam. Using a piezo-electrical device we translated the cover slip and stretched the double-stranded DNA molecule, attached

between the cover slip and the bead. We measured the displacement of the bead from the center of the trap and deduced the force exerted by the DNA strand. Before adding NCp7 we first checked the force-extension curve of a pure single DNA molecule, then we introduced given concentration of NCp7 and stretched the DNA-NCp7 complex for each concentration over time. We obtained force-extension curves as a function of time for five concentrations of introduced NCp7—3, 30, and 300 nM and 10 and 100 nM.

The stretching curves used for these measurements do not depend on pulling rate (at the low pulling rates used here) and the measurements therefore are indistinguishable, within the reported experimental error, from equilibrium measurements. [28]

I want to receive adsorption rate as a function of time, $\phi(t)$ and I will determine it by looking at DNA force-extension curves and analyzing persistence length as a function of time, $L_{\mathrm{p}}(t)$.

2.2   Presentation of the data

2.2.1   Results for 3, 30, and 300 nM of NCp7

Force-extension curves—$F(x)$

Figure 2.2 shows the typical force-extension curves as a function of time. At low forces, the entropic regime is observed, in which the elasticity of the molecule is a consequence of the reduction of the number of accessible states under stretching. In this regime, the force-extension law is linear, and the apparent Hooke's coefficient is equal to $3k_{\mathrm{B}}T/2L_{\mathrm{c}}L_{\mathrm{p}}$, where $k_{\mathrm{B}}T$ is the thermal energy, L_{c} the total contour length, and L_{p} the persistence length. Then, after a transition regime, the enthalpic regime is reached in which the force rapidly increases with the extension. In order to minimize the damages induced to DNA by stretching, we have not pulled the molecule up to the B-S transition. The buffer used was 25 mM Tris HCl (pH = 7.5) + 30 mM NaCl + 0.2 mM $MgCl_2$. Experiments are performed at a pulling rate equal to $500\,\mathrm{nm\cdot s^{-1}}$, under which the extension and relaxation curves superimpose over the studied extension range. The maximum extension of the DNA molecule does not evolve with time and is equal to ≈ 0.34 nm per base pair. Nevertheless, an evolution of the curvature of the force-extension curve at the end of the entropic regime is observed. As the total length of the molecule remains constant, this is a consequence of a change of the persistence length of DNA.
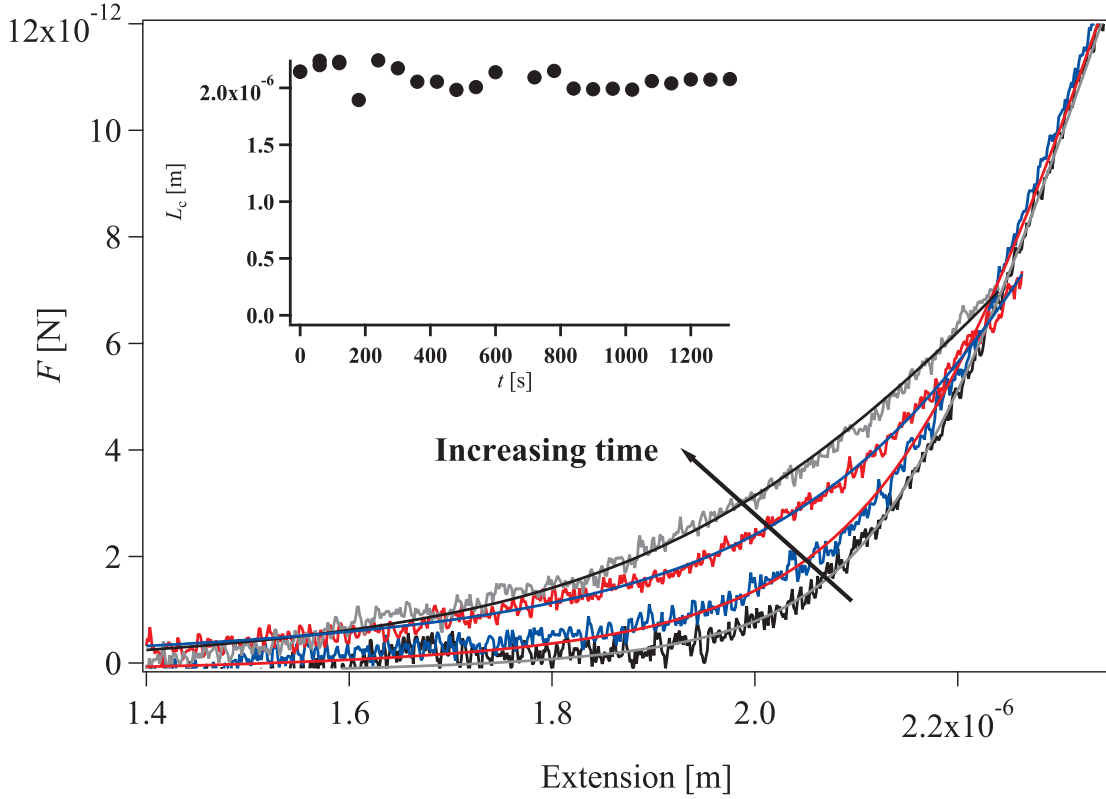
Figure 2.2: Force exerted onto the DNA/NCp7 complex as a function of extension and time. Dashed lines are fits using Equation 1.5. *Inset*: evolution of the contour length with time.

Persistence length in time—$L_p(t)$

Persistence length values, L_p, are obtained from WLC fits (see Section 1.2.1) of the force-extension curves. The data presented in Figure 2.3 represents L_p as a function of time for three concentrations of NCp7—3, 30, and 300 nM. Curves shown are the exponential fits of the data—they are added solely to guide the reader. The plot reveals a slow decrease of the persistence length of DNA after the addition of NCp7.

Model $L_p \rightarrow \phi$

This section will provide the relation between adsorption rate, ϕ and persistence length, L_p. A model is proposed in which the adsorption has two consequences:

- total decorrelation of the orientation of the chain at the adsorption site,
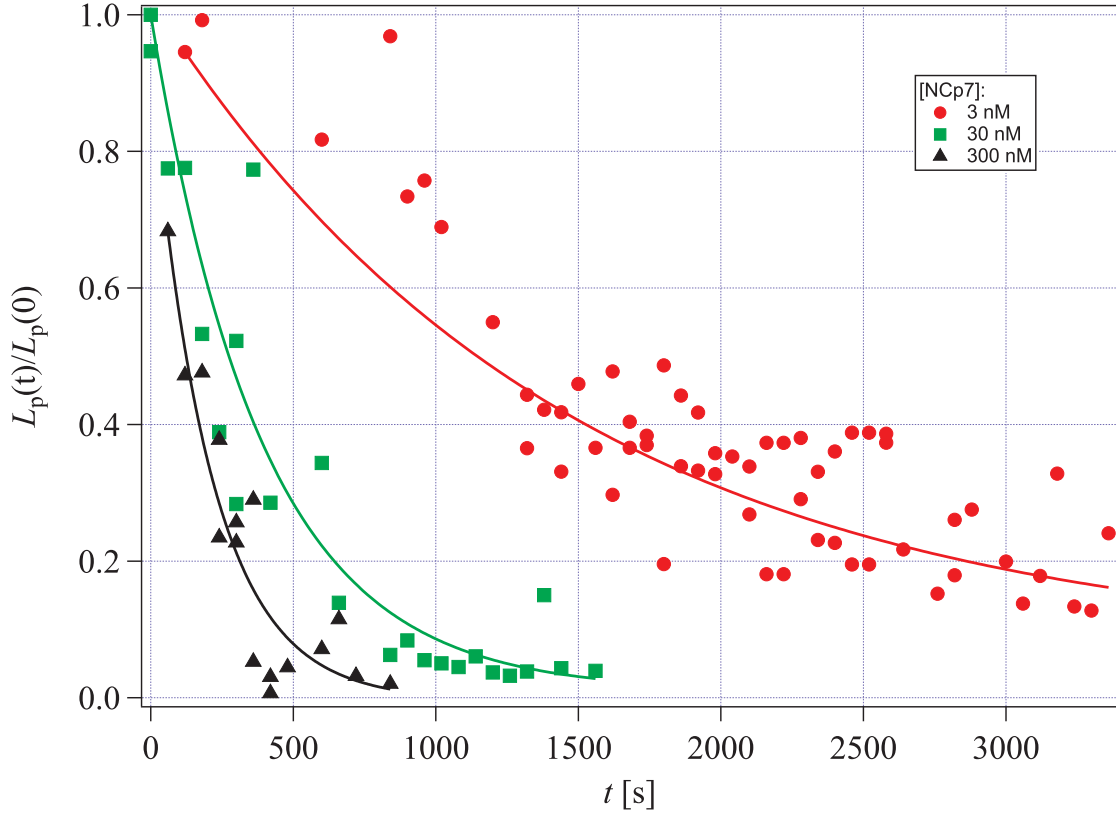
Figure 2.3: Normalized $L_p(t)$ for 3, 30, and 300 nM of NCp7. The values are normalized by the persistence length of bare DNA, equal to 49 nm, according to [13].

- increase of the contour length of the chain.

Figure 2.4 depicts described model, showing what happens when the protein is adsorbed. After the adsorption the chain orientation is totally decorrelated at the adsorption site. Moreover L_c increases by Δb for each adsorption event.

Behavior of DNA chain upon adsorption is described by the following equations. The initial, temporary and final values of L_c and L_p are presented. We denote:

- L_{c_0}, L_c, L_{c_∞}: contour lengths at $t = 0$, t and $t \to \infty$, respectively,

- L_{p_0}, L_p, L_{p_∞}: persistence lengths at $t = 0$, t and $t \to \infty$, respectively,

- N: number of junctions between rigid rods in the initial chain, so that persistence length is L_{p_0},
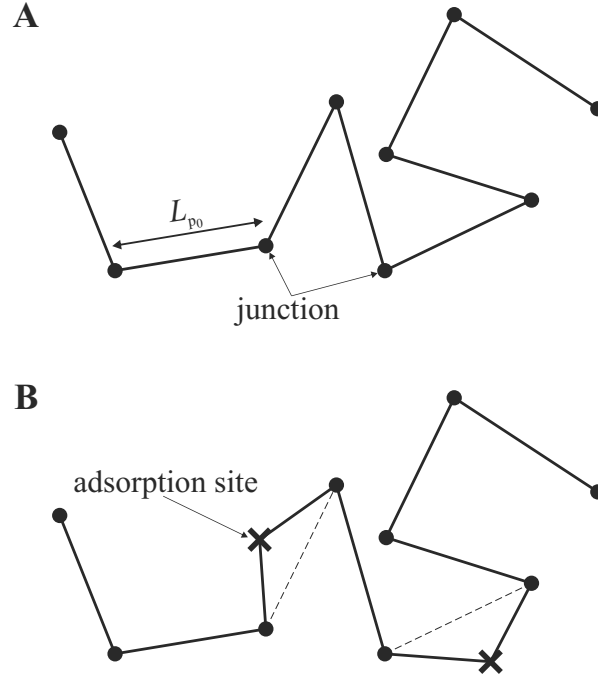
Figure 2.4: The model of adsorption onto a DNA chain. The junctions between rigid rods are symbolized as black circles, the adsorption sites are marked with black crosses. **A.** The DNA chain before adsorption. Average L_p value is equal to L_{p_0}. **B.** Situation after adsorption of a protein.

- n_max: maximal number of adsorption sites,

- ϕ: fraction of adsorption sites adsorbed at the time t (if n sites have been adsorbed, then $\phi = n/n_\mathrm{max}$),

- Δb: the increase of contour length of the chain per adsorption event.

Firstly, let us describe the persistence length. We have on one side:

$$L_{\mathrm{c}_0} = (N + 1)L_{\mathrm{p}_0} \tag{2.1}$$

$$L_\mathrm{c} = (N + 1 + \phi n_\mathrm{max})L_\mathrm{p} \tag{2.2}$$

$$L_{\mathrm{c}_\infty} = (N + 1 + n_\mathrm{max})L_{\mathrm{p}_\infty} \tag{2.3}$$

On the other side we have the increase of contour length:

$$L_c = L_{c_0} + \phi n_{\max} \Delta b \tag{2.4}$$

$$L_{c_\infty} = L_{c_0} + n_{\max} \Delta b \tag{2.5}$$

Consequently:

$$L_c = L_{c_0}(1 - \phi) + \phi L_{c_\infty} \tag{2.6}$$

$$= L_{c_0}[(1 - \phi) + \alpha\phi] \tag{2.7}$$

where $\alpha = L_{c_\infty}/L_{c_0}$.

Having the definitions of L_c and L_p we can introduce the following relationship to calculate ϕ:

$$\phi = \frac{L_{p_0} - L_p}{(1 - \alpha) L_{p_0} - \left(1 - \alpha\frac{L_{p_0}}{L_{p_\infty}}\right) L_p} \tag{2.8}$$

In the case of $\alpha = 1$, meaning there is no change in L_c, we have:

$$\phi = \frac{L_{p_0} - L_p}{L_{p_0} - L_{p_\infty}} \frac{L_{p_\infty}}{L_p} \tag{2.9}$$

Fraction of adsorption sites adsorbed in time—$\phi(t)$

The fraction of occupied adsorption sites, ϕ, may *a priori* vary from 0 to 1. $\phi = 0$ means that none of the adsorption sites is occupied by the protein. $\phi = 1$ is for the saturation level, when all the adsorption sites are occupied. To calculate ϕ as a function of time I used Equation 2.8.

L_{p_0} and L_{p_∞} are estimated from Figure 2.3. For all the concentrations L_{p_0} was set to 120 nm. L_{p_∞} value depends on concentration and for 3 nM concentration was 10 nm, whereas for 30 and 300 nm it was 1 nm. The resulting curves are shown in Figure 2.5.
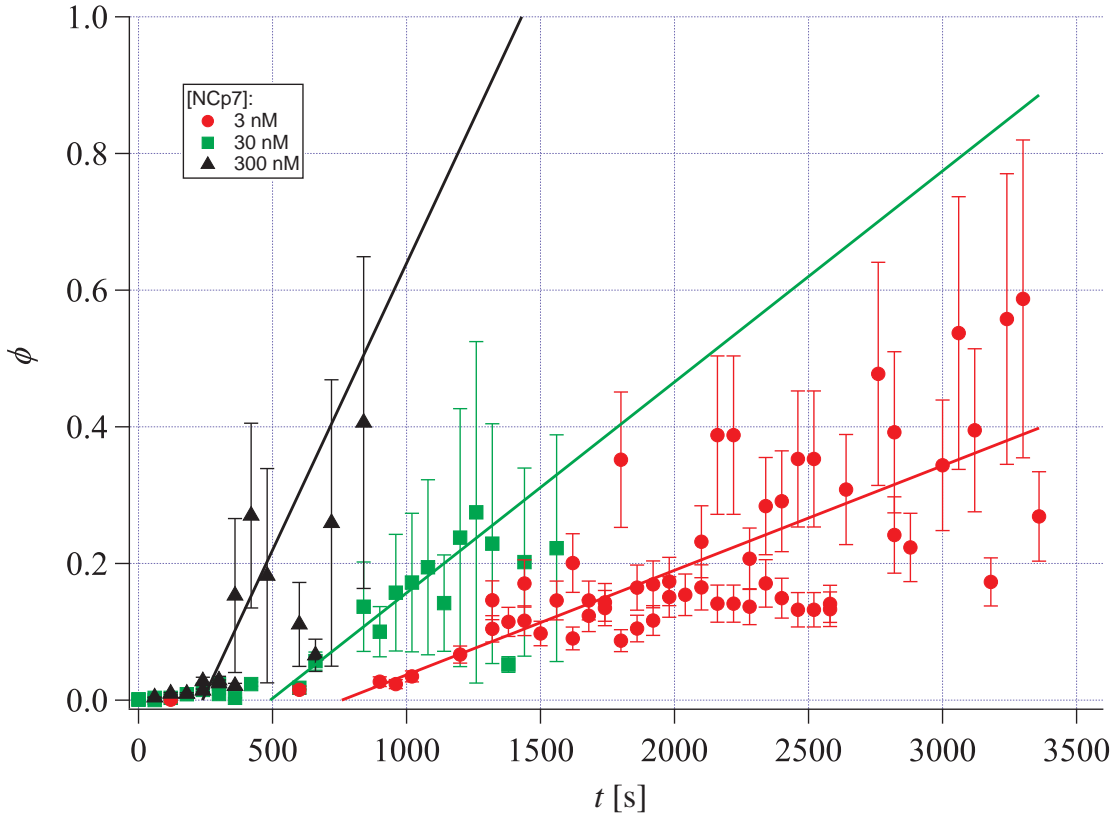
Figure 2.5: The fraction of adsorption sites adsorbed in time $\phi(t)$ for 3, 30, and 300 nM of NCp7.

Analyzing the data we can distinguish two regions. The first one when ϕ values remain small enough, meaning that very small number of proteins has been adsorbed to the chain. Later the second region appears, when ϕ starts to grow linearly. The regions of ϕ growth for each concentration of NCp7 were fitted with linear fit just to make it easier for a reader to follow the slope of the reaction.

Figure 2.6 illustrates the Equation 2.8. The coefficients were chosen as follows: $L_{p_0} = 120$nm, $L_{p_\infty} = 1$ nm, $\alpha = 1$. L_p is plotted in whole range between L_{p_0} and L_{p_∞}.

There are two main causes of the uncertainty of ϕ computation. The first problem is connected with fitting the force-extension data to retrieve L_p. When adsorption ratio increases, the slope of the force-extension curve in the pulling of the chain (enthalpic) regime decreases. As described in the Section 1.2.1 on page 18 this slope is not described by the WLC theory and the WLC fit is less accurate.
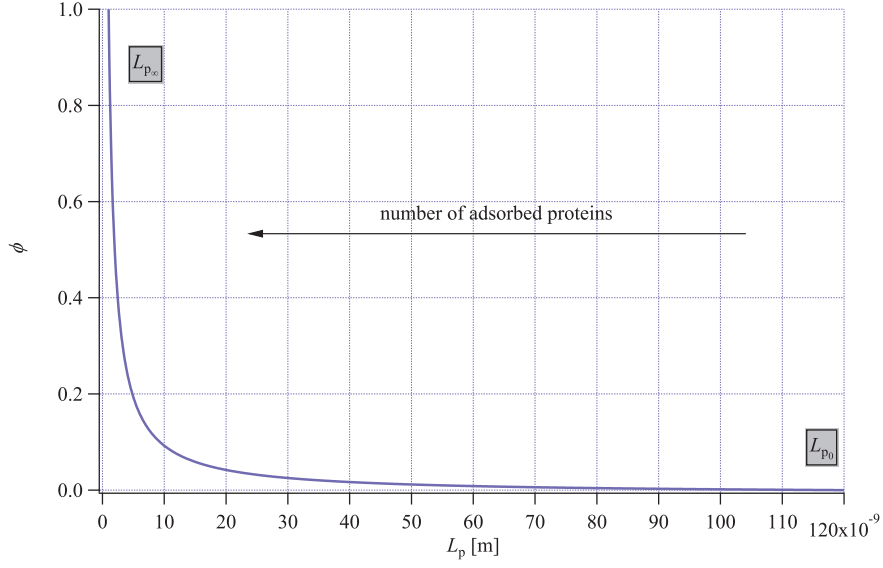
Figure 2.6: Theoretical curve of $\phi(L_\mathrm{p})$ for $L_{\mathrm{p}_0} = 120$ nm and $L_{\mathrm{p}_\infty} = 1\ nm$.

On the other hand it is easily seen that $\frac{\mathrm{d}\phi}{\mathrm{d}L_\mathrm{p}}$ grows rapidly when L_p approaches L_{p_∞} (as deduced from Equation 2.9). For that reason when the time elapses, smaller values of L_p induce bigger error on ϕ. This error can be computed quantitatively. Let us assume that ΔL_p is given by the difference between the L_p at a given time and its time-average value over a time range of 200 s.

The error bars in Figure 2.5 were calculated taking into account the standard deviation of error between the experimental points and L_p fit given in Figure 2.3. The standard deviation values were as follows: $\sigma_{3\ \mathrm{nM}} = 5.5 \cdot 10^{-9}$, $\sigma_{30\ \mathrm{nM}} = 6.3 \cdot 10^{-9}$ and $\sigma_{300\ \mathrm{nM}} = 4.3 \cdot 10^{-9}$. The formula used to calculate error bars was the following:

$$\Delta\phi = \left|\frac{\partial\phi}{\partial L_\mathrm{p}}\right|\Delta L_\mathrm{p} \tag{2.10}$$

where ΔL_p is the standard deviation of L_p and:

$$\frac{\partial\phi}{\partial L_\mathrm{p}} = \left|-\frac{1}{L_{\mathrm{p}_0} - L_{\mathrm{p}_\infty}}\frac{L_{\mathrm{p}_\infty}}{L_\mathrm{p}} - \frac{L_{\mathrm{p}_0} - L_\mathrm{p}}{L_{\mathrm{p}_0} - L_{\mathrm{p}_\infty}}\frac{L_{\mathrm{p}_\infty}}{L_\mathrm{p}^2}\right| \tag{2.11}$$

$$= \left|-\frac{L_{\mathrm{p}_0}L_{\mathrm{p}_\infty}}{(L_{\mathrm{p}_0} - L_{\mathrm{p}_\infty})L_\mathrm{p}^2}\right| \tag{2.12}$$

2.2.2   Results for 10 and 100 nM of NCp7

An equilibrium DNA stretching curve, $F(x)$, is extremely sensitive to the presence of DNA binding protein. Thanks to that it can be used to observe the binding. The most visible change in the curve's appearance is the increase in the slope of the force-induced melting transition upon addition of the protein. The reasons of this increase in transition width are reduction in DNA melting cooperativity and intercalation of NC into dsDNA. [32]

Force-extension curves—$F(x)$

Stretching of the DNA was performed in a room temperature in 20 mM HEPES (pH=7.5).

We used a pure single dsDNA molecule curve, received before protein addition, as a reference. We obtained the evolution of DNA-NCp7 force-extension curves in a time course for 10 nM (Figure 2.7) and 100 nM (Figure 2.8) of NCp7.

The curves corresponding to reactions at low forces applied (below 10 pN) reveal no changes in DNA length. At higher forces ($F > 10$ pN) we observe that the DNA length and force-induced melting transition increase. It may be observed that the slope of B-S transition increases. In the following part we are going to analyze this increase.
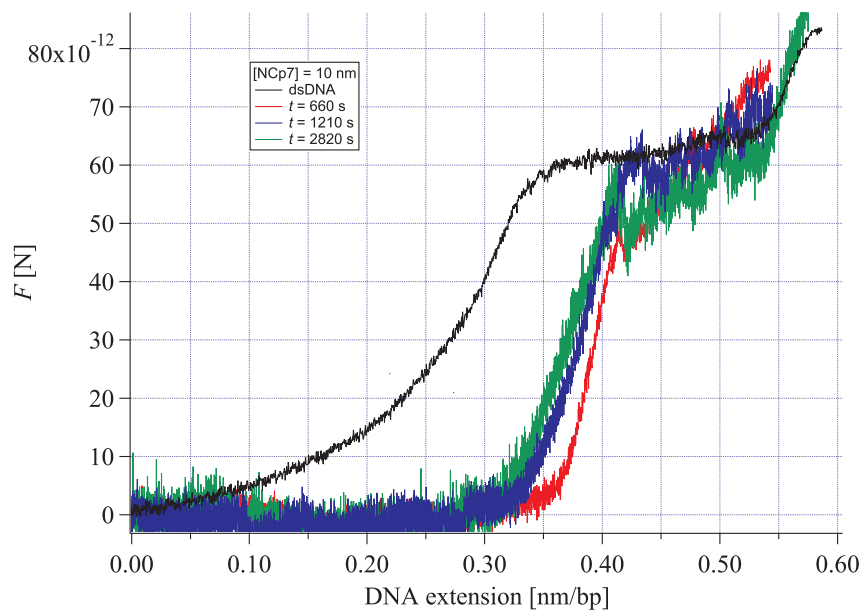

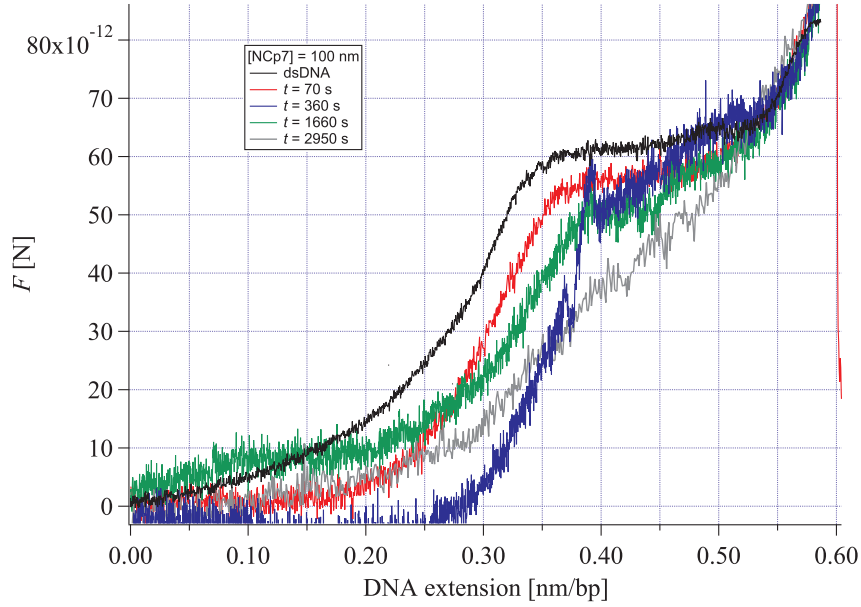**Figure 2.7:** Force-extension curves for 10 nM of NCp7.

Figure 2.8: Force-extension curves for 100 nM of NCp7.

Cooperativity of the B-S transition

The transition from B- to S-state may be described by Zimm/Bragg [1] and Grosberg/Khokhlov [44] theory.

Let us call ΔG_{BS} the difference of energy between the B- and the S-configurations of a base pair.

Then the equilibrium constant for converting a pair from the helical B-state to the stretched S-state, s, is:

$$s = \exp\left[-\frac{2\Delta G_{\mathrm{BS}}}{k_{\mathrm{B}}T}\right] \tag{2.13}$$

We will moreover introduce $2\Delta G_*$ the extra energy of the two B boundaries flanking a S region.

With this notation, we can define a cooperativity parameter:

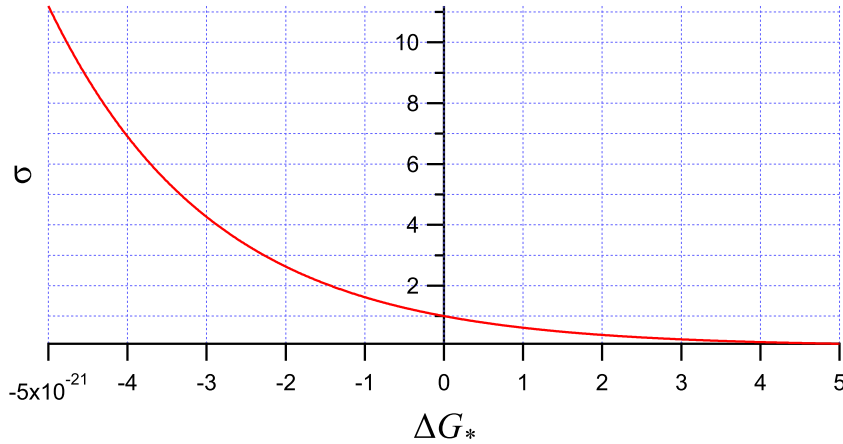$$\sigma = \exp\left[-\frac{2\Delta G_*}{k_{\mathrm{B}}T}\right] \tag{2.14}$$

Figure 2.9: The cooperativity parameter σ as a function of the free enthalpy of B-S boundaries ΔG_*.

$\Delta G_* = 0$ corresponds to $\sigma = 1$, meaning there is no cooperativity, whereas $\Delta G_* = \infty$ corresponds to the limit to high energies of B-S boundaries leading to high cooperativity. Negative values of ΔG_* favor the formation of B-S boundaries and this describe the anti-cooperativity.

With these notations the fraction of the base-pairs in the S-state, $\Theta = \frac{\#\mathrm{bp_S}}{\#\mathrm{bp_S} + \#\mathrm{bp_B}}$, is given by: [44]

$$\Theta(f) = \frac{1}{2} + \frac{s(f) - 1}{2((s(f) - 1)^2 + 4s(f)\sigma)^{1/2}} \tag{2.15}$$

We want to compute the force difference ΔF between the last point of the B-state before transition at the first point in S-state after transition.

Experimentally ΔF is obtained as a function of the elongation:

$$\Delta F = \int_{x_{\mathrm{B}}}^{x_{\mathrm{S}}} \frac{\partial F}{\partial x} \, \mathrm{d}\, x = \int_{\Theta=0}^{\Theta=1} \frac{\partial F}{\partial x} \frac{\partial x}{\partial \Theta} \, \mathrm{d}\, \Theta = \int_{\Theta=0}^{\Theta=1} \frac{\partial F}{\partial \Theta} \, \mathrm{d}\, \Theta \qquad (2.16)$$

and the inversion point of the $F(x)$ curve corresponds to $s = 1$.

We need to compute:

$$\left.\frac{\partial F}{\partial \Theta}\right|_{s=1} = \left.\frac{1}{\frac{\partial \Theta}{\partial F}}\right|_{s=1} \qquad (2.17)$$

$$\left.\frac{\partial \Theta}{\partial F}\right|_{s=1} = \left.\frac{\partial \Theta}{\partial s}\right|_{s=1} \cdot \left.\frac{\partial s}{\partial F}\right|_{s=1} \qquad (2.18)$$

with $s = \exp[-\frac{\Delta G - F\Delta b}{k_{\mathrm{B}}T}]$, where Δb is the difference of length/bp between S- and B-states and F is the applied force and ΔG, the free enthalpy difference between S- and B-states.

$$\frac{\partial s}{\partial F} = s\frac{\Delta b}{k_{\mathrm{B}}T} \iff \left.\frac{\partial s}{\partial F}\right|_{s=1} = \frac{\Delta b}{k_{\mathrm{B}}T} \qquad (2.19)$$

$$\frac{\partial \Theta}{\partial s} = \frac{1}{2}\left(\frac{\sqrt{(s-1)^2 + 4s\sigma}}{(s-1)^2 + 4s\sigma} - (s-1)\left(-\frac{1}{2}\right)\frac{2(s-1) + 4\sigma}{((s-1)^2 + 4s\sigma)^{3/2}} \right) \qquad (2.20)$$

$$\left.\frac{\partial \Theta}{\partial s}\right|_{s=1} = \frac{1}{4\sqrt{\sigma}} \qquad (2.21)$$

which leads to:

$$\Delta F = 4\sqrt{\sigma}\frac{k_{\mathrm{B}}T}{\Delta b} \qquad (2.22)$$

where σ is a cooperativity factor and Δb the difference of length/bp between S- and B-states.

In order to define the transition width ΔF, over which the DNA molecule transforms between the ds- and ss-state, we fit the plateau (transition) midpoint with a tangent line,
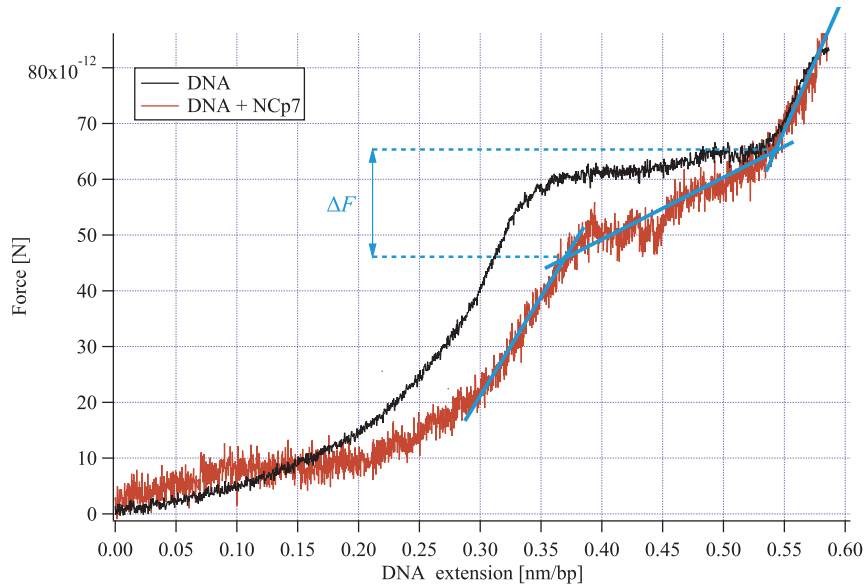
Figure 2.10: The graphical explanation of how to calculate ΔF.

as shown in Figure 2.10. The slope of this line is the change in force from the beginning to the end of the transition. Thus, the force transition ΔF is the difference in forces at which the tangent line intersect tangent lines of the ds- and ss-states of force-extension curve.

We assume after Williams et al. [32] that the transition width, ΔF, is proportional to the fraction of sites bound by protein, ϕ. The conversion from ΔF to ϕ used here is based on Equation 3 in [32]. The article describes analysis of ΔF as a function of protein concentration, whereas I present analysis of ΔF as a function of time. For that reason the equation is modified to represent time function:

$$\delta F(t) = \phi(t) \cdot \delta F_{\text{sat}} \tag{2.23}$$

Consequently:

$$\phi(t) = \frac{\delta F(t)}{\delta F_{\text{sat}}} \tag{2.24}$$

where δF is the difference between ΔF in the presence and in the absence of NCp7 and

δF_{sat} corresponds to the saturation point.

The transition width ΔF as a function of time—$\Delta F(t)$

Figure 2.11 contains transition width as a function of time. As mentioned before ΔF increases with addition of the protein. 100 nM concentration of NCp7 is over saturation level [32], so all the adsorption sites are occupied. The concentration of the protein was increased from 10 to 100 nM after 4500 seconds from the beginning of the experiment. The figure indicates the saturation level, δF_{sat}.
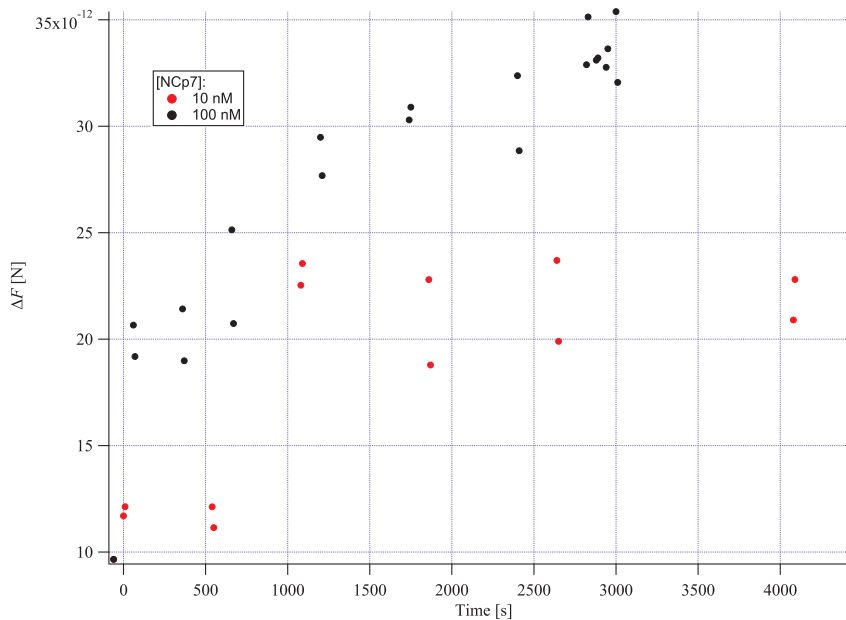

Figure 2.11: The transition width $\Delta F(t)$ for 10 and 100 nM of NCp7.

The fraction of sites bound by protein ϕ as a function of time—$\phi(t)$

The values of ΔF shown in Figure 2.11 are transformed into the fraction of sites bound by protein ϕ values using Equation 2.24 and shown in Figure 2.12.

2.2.3   Discussion

As was mentioned in Section 1.2.2, the cooperativity is a phenomenon, where adsorption of a protein is more probable on a site neighboring with already occupied site, than with
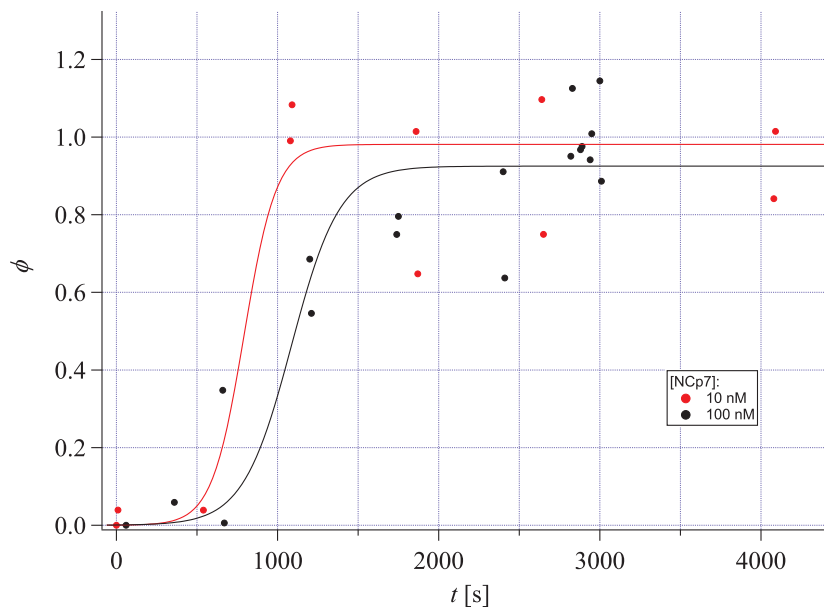
Figure 2.12: The fraction of sites bound by protein ϕ as a function of time for 10 and 100 nM of NCp7. The lines are of sigmoidal shape and are added just as a guide for the eyes.

unoccupied one. Thanks to the cooperativity, much lower concentration of proteins is needed to cause a desired effect.

Below I will present a model describing the adsorption kinetics and will use it to fit the data presented in Figure 2.5.

The cooperativity of the adsorption, a theoretical model

I will now present a model developed by J. B. Keller[2] to describe the adsorption kinetics of a small molecule onto a large macromolecule. Let us consider that the macromolecule consists of a series of sites that can react with a small molecule. In our case this small molecule is NCp7 protein and a site is a short sequence of base-pairs.

In terms of kinetic theory the cooperativity means that the reaction rate of a site without any occupied neighboring site is smaller than the one of a site with one or two occupied neighbors. Figure 2.13 presents schematically a chain under consideration. Unoccupied sites have two neighbors, each of them may be either occupied or unoccupied. Consequently an unoccupied site may have 0, 1, or 2 occupied neighbors.
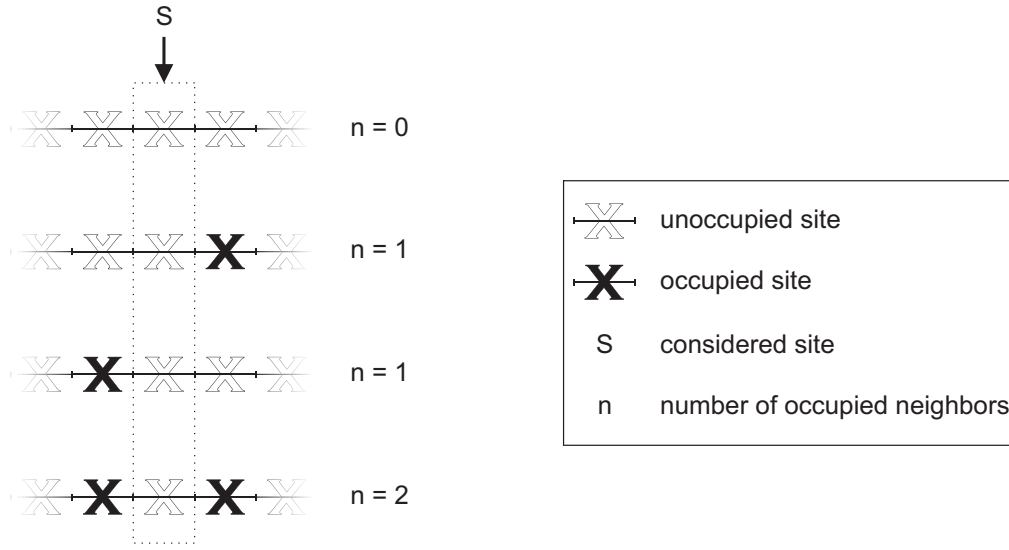
Figure 2.13: Example model of a chain with occupied and unoccupied sites. Unoccupied sites with 0, 1 and 2 neighbors are indicated.

The goal is to determine $\phi(t)$, the fraction of occupied sites at time t, assuming that at $t = 0$ none of them is occupied.

Let us define $N_0(t)$, $2N_1(t)$ and $N_2(t)$, being the fractions of the total number of sites of unoccupied binding sites at time t with 0, 1, or 2 occupied neighbors, respectively. Then $\phi(t)$ is given by:

$$\phi(t) = 1 - N_0(t) - 2N_1(t) - N_2(t) \tag{2.25}$$

In order to determine the $N_i(t)$, we look at the rates at which they change, $\frac{\mathrm{d}\,N_i}{\mathrm{d}\,t}$:

$$\frac{\mathrm{d}\,N_0}{\mathrm{d}\,t} = -k_0 N_0 - 2N_0 \frac{k_0 N_0 + k_1 N_1}{N_0 + N_1} \tag{2.26}$$

$$\frac{\mathrm{d}(2N_1)}{\mathrm{d}\,t} = -k_1 2N_1 + 2(N_0 - N_1)\frac{k_0 N_0 + k_1 N_1}{N_0 + N_1} \tag{2.27}$$

$$\frac{\mathrm{d}\,N_2}{\mathrm{d}\,t} = -k_2 N_2 + 2N_1 \frac{k_0 N_0 + k_1 N_1}{N_0 + N_1} \tag{2.28}$$

where k_0, k_1 and k_2 are the first-order rate constants (i.e. probabilities of reaction per

site per unit time) for binding sites with 0, 1, or 2 occupied neighbors, respectively.

Equations 2.26, 2.27 and 2.28 are explained in Figure 2.14. We consider a site S and describe its probability to evolve from one configuration (left column) to another (right column), by adsorption onto site S or onto one of its neighbors. Rates shown in black represent possibility of appearance of a binding site with specified number of occupied neighbors, whereas rates in red represent possibility of disappearance of such a binding site and have negative sign. $k_i N_i$ is the probability that the considered binding site becomes occupied.

Each term is the product of the number of configurations with the probability that they evolve towards/from a given configuration.

Initially all groups are unoccupied, meaning that:

$$
\begin{aligned}
N_0(0) &= 1 \\
N_1(0) &= 0 \\
N_2(0) &= 0
\end{aligned}
\tag{2.29}
$$

For the further discussion we will use k_0^{-1} as the time unit and define:

$$
\tau = k_0 t
\tag{2.30}
$$

We first realize that Equations 2.26 and 2.27 are coupled equations that do not involve N_2. We thus solve them independently.

Let us divide Equations 2.26 and 2.27 by N_0:

$$
\frac{\mathrm{d}\ln N_0}{\mathrm{d}\,t} = \frac{1}{N_0}\frac{\mathrm{d}\,N_0}{\mathrm{d}\,t} = -k_0 - \frac{2\left(k_0 + k_1\frac{N_1}{N_0}\right)}{1 + \frac{N_1}{N_0}}
\tag{2.31}
$$

$$
\frac{1}{N_0}\frac{\mathrm{d}\,N_1}{\mathrm{d}\,t} = -k_1\frac{N_1}{N_0} + \frac{\left(1 - \frac{N_1}{N_0}\right)\left(k_0 + k_1\frac{N_1}{N_0}\right)}{1 + \frac{N_1}{N_0}}
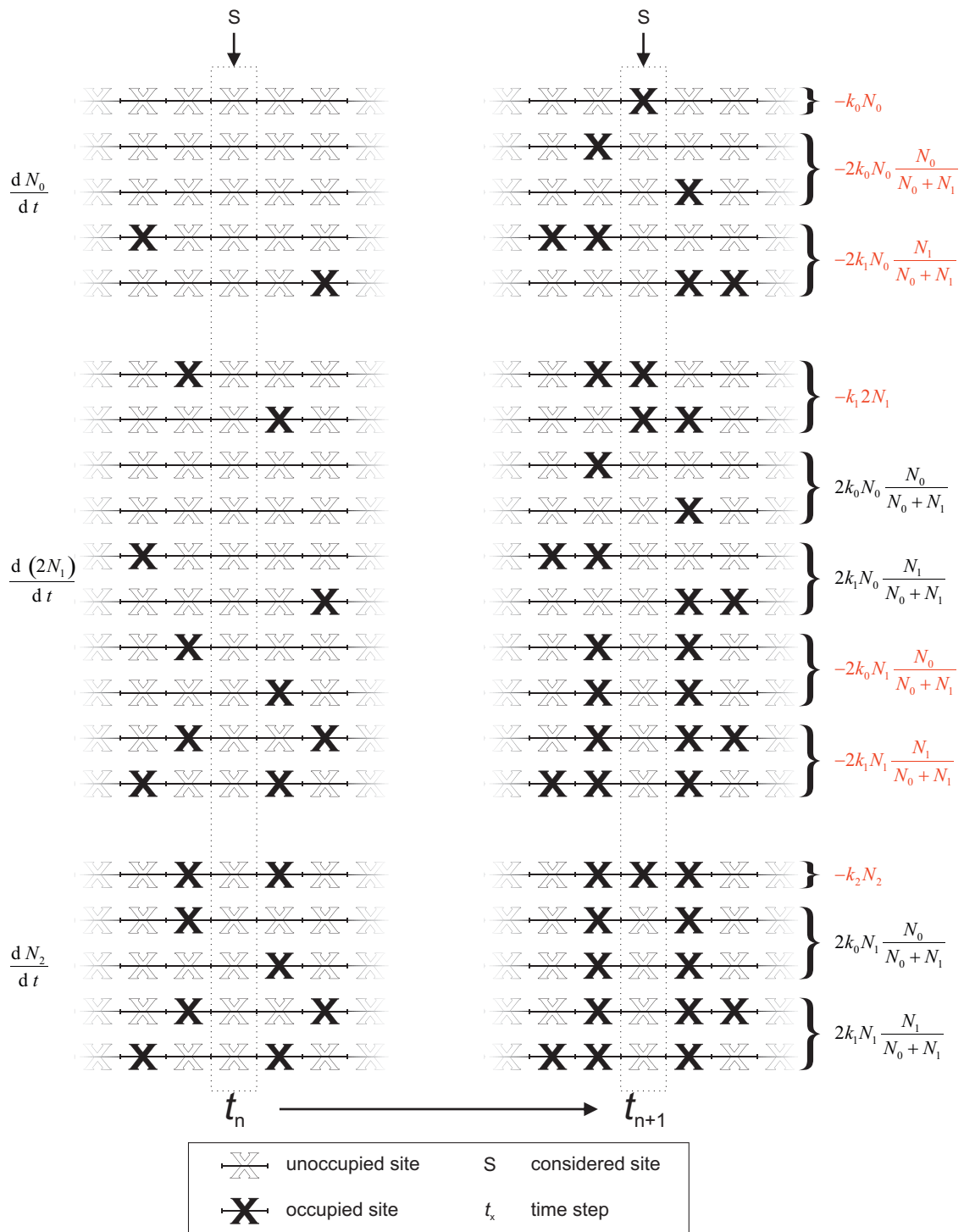\tag{2.32}
$$

Figure 2.14: Scheme of possible adsorption events for adsorption sites with 0, 1, or 2 occupied neighbors. t_n is situation before and t_{n+1} after the protein is adsorbed.

Let us moreover notice that:

$$\frac{\mathrm{d}}{\mathrm{d}\,t}\left(\frac{N_1}{N_0}\right) = \frac{1}{N_0}\frac{\mathrm{d}\,N_1}{\mathrm{d}\,t} - \frac{N_1}{N_0{}^2}\frac{\mathrm{d}\,N_0}{\mathrm{d}\,t} = \frac{1}{N_0}\frac{\mathrm{d}\,N_1}{\mathrm{d}\,t} - \left(\frac{N_1}{N_0}\right)\frac{\mathrm{d}\ln N_0}{\mathrm{d}\,t} \tag{2.33}$$

Then we introduce:

$$x(\tau) = \ln N_0(t) \tag{2.34}$$

$$y(\tau) = \frac{N_1(t)}{N_0(t)} \tag{2.35}$$

And we define the reactivity rates, relating to k_0:

$$
\begin{aligned}
k &= \frac{k_1}{k_0} \\
k' &= \frac{k_2}{k_0}
\end{aligned}
\tag{2.36}
$$

Now Equations 2.31 and 2.32 take the form:

$$\frac{\mathrm{d}\,x}{\mathrm{d}\,\tau} = -\frac{3 + (2k + 1)y}{1 + y} \tag{2.37}$$

$$\left(\frac{\mathrm{d}\,y}{\mathrm{d}\,\tau}\right) + y\left(\frac{\mathrm{d}\,x}{\mathrm{d}\,\tau}\right) = \frac{1 - y - 2ky^2}{1 + y} \tag{2.38}$$

Equation 2.38 gives:

$$\frac{\mathrm{d}\,y}{\mathrm{d}\,\tau} = 1 + y \tag{2.39}$$

$$\mathrm{d}\,\tau = \frac{\mathrm{d}\,y}{1 + y} \tag{2.40}$$

$$\mathrm{d}\,x = -\frac{3 + (2k + 1)y}{1 + y}\frac{\mathrm{d}\,y}{1 + y} \tag{2.41}$$

$$\mathrm{d}\,y = (1 + y)\,\mathrm{d}\,\tau \tag{2.42}$$

We can then integrate to obtain:

$$x = \frac{2(k - 1)y}{1 + y} - (2k + 1)\ln(1 + y) \tag{2.43}$$

$$= 2(k - 1)[1 - \exp(-\tau)] - (2k + 1)\tau \tag{2.44}$$

$$y = \exp(\tau) - 1 \tag{2.45}$$

From Equations 2.34 and 2.35 we finally obtain:

$$N_0(\tau) = \exp(x) = \exp[-(2k + 1)\tau - 2(k - 1)(e^{-1} - 1)] \tag{2.46}$$

$$N_1(\tau) = y\exp(x) = [\exp(\tau) - 1]\exp[-(2k + 1)\tau - 2(k - 1)(e^{-1} - 1)] \tag{2.47}$$

To determine $N_2(t)$, Equation 2.28 is solved, giving:

$$N_2(\tau) = 2\exp(-k'\tau)\int_0^\tau \frac{\exp(k'\tau)N_1(N_0 + kN_1)}{N_0 + N_1}\,\mathrm{d}\,\tau$$

$$= 2\exp(-k'\tau)\int_0^\tau \exp(k'\tau)[1 - 2k + (k - 1)\exp(-\tau) + k\exp(\tau)]N_0(\tau)\,\mathrm{d}\,\tau \tag{2.48}$$

We are interested in situation where $k = k' \geqslant 1$, where $k = k' = 1$ means no cooperativity and $k = k' > 1$ means cooperativity where we do not assume any difference in reactivity rates for 1 and 2 neighboring sites.

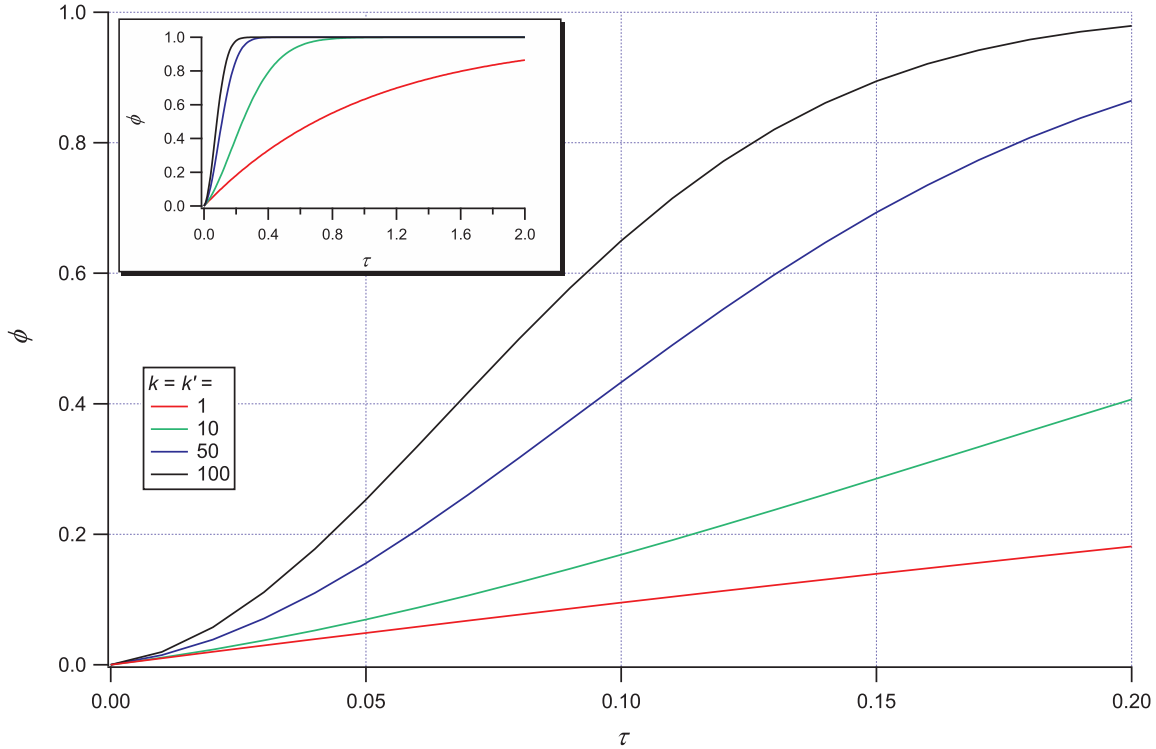Figure 2.15 gives $\phi(\tau)$ for $k = k' = 1, 10, 50, 100$.

Figure 2.15: $\phi(\tau)$ for $k = k' = 1, 10, 50, 100$.

Analysis of the data

Using this relationship, we determine the evolution of the fraction of bound DNA sites from the change of the persistence length (Figure 2.17). A site consists in any sequence of $\approx$ 5–7 base pairs [29]. Remarkably, ϕ does not evolve linearly with time at short times, but the $\phi(t)$ curves exhibit an upward curvature. This has strong consequences as it implies that the rate of adsorption of NCp7 onto DNA depends on time. It increases with time up to a maximum before decreasing again when DNA is close to saturation. We checked that this behavior is not due to the series of stretching applied to the DNA molecule. Indeed, if, after NCp7 injection, a first DNA molecule is stretched during time t, and then a new DNA molecule is selected and stretched, the two DNA molecules exhibit the same persistence length. As a consequence, the measured kinetics is that of an unstretched random coil DNA. We thus assume that the increase of the complexation rate $d\phi/dt$ with time is related to the increase of the number of occupied adsorption sites with time.
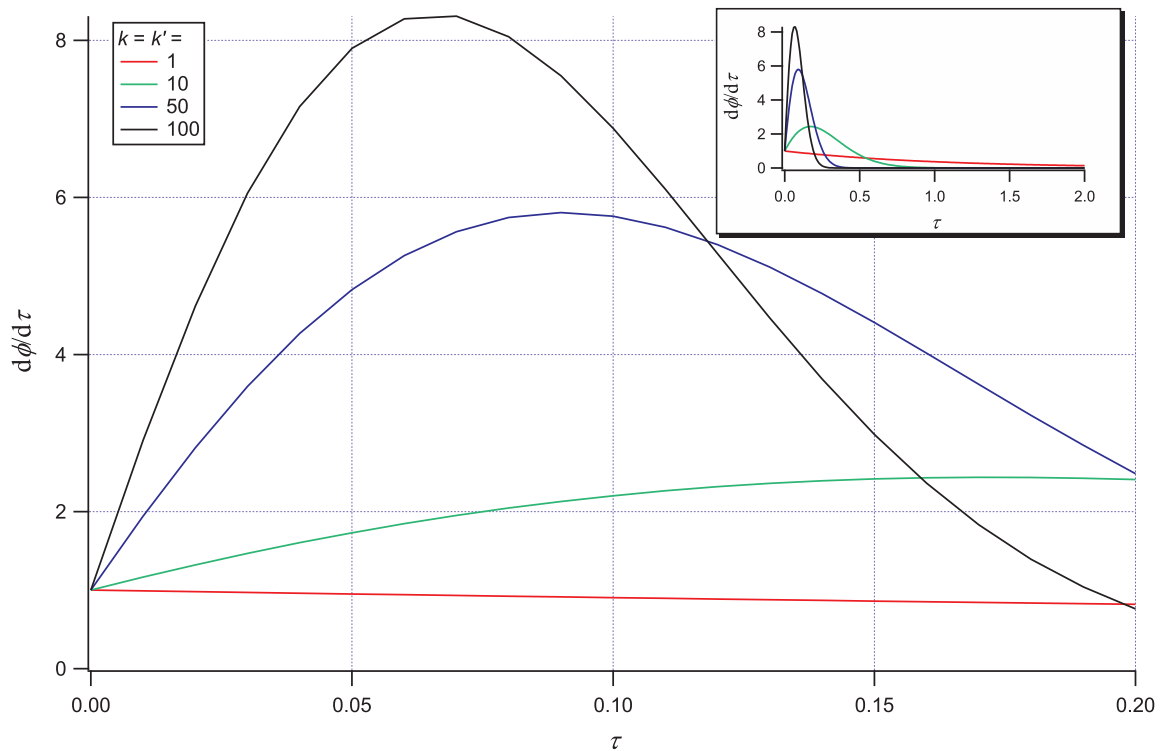
Figure 2.16: $\frac{\mathrm{d}\phi}{\mathrm{d}\tau}(\tau)$ for $k = k' = 1, 10, 50, 100$.

From these equations, the evolution of the fraction of occupied sites, $\phi(t)$ may be studied. Remarkably, the evolution of $\phi(t)$ for the three studied concentrations may all be superimposed onto a unique master curve. Choosing $\phi_{3\mathrm{nM}}(t)$ as the master curve, we define the time scaling coefficients, $\alpha(30\text{ nM})$ and $\alpha(300\text{ nM})$ defined as the coefficients such that, when expressed as a function of αt, the $\phi(t)$ curves superimpose. The obtained values are $\alpha(30\text{ nM}) = 1.79$ and $\alpha(300\text{ nM}) = 3.85$. Then, this unique master curve may be fitted using Equations 2.46–2.48, from which we obtain $k_0(3\text{ nM}) = 70\text{ s}^{-1}$ and $\kappa = 195$. We finally obtain the adsorption rates $k_0(30\text{ nM}) = 125\text{ s}^{-1}$ and $k_0(300\text{ nM}) = 269\text{ s}^{-1}$ (see Figure 2.18).

In conclusion, kinetic study of the aggregation of NCp7(12–55) onto DNA double strands reveal that the interaction is strongly cooperative, even in the absence of the basic residues that flank the zinc fingers structure. In this case, as aggregation induced by the basic residues is avoided, it may be speculated that cooperativity is promoted by correlation of the nucleic acid/NCp7 orientation induced by the zinc fingers.
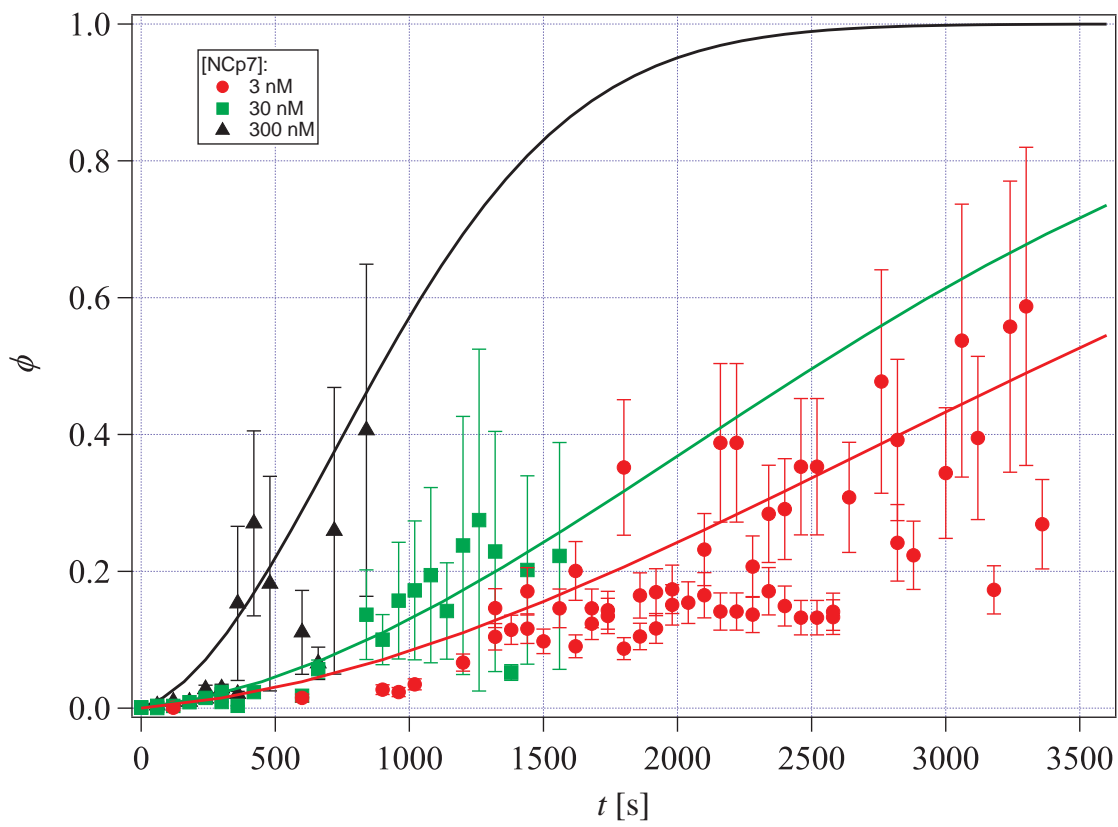
Figure 2.17: $\phi(t)$ for 3, 30, and 300 nM of NCp7. Fit with Keller's model.
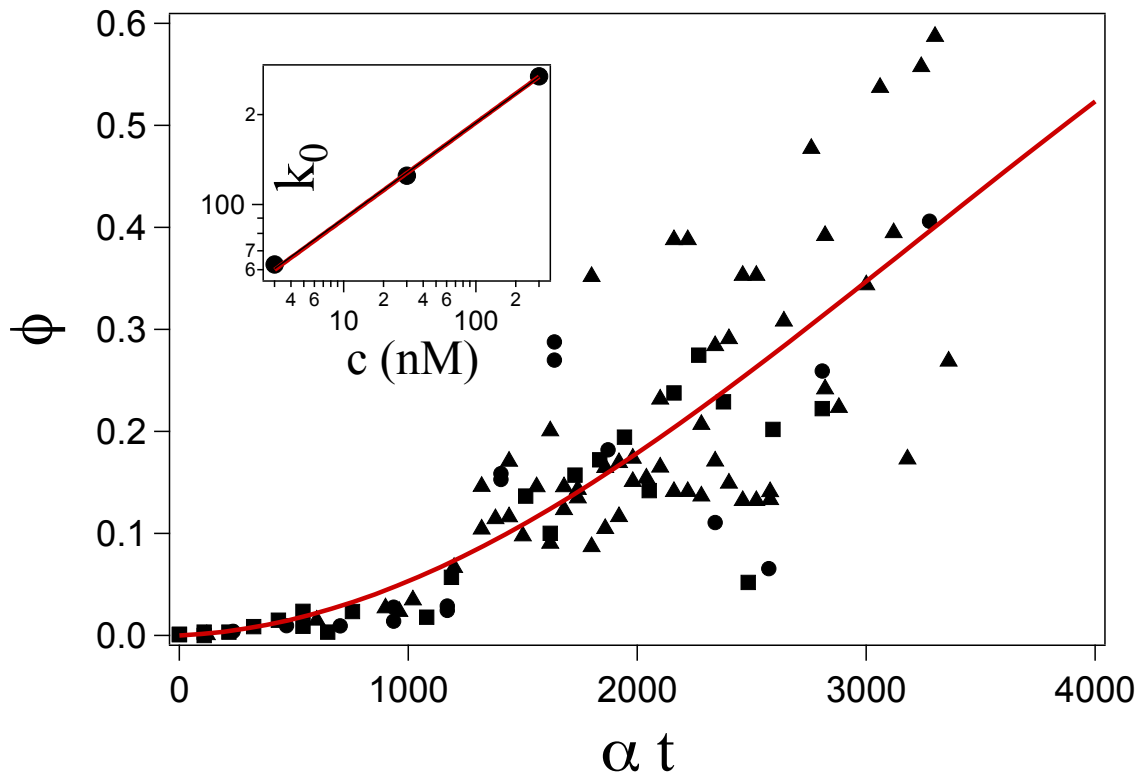
Figure 2.18: Evolution of the ratio of complexed DNA sites, ϕ, as a function of rescaled times, αt, for three NCp7 concentrations: 3 nM ($\blacktriangle$), 30 nM ($\blacksquare$), and 300 nM ($\bullet$). The solid line is a fit using Equation 2.48. *Inset*: adsorption rates k_0 as a function of NCp7 concentration. The line is a power-law fit of the data, whose slope is found to be $0.32 \pm .01$.

Part II

Probe dynamics in a glassy colloidal suspension

Chapter 3

Introduction

3.1 What is Laponite?

3.1.1 Clays in general

Clays and clay minerals are very important industrial minerals. Clays are used for many kinds of ceramics, such as porcelain, bricks, tiles and sanitary ware as well as an essential constituent of plastics, paints, paper, rubber and cosmetics. [79]

They are hydrous aluminium phyllosilicates, that are formed of parallel sheets of silicate, sometimes with variable amounts of iron, magnesium, alkali metals, alkaline earths and other cations. They are ultrafine-grained (less than 2 μm).

Clays are commonly referred to as 1:1 or 2:1. They are fundamentally built of tetrahedral and octahedral sheets (see Figure 3.1). A 1:1 clay consists of one tetrahedral sheet and one octahedral sheet (e.g. kaolinite and serpentine). A 2:1 clay consists of an octahedral sheet sandwiched between two tetrahedral sheets (e.g. illite, smectite, attapulgite, chlorite).

Clays include the following groups:

- ⋆ Kaolin group which includes the minerals kaolinite, dickite, halloysite and nacrite (polymorphs of $Al_2Si_2O_5(OH)_4$)

- ⋆ Smectite group which includes dioctahedral smectites such as montmorillonite and nontronite and trioctahedral smectites for example saponite.

The graph was removed because of copyright restrictions.

Figure 3.1: Schematic presentation of (A) 1:1 layer structures and (B) 2:1 layer structures.

The graph was removed because of copyright restrictions.

Figure 3.2: Diagrammatic sketches of the tetrahedral (left) and octahedral (right) sheets. [80]

- ⋆ Illite group which includes the clay-micas. Illite is the only common mineral.

- ⋆ Chlorite group includes a wide variety of similar minerals with considerable chemical variation.

- ⋆ Other 2:1 clay types exist such as sepiolite or attapulgite, clays with long water channels internal to their structure.

In clays the tetrahedral sheets are always bonded to octahedral sheets formed from small cations, such as aluminium or magnesium, coordinated by six oxygen atoms. The unshared vertices from the tetrahedral sheet also form part of one side of the octahedral sheet but an additional oxygen atom is located above the gap in the tetrahedral sheet at the center of the six tetrahedra. This oxygen atom is bonded to a hydrogen atom forming an OH group in the clay structure.

Depending on the composition of the tetrahedral and octahedral sheets, the layer will have no charge, or will have a net negative charge. If the layers are charged this charge is balanced by inter-layer cations such as Na^+ or K^+. In each case the inter-layer can also contain water. The crystal structure is formed from a stack of layers interspaced with the inter-layers.

We distinguish natural and synthetic clays. Natural clays are mined and refined prior to use. This causes a difficulty with repeating exact structure, even when two clays are classified to be of the same class. They are only identical if mined from the same location and mineral vein and even in such cases there can be some differences. [65]

Another group are synthetic clays, who are also layered silicates, but there is more control in the chemical structure, aspect ratio, cation exchange capacity and trace elements. They can be reproduced in the same form, if the production conditions are retained. It places them ahead of natural clays. Their drawback is a higher price.

3.1.2   Laponite

Laponite is synthetic magnesium silicate produced by Rockwood Additives, widely used as filler and thickening agent.[56] Laponite platelets are nanometer-scale disks with 1:25 aspect ratio (see Figure 3.3). The faces of the platelet are negatively, while the rim positively charged. It is a mineral clay, which is characterized by a layered structure, which closely resembles the natural clay mineral hectorite. It is built up of sheets of octahedrally coordinated magnesium oxide placed between two parallel sheets of tetrahedrally coordinated silica (see Figure 3.4).
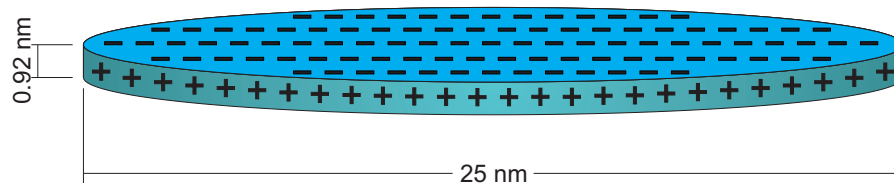
Figure 3.3: Single Laponite platelet.

The empirical formula is as follows:

$$Na^{+0.7} + [(Si_8Mg_{5.5}Li_{0.3})O_{20}(OH)_4]^{-0.7}$$
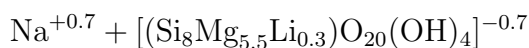
Dried Laponite form crystals, where the Laponite disks are arranged into stacks held together electrostatically by sharing of sodium ions in the inter-layer region between

adjacent crystals (see Figure 3.4). When dispersed in a polar solvent, like water, the weak bonds are easily broken as the solvent penetrates into the inter-layer regions. Consequently, the layered structure is separated into primary platelets, as described above. [84]

Laponite-Laponite interactions are of different kinds—van der Waals attraction, complex electrostatic interaction, which can be either repulsive (rim-rim, face-face) or attractive (rim-face). [78]

The graph was removed because of copyright restrictions.

Figure 3.4: Idealized structural formula of Laponite. [86]

3.2 Aging of a Laponite suspension

When diluted enough a Laponite suspension appears to be a liquid, but when on a large range of volume fraction, the suspension exhibits a very slow dynamics that evolves with the time elapsed since the preparation of the solution. This slow dynamics depends on Laponite as well as salt concentration.

As it is a prerequisite to understand this behavior before a detailed analysis of Laponite's phase diagram, I firstly describe its dynamics.

Aging evolution of the suspension is observable both in the static organization of the particles and in their dynamics.

3.2.1 Description and discussion of dynamic light scattering

In dynamic light scattering system the sample is illuminated by a laser beam and the fluctuations of the scattered light are detected at a known scattering angle θ by a fast photon detector, as shown in Figure 3.5.
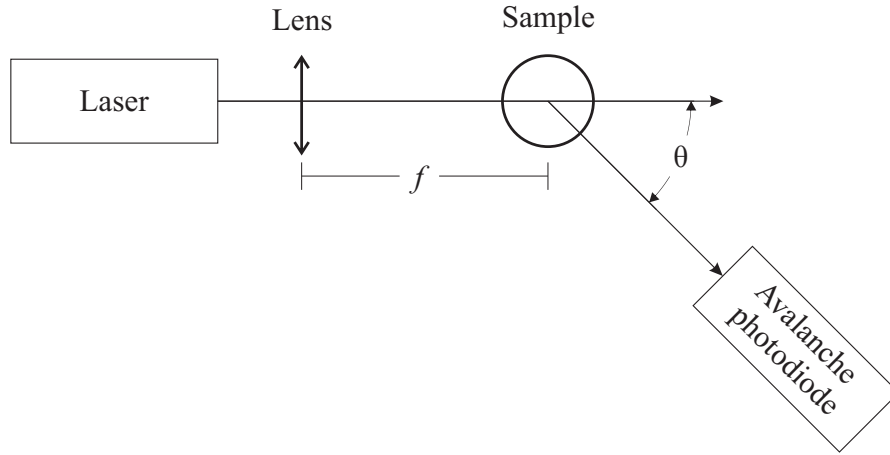

Figure 3.5: Dynamic light scattering (DLS) scheme. f is the focal distance of the lens.

The particles scatter the light and in that way mark information about their motion. Analysis of the fluctuation of the scattered light thus yields information about the particles. Experimentally one characterizes intensity fluctuations by forming the intensity correlation function:

$$g_2(q,t) = \frac{\langle I(q, t + \tau) I(q, \tau) \rangle_\tau}{\langle I(q, \tau) \rangle_\tau^2} \tag{3.1}$$

where $\langle ... \rangle$ is the temporal average over τ and q is the modulus of the scattering wave vector defined as:

$$q = \frac{4\pi n}{\lambda_0} \sin\left(\frac{\theta}{2}\right) \tag{3.2}$$

where n is the index of refraction of the solvent and λ_0 the laser wavelength in vacuum.

If the particles' motion is Brownian, the analysis of the intensity correlation function

provides the diffusion constant of the particles and we have:

$$\sqrt{g_2(q,t) - 1} = e^{-q^2 Dt} \qquad (3.3)$$

The diffusion constant D is then related to the radius R of the particles by means of the Stokes-Einstein equation:

$$D = \frac{kT}{6\pi R\eta} \qquad (3.4)$$

where k is the Boltzmann constant, T the temperature and η the viscosity of the solvent.

Ruzicka *et al.* [73] used dynamic light scattering to follow the dynamics of a Laponite suspension. They carried out the experiment using a goniometer fitted with a toluene bath. The laser was a 30 mW diode-pumped, frequency-doubled neodymium-doped yttrium aluminum garnet (Nd:YAG) ($\lambda = 532$ nm). The scattered intensity was recorded with an avalanche photodiode, $\theta = 90°$ and the acquisition time of each $g_2(q,t)$ was 120 s.

Due to the finite non-zero size of the detector, the limit of $g_2 - 1$ when t goes to 0 is smaller than 1. We will call its value the coherence factor b.

The sample ages for every concentration of a Laponite suspension, even very low. This aging manifests as a slowing down of the decorrelation function. At short t_{w}, the characteristic decay time τ_1 increases (see Figure 3.6).

Then, a slow mode of relaxation appears and the results may be fitted with equation:

$$g_2(q,t) - 1 = b \left[ae^{-t/\tau_1} + (1-a)e^{-(t/\tau_2)^\beta} \right]^2 \qquad (3.5)$$

where b represents the coherence factor. The fast (short-time) relaxation mode is described by the exponential factor and characteristic time τ_1, while the slow (long-time) relaxation mode by the stretched exponential factor with coefficient β and time τ_2. β is measured to be of a value 1.35, [63] so β is greater than unity. This means that the long time dynamics of the Laponite is hyperdiffusive. [59] Although the origin of this

The graph was removed because of copyright restrictions.

Figure 3.6: Evolution of the time autocorrelation functions as a function of the waiting time t_w (same waiting times, same lines styles) for two different Laponite concentrations: a low one, $C_w = 1.9\%$ (A) and a high one, $C_w = 2.8\%$ (B). Experiments are performed with Nd:YAG (532 nm) laser at $\theta = 90°$. [73]

behavior is not fully understood, it has been assumed that it is due to the long time relaxation of localized stress accumulated inside the sample. [61]

The evolution of τ_1 depends on the concentration. At high concentrations τ_1 is constant, while at the low ones it increases with increasing t_w.

At some time a qualitative change in the correlation function is observed. When the time tends to the infinity, the correlation function does not tend to 0, meaning a transition to a non-ergodic, dynamically arrested state. [78]

A non-ergodic state takes place when Laponite platelets positions remain correlated to their organization 10^3 ms sooner. It means that the platelets are not able to move by $q^{-1} \simeq 45$ nm during 10^3 ms. On this timescale they are trapped in a particular configuration and cannot explore the overall particular landscape.

Depending on the concentration, τ_2 exhibits two different behaviors (see Figure 3.7). At low concentration, τ_2 diverges in a finite waiting time t_{w}, meaning that the sample reaches a stationary state and in a gel phase. On the contrary at high concentration, τ_2 continues to evolve with t_{w} as τ_2 is proportional to $e^{t_{\mathrm{w}}}$ (Figure 3.7, $C_{\mathrm{w}} = 2.5\%$). The sample thus continues to evolve with t_{w} and an exponential aging is observed.

Nevertheless, these measurements do not allow to study sample dynamics slower than 1 s and a full aging regime, in which τ_2 is proportional to t_{w} is not observed. Experiments on longer time scales have been performed using multispeckle dynamic light scattering.

The graph was removed because of copyright restrictions.

Figure 3.7: Waiting time dependence of τ_2, i. e., of the average relaxation time of the slow decay of the correlation functions. As an example, the t_{w} dependence of τ_2 is reported for the three indicated concentrations. [67]

In this setup [83] a thin sample is illuminated by an expanded incident laser beam as in Figure 3.8, forming an angle θ with the sample. Any particle inside the beam will diffuse light. The diffusion wave vector is selected by an afocal system of two lenses and a pinhole located at their focal point.

Under these conditions every pixel of the CCD camera sees different diffusive volume with the same vector q.

Then the dynamics of the sample is obtained by computing the overall average correlation function of the intensity collected by the CCD:
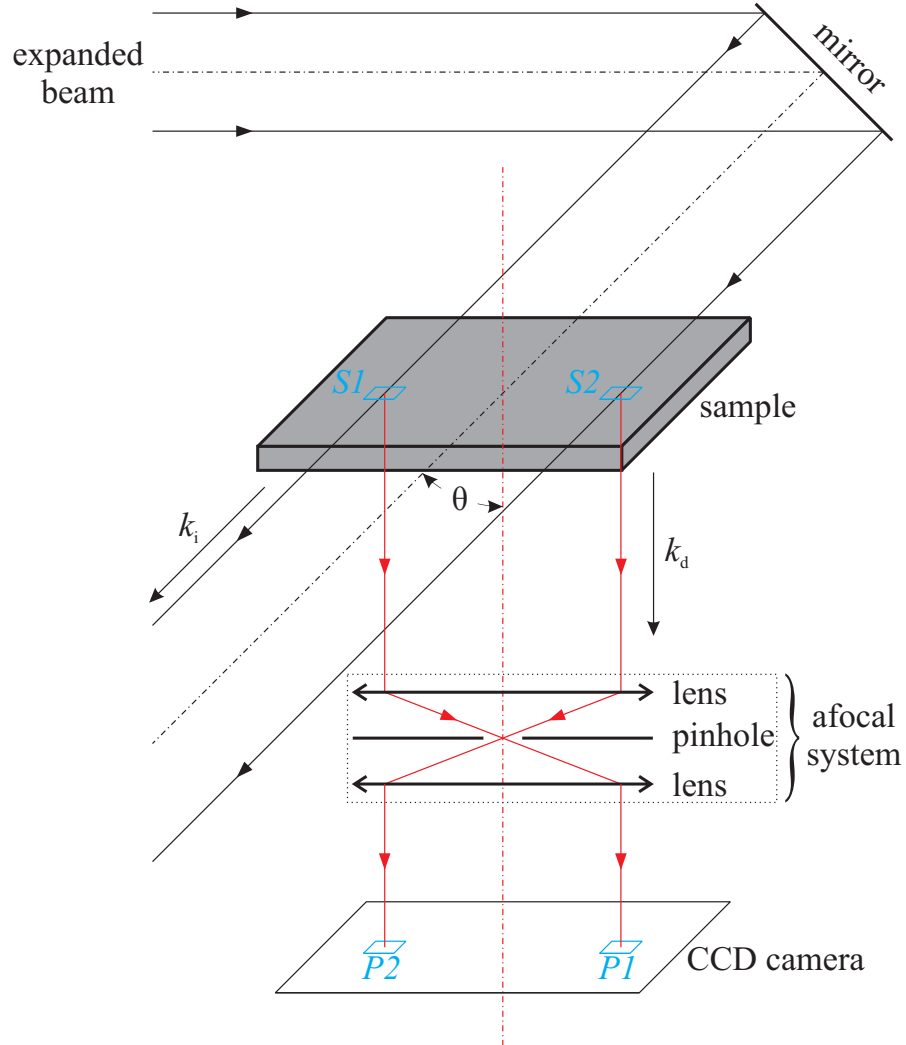
Figure 3.8: Scheme of the setup for small angles. The widened incident angle illuminates the sample. The incidence angle is of the order of few degrees. k_i is the incident wave, k_d is the diffused wave, θ is the incidence angle, Sx is the xth source point/region, Px is the xth pixel. [83]

$$g_2(t) = \frac{\langle I_p(0) I_p(t) \rangle_p}{\langle I_p(0) \rangle_p \langle I_p(t) \rangle_p} \tag{3.6}$$

where $\langle ... \rangle_p$ is the average over the pixels.

This setup allows to have access to very long time-scales (up to several hours).

One observes a transition between two long times dynamics, as shown on Figure 3.9.

The graph was removed because of copyright restrictions.

Figure 3.9: Evidence of two distinct aging regimes: exponential aging and full aging. Data are obtained on a 1.36% Laponite volume fraction sample at $\theta = 30°$. [63]

At short ages, the exponential aging is recovered, but at longer ages, an aging process in which τ_2 is proportional to t_w is observed. This is so-called full aging, characteristic of glassy dynamics.

3.2.2 Evolution of the static structure factor $S(q)$

One may observe the evolution with t_w of the organization of the platelets. Static light scattering [69] and X-ray [73] experiments revealed that as time passes structures of higher and higher characteristic sizes develop for low concentration solutions ($C_w < 2\%$ [73]).

As shown on Figure 3.10C there is an evident change of the static structure factors as the sample ages and approaches non-ergodic state. Figure 3.11 shows that the excess of scattering at low q increases as the Laponite concentration decreases. This indicates the existence of strong inhomogeneity in the suspension, which is attributed by Ruzicka *et al.* [73] to the formation of a network, which grows with increasing aging time and eventually forms a gelled network.

On the contrary, for high concentration solutions, the static factor does not exhibit any increase at low q. Thus, at times long enough, Laponite suspension behave as:

The graph was removed because of copyright restrictions.

Figure 3.10: Evolution of the measured structure factors as a function of the waiting time t_w (same waiting times, same lines styles) for two different Laponite concentrations: a low one, $C_w = 1.9\%$ (C) and a high one, $C_w = 2.8\%$ (D). [73]

The graph was removed because of copyright restrictions.

Figure 3.11: Waiting time evolution of the static structure factors from full $[f(q, \infty) = 0]$ to incomplete decay $[f(q, \infty) \neq 0]$ in the corresponding DLS spectra for three different low Laponite concentrations at $t_w \approx 1.2 t_w^\infty$. [73]

$\star$ stationary gels at low q, possessing long range heterogeneities,

$\star$ out of equilibrium glasses at high q, which appear to be more heterogeneous as seen with static light scattering or coherent X-ray experiments.

Above differences between low and high Laponite concentration samples are proof that both samples are reaching the final non-ergodic states following different routes. It also means that the final arrested states are actually different.

3.3 Phase diagram

Despite its complexity, it is believed that there is enough agreement between results from several groups to be able to establish a phase diagram at long waiting times, if salt concentration and Laponite concentration are known.

The graph was removed because of copyright restrictions.

Figure 3.12: New phase diagram of Laponite suspensions proposed in this review collecting data from different authors obtained with different techniques for large enough waiting time. Note that SIM refers to numerical simulations.[78]

Ruzicka *et al.* [78] constructed a unified phase diagram of Laponite suspensions (see Figure 3.12), dependent on three parameters—clay concentration, salt concentration and waiting time.

For the samples with salt free water ($C_s = 10^{-4}$ M) one can distinguish four regions, depending on clay concentration:

- For $C_w \leqslant 1.0\%$ there is an extremely slow phase separation between clay-poor and clay-rich phase. [77]

- For $1.0\% < C_w < 2.0\%$ a gel state, caused by attractive interactions between platelets is observed. [69, 73, 74, 77]

- For $C_w \geqslant 1.0\%$ one finds a glassy state, which is dominated by repulsive interactions, called a Wigner glass. [76]

- For $C_w \gtrsim 1.0\%$ the formation of a nematic phase has been reported. [58]

This description is valid for low salt concentration, up to $C_s = 2$ mM. At higher concentrations, between 3 mM and 20 mM, the results are inconclusive, displaying features of both gel and glass. The higher clay concentrations has not been thoroughly studied, because of the immediate arrest of the samples. For salt concentrations higher than $C_s = 20$ mM there is a phase separation in the form of flocculation or sedimentation of large aggregates. [58, 69] A phase separation was discovered for wide range of salt concentrations down to $C_s = 1$ mM for very low clay concentrations ($C_w < 0.3\%$). [69]

Both gel and glassy arrested states can be found by changing the clay concentration. The origin of these states is assigned to dominant attractive and repulsive interactions, both being present in the Laponite suspensions. Attraction is more common at low and intermediate concentrations, eventually resulting in a phase separation.

3.4 Diffusion of probe particles

Laponite displays aging dynamics with hyperdiffusive characteristics. It has been assumed that this dynamics is associated with spatial heterogeneities and that stored heterogeneities are responsible for it. [61]

One way to study Laponite dynamics more accurately is to look at the diffusion of the probe particles. [64, 68, 74] Most studies chose probe particles much larger than the Laponite discs. For example, heterogeneous behavior of 1 μm probe particles has been observed. [74]

Nevertheless, quantitative analysis of the dynamics of the probe particles requires a fine understanding of the coupling between the particles and the medium. [60, 66] In particular, most studies assume that the probe particles are larger than the largest spatial heterogeneities scale of the studied continuous medium and very little is known about the influence of the tracer size on its observed dynamics, when its size is of the order of the Laponite structure heterogeneity.

Petit *et al.* [75] studied the motion of the colloidal particles, ranging from 25 nm to 100 nm, in Laponite glass.

They performed Fluorescence Recovery After Photobleaching (FRAP) experiment.

The setup used by this group is shown in Figure 3.13. The general idea of the measurement is to photobleach the fluorescence of tracers in a small region of the sample by an intense laser. The recovery of the fluorescence signal as unbleached tracers diffuse into the bleached area is then measured by a much weaker laser beam. With the imaging beam they image the imprinted photobleaching pattern as a function of time.

The beam of an 488 nm Ar$^+$ laser (2 W power) is divided into a photobleaching and an imaging beam by a 90%/10% beam splitter. The photobleaching beam passes a cylindrical-spherical lens system to create a horizontal laser sheet of a linear bleached region whose width is 110 µm at the location of the sample cell.

The imaging beam is attenuated by half-wave plate combined with a Glan-Taylor polarizer before passing through a spatial filter and being enlarged to provide uniform illumination at the scale of the observed sample region. This region is monitored by a CCD camera.

This technique allows to study the motion of the particles over large length- and time-scales. Typically the fastest motion detected by the authors is a diffusion motion of the order of 10 µm during a few seconds.

The authors obtain the long time diffusion coefficient of the probe particles (for samples aged more than a few days). For the largest studied particles (65 nm and 100 nm), no motion is observed, $D_\infty = 0$. Then, smaller particles (25 nm and 37 nm) are observed to diffuse with a diffusion coefficient that decreases with Laponite concentration (see Figure 3.14).

The slowdown of the colloidal probes dynamics is explained by the authors by the decrease of the particles mobility due to their confinement inside Laponite structure

The graph was removed because of copyright restrictions.

Figure 3.13: Fluorescence Recovery After Photobleaching (FRAP) setup. [75]

porosity.

From this article it may be concluded that the long time diffusion coefficient of colloidal probes in a Laponite suspension is:

* ⋆ Null, if the diameter of the particles is larger than the pore size of the Laponite suspension, d depends as:

The graph was removed because of copyright restrictions.

Figure 3.14: Evolution of the normalized diffusion coefficient, $D_\infty^* = D_\infty(c)/D_0$, of colloidal tracers in Laponite, as a function of the concentration of Laponite for various tracer sizes: ($\Diamond$) 1 nm fluorescein molecules; ($\triangle$) 25 nm diameter colloids; ($\square$) 37 nm diameter colloids; (∇) 65 nm diameter colloids; ($\bigcirc$) 100 nm diameter colloids. [75]

$$d = (6/\pi)^{1/3} \left(\rho_{\text{lap}}\nu/\rho_{\text{glass}}\right)^{1/3} c^{-1/3} \tag{3.7}$$

where ν is the volume of a Laponite disk, ρ_{lap} is the density of the Laponite disks, ρ_{glass} is the density of the Laponite solution and c is the Laponite mass concentration.

$\star$ Equal to that of a particle moving between two parallel planes, whose distance is equal to d.

We are interested in the motion of the probe particles over length-scales of much smaller than those probed by this technique and wish to study particles' motion at the length-scale of the order of their size.

Chapter 4
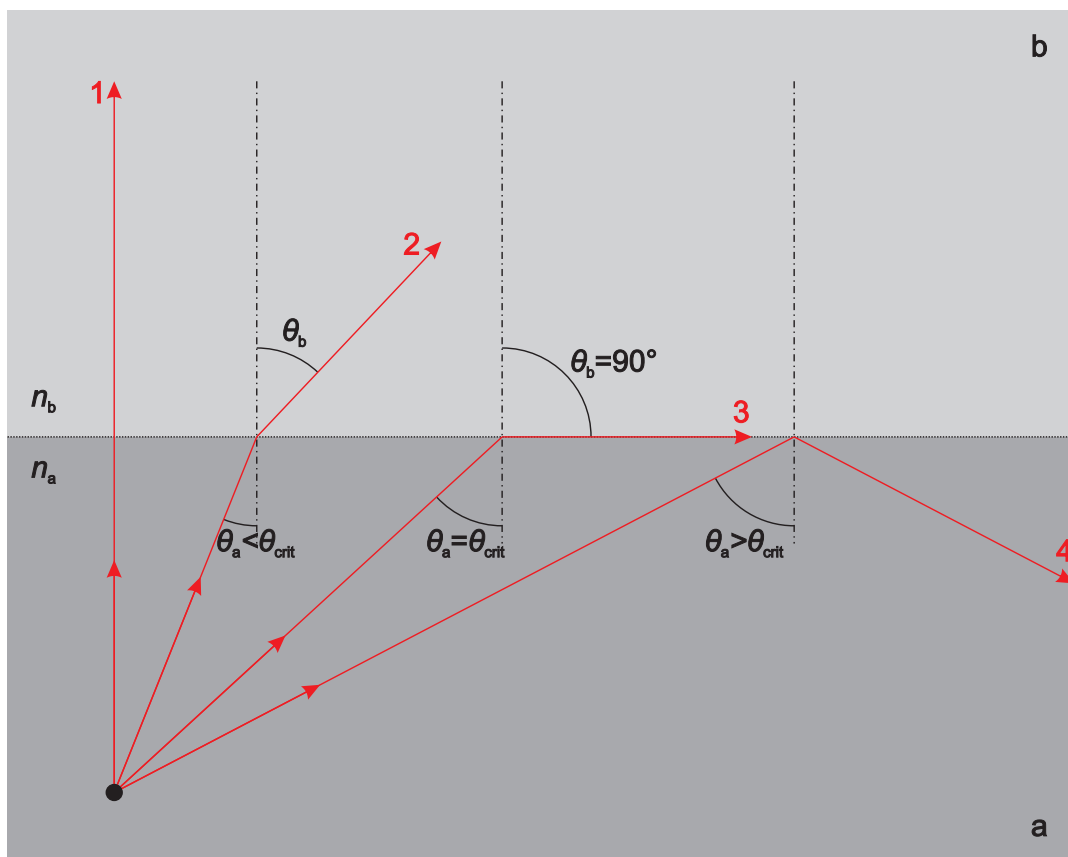
Experiment

4.1   Total internal reflection

Figure 4.1: Total internal reflection. n_a and n_b $(n_a > n_b)$ are refractive indexes for materials a and b.

When light propagates from a medium of high index of refraction into a medium of lower index of refraction, there is a possibility that all of the light can be reflected back from the interface. Figure 4.1 shows several rays radiating from a source in material a with index of refraction n_a. The rays reach the surface of material b with index n_b, where $n_a > n_b$. The Snell's law of refraction tells that:

$$n_a \sin \theta_a = n_b \sin \theta_b \tag{4.1}$$

Consequently:

$$\sin \theta_b = \frac{n_a}{n_b} \sin \theta_a \tag{4.2}$$

Because n_a/n_b is greater than 1, $\sin \theta_b$ is larger than $\sin \theta_a$. So there is a value of θ_a less than 90° for which Snell's law gives $\theta_b = 90°$. The angle of incidence for which the angle of refraction is 90° is called the critical angle (θ_{crit}, see Figure 4.1, ray 3).

To find θ_{crit} for given materials one sets $\theta_b = 90°$ ($\sin \theta_b$) in Snell's law. Then:

$$\sin \theta_{crit} = \frac{n_b}{n_a} \tag{4.3}$$

Total internal reflection occurs if the angle of incidence θ_a is greater than or equal to θ_{crit}.

4.2   Evanescent wave

Because the tangential component of the electric and the normal component of the magnetic fields cannot be discontinuous at a boundary, there must exist an electromagnetic field in the medium with low index of refraction. Evanescent wave is a name for such a field penetrating a small distance into second material and propagating parallel to the surface in the plane of incidence.

Evanescent waves are formed when sinusoidal waves are internally reflected from the interface between two materials at an angle greater than the critical angle θ_{crit} so that total internal reflection occurs. The intensity of evanescent waves decays exponentially with perpendicular distance z from the interface at which they are formed:

$$I(z) = I_0 e^{-z/d} \tag{4.4}$$

where:

$$d(\theta_{\text{a}}) = \frac{\lambda_0}{4\pi} \left(n_{\text{a}}^2 \sin^2 \theta_{\text{a}} - n_{\text{b}}^2 \right)^{-1/2} \tag{4.5}$$

for angle of incidence $\theta_{\text{a}} > \theta_{\text{crit}}$ and light wavelength λ_0. Figure 4.2 shows the penetration depth d as a function of incidence angle θ_{a}. d goes to infinity for angle smaller than θ_{crit}.
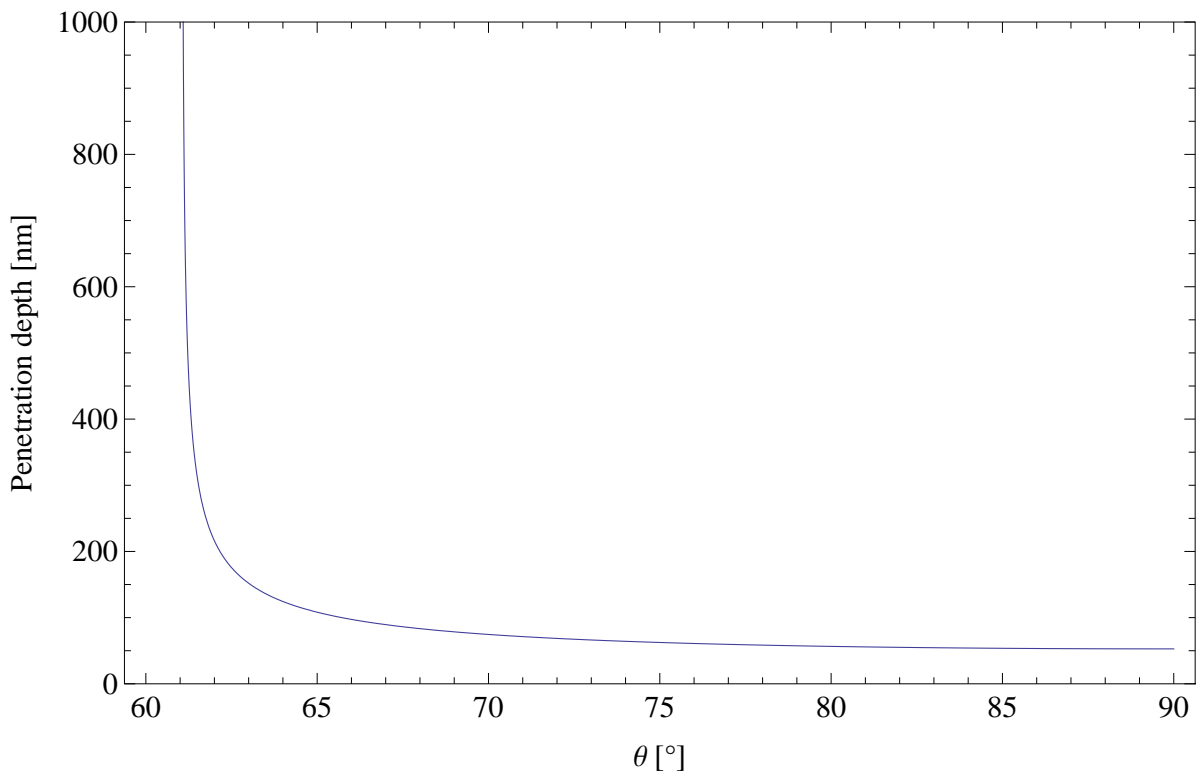
Figure 4.2: The penetration depth as a function of incidence angle θ_{a}. $\lambda_0 = 488$ nm, $n_{\text{a}} = 1.52$, $n_{\text{b}} = 1.33$.

For θ_a approaching θ_{crit}, $d \to \infty$, but in general situation, d decreases with increasing θ_a and is on the order of λ_0 or smaller. I_0 is the intensity at $z = 0$ depends on both the incidence angle θ_a and the incident beam polarization. For incident electric field intensities $\mathcal{I}^{\parallel,\perp}$ with polarizations parallel and perpendicular, respectively, to the plane of incidence, the evanescent intensities $I_0^{\parallel,\perp}$ are: [55]

$$I_0^{\parallel} = \mathcal{I}^{\parallel} \cdot \frac{4\cos^2\theta(2\sin^2\theta - n^2)}{n^4\cos^2\theta + \sin^2\theta - n^2} \tag{4.6}$$

$$I_0^{\perp} = \mathcal{I}^{\perp} \cdot \frac{4\cos^2\theta}{1 - n^2} \tag{4.7}$$

where $n = n_b/n_a < 1$.

Figure 4.3 illustrates $I_0^{\parallel}$ and $I_0^{\perp}$ as functions of θ. $I_0^{\parallel}$ is more intense for whole range of θ and they both approach zero when $\theta \to 90°$.

4.3   Total internal reflection fluorescence microscope (TIRFM)

Total internal reflection fluorescence microscope takes advantage of the total internal reflection phenomenon and use of fluorescent samples. The portion of the specimen within the evanescent field can be excited to emit fluorescence. Only fluorophore molecules very near the surface of a specimen are excited to emit, creating an extremely thin optical section. The key advantage of TIRFM is the shallow penetration depth of the evanescent wave. Thus x-y resolution of a TIRFM image is equal to the resolution of a standard fluorescence microscope image, but z resolution may be much higher, as it is equal to d. Moreover, the evanescent intensity exponentially decays with the distance form the surface, z. This effect leads to images of very high contrast having a good signal-to-noise ratio.

There are two most common TIRFM setups—with illumination side prism and through the lens illumination (see Figure 4.4).

The setup with prism is easy to build, since it requires only the microscope, prism and laser. The drawback for this setup is the requirement that the specimen be positioned between the prism and the microscope objective.

The setup through the objective lens illumination requires that the laser be intro-
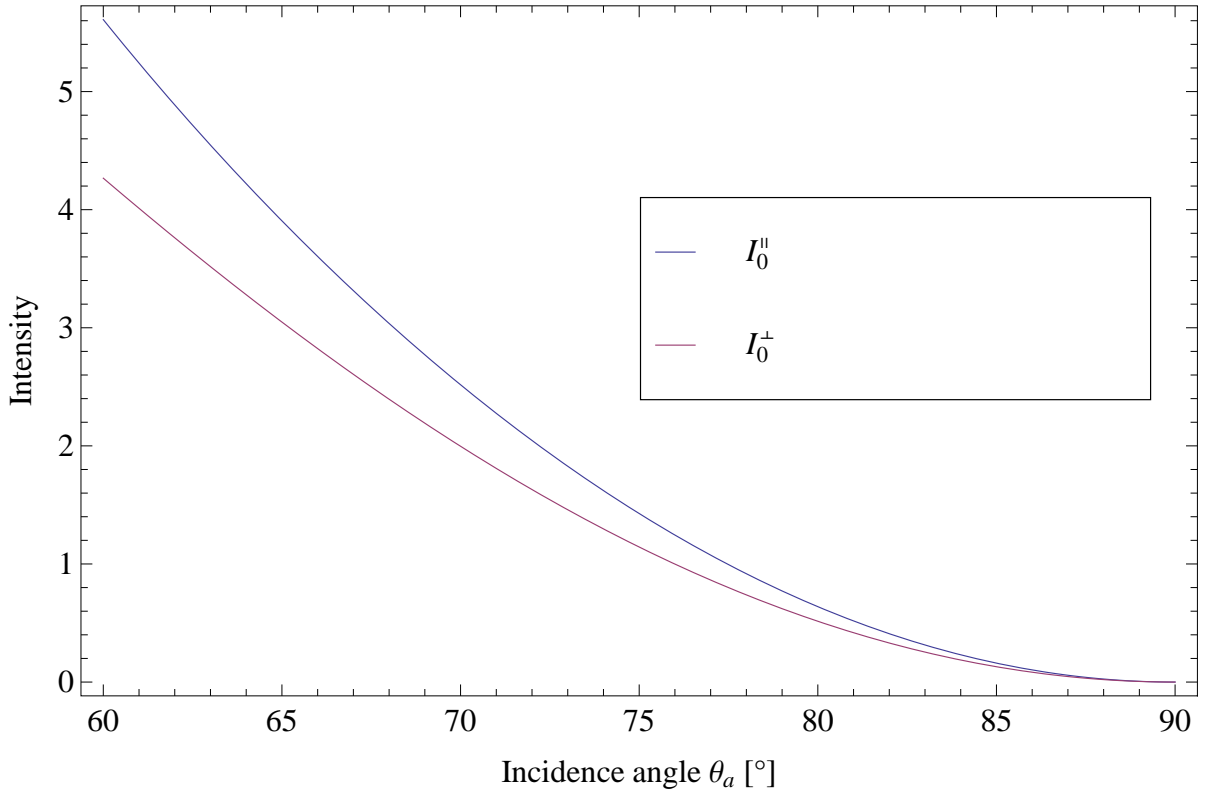
Figure 4.3: Intensities $I_0^{\parallel,\perp}$ vs incidence angle θ, for $n = 1.33/1.52 = 0.875$, corresponding to a critical angle of $\theta_{\mathrm{crit}} = 61.04°$. Intensity is expressed as the ratio of evanescent intensity at $z = 0$ to the incident intensity for each polarization.

duced through the microscope. The specimen is located in a way that permits the user to access the sample at the time of the experiment.

4.4   The experimental setup

To perform these experiments I used objective-based Total Internal Reflection Fluorescent Microscope (TIRFM). The objective used was Olympus PLAPON 60XOTIRFM, with high numerical aperture, N.A. = 1.45. The laser was Coherent Sapphire 488 LP with wavelength $\lambda_0 = 488$ nm. Refractive indexes were 1.48, 1.52 and 1.33 for immersion oil, cover slip and sample, respectively.

We want to select one wave vector incidence angle θ_{a} at the surface of the cover slip. We do not illuminate the microscope objective with a parallel beam, but with a beam
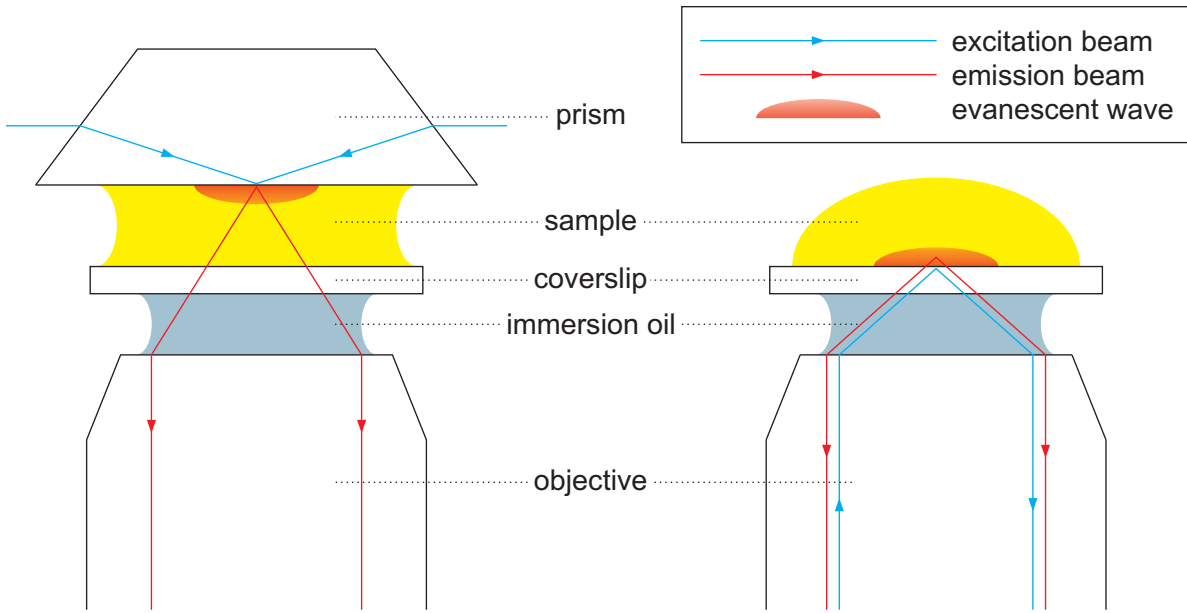
Figure 4.4: Scheme of prism- (left) and objective-based (right) TIRFM.

that converges at the back focal plane of the objective.

Thus, the propagating beam in the object space is a collimated beam and only one incident wave vector is selected, leading to a monoexponential decay of the evanescent field in the sample.

We use a converging lens of focal length $f = 300$ mm to focus the beam onto the back focal plane of the microscope objective. This lens is not coaxial with the objective. The radial displacement of the lens allows us to control the output angle of the collimated beam.

The sample is imaged by the same microscope objective together with a tube lens of $f = 180$ mm, so that the overall magnification of the microscope is $60\times$.

We followed a region of 350×40 pixels (see Figure 4.6) on Princeton PhotonMAX 512B CCD camera. One pixel size is 16×16 µm. The objective used has a magnification factor of $60\times$. That means one pixel corresponds to 266.7×266.7 nm of the sample. The region we observed is therefore of 93.3×10.7 µm.

We have used three sizes of the beads: 20, 40, and 100 nm. Thus, the diameter of the Laponite particle is larger than the smallest bead and smaller than the two other studied particles. The solutions were diluted to receive the same number of beads in a volume unit (~ 10 in selected region).
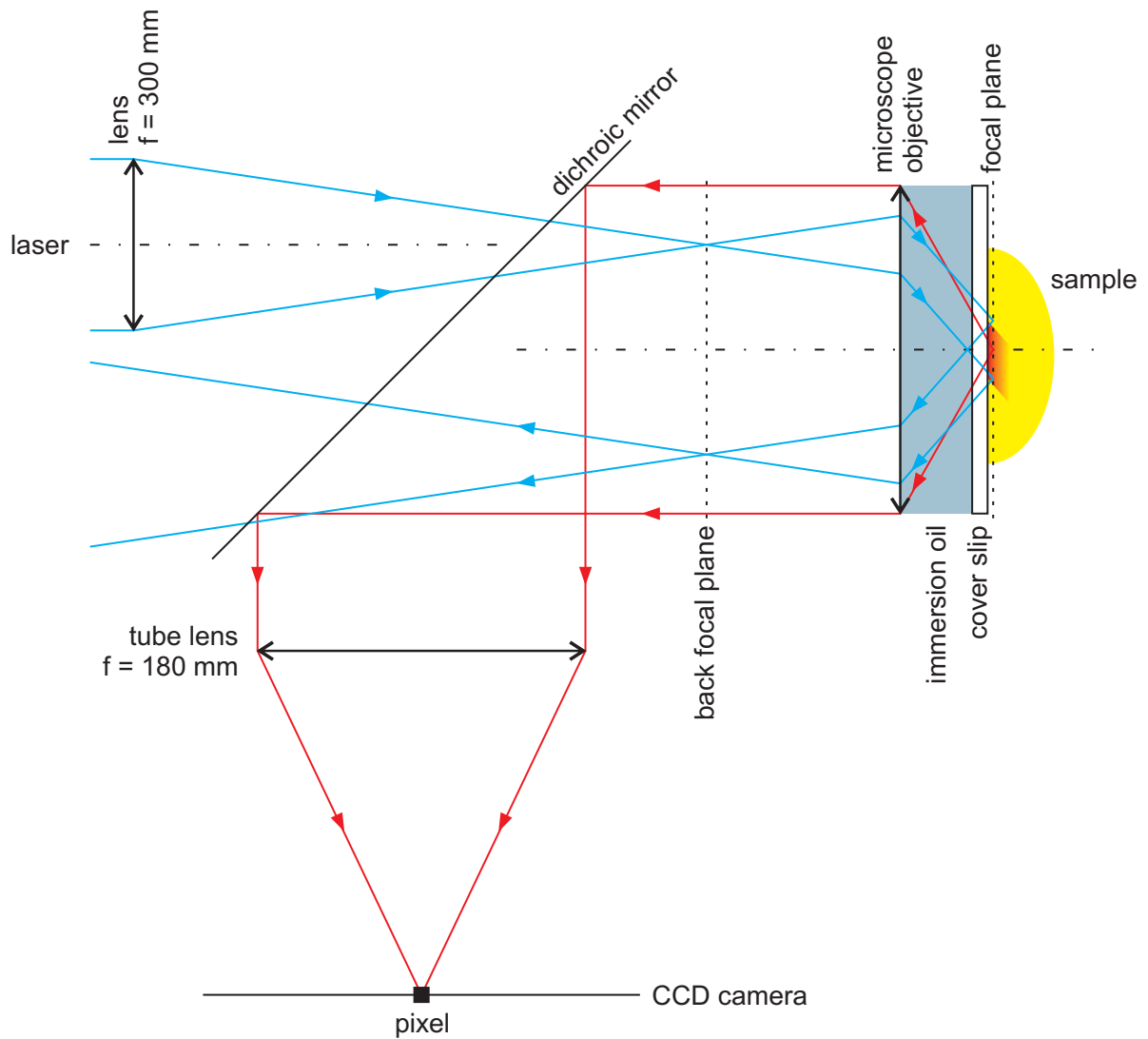
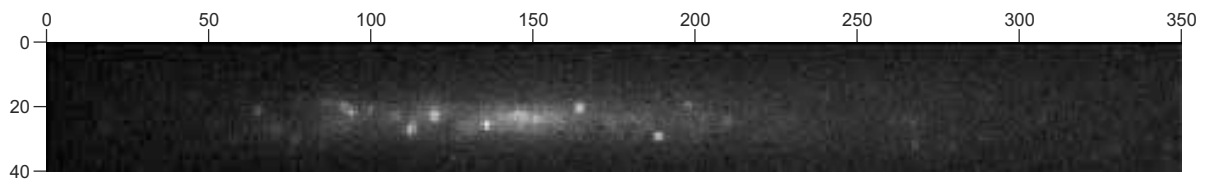**Figure 4.5:** The experimental setup scheme.

Figure 4.6: Example image of typical frame of size 350×40 pixels.

4.5 From the raw to the binarized image

The data we receive from the CCD camera is of a form of 350×40 pixels 16-bit frames, providing us with 65536 intensity levels. The exposure time is 0.25 s per frame. The

avalanche gain of the CCD camera is 1000. One cannot increase gain, without increasing noise level. Typical contrast is very low (contrast $C = \frac{\langle I^2 \rangle_{\mathrm{p}}}{\langle I \rangle_{\mathrm{p}}^2}$, where $\langle \rangle_{\mathrm{p}}$ is the average over the pixels) and may vary a lot from one image to the other (see Figure 4.7). The particles cannot be easily identified in the raw image.
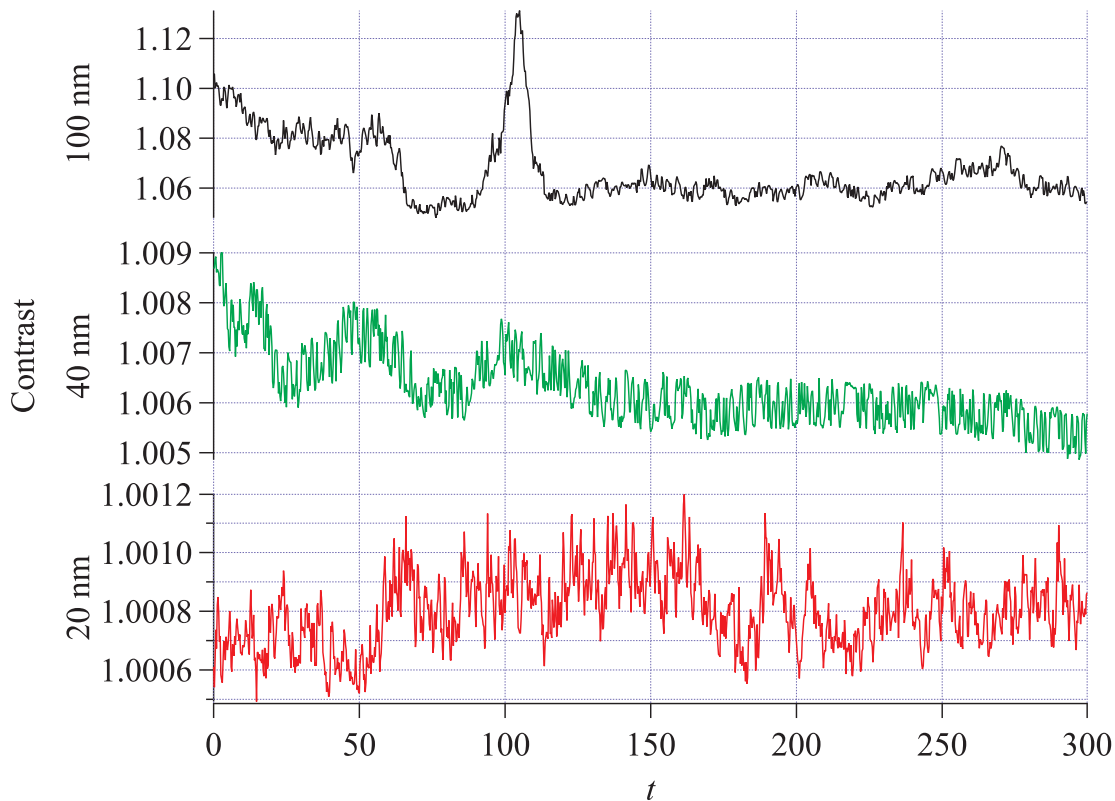

Figure 4.7: Example contrast variations for 20, 40, and 100 nm diameter beads.

To perform an analysis we needed to filter the data in order to retrieve the information from it. We were looking for a given number of pixels which were most intense in whole image.

Figure 4.8 shows the differences between three kinds of representation of the results:

⋆ data presented as grayscale image,

⋆ 50 most intense pixels cut-off with their real values preserved,

⋆ 50 most intense pixels cut-off binarized—with only two states, black and white.
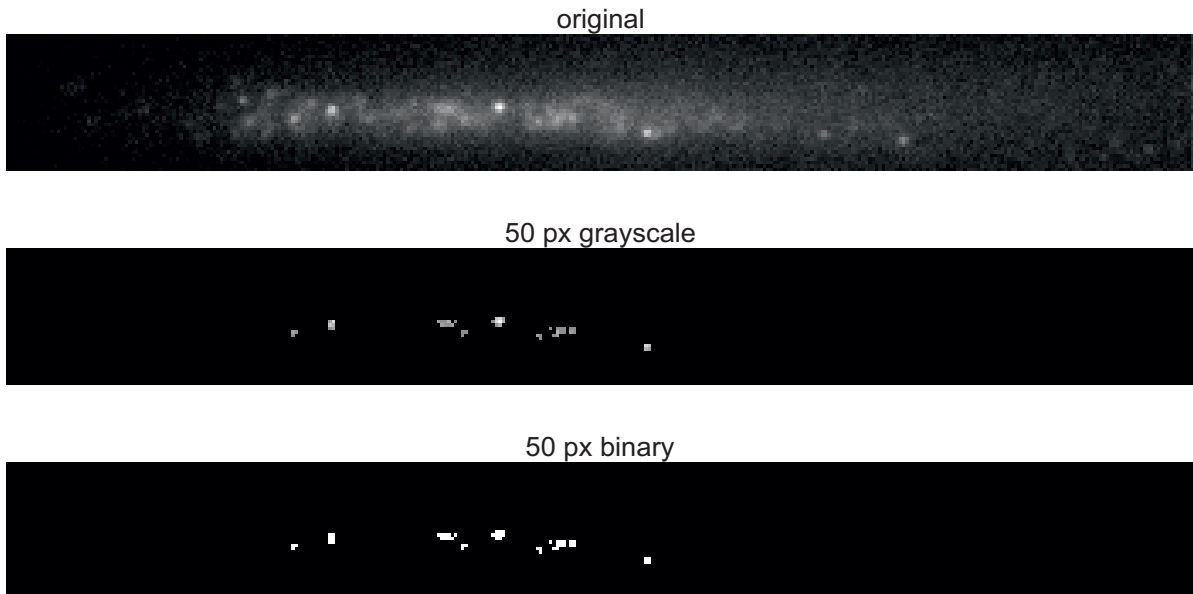
original

50 px grayscale

50 px binary

Figure 4.8: The original grayscale image (upper) and 50 most intense pixels in grayscale (middle) and binary (lower) versions. The chosen pixels in grayscale image have the values from the original image, while the same pixels in the binary image have the value of 1. Example for 20 nm particles.

We firstly need to get rid of the dark noise and thus wish to threshold the image. Because the values range differs from image to image we could not set a fixed value. For the contrast fluctuates we were unable to use a relative choice of the threshold level. Indeed, for setting a threshold to be a function of $I_\mathrm{max} - I_\mathrm{min}$ would lead to a huge variation of the pixels number between images. Thus we needed to choose another criterion of selection. Because the number of particles in the field of view should be constant whatever the optical alignment is, we decided to select a number N of the most intense pixels in each image. N value was chosen so that the number of objects is of the order of the number of particles in the observed volume.

Figure 4.10 shows the binary images with different number of most intense pixels marked—25, 50, 75, 100 and 200. The size of objects is increasing with the number of pixels selected, as shown in Figure 4.9.

We do not try to identify the particles and to follow them, but will develop a way to study the pixel dynamics. Then we will come back to the particle dynamics.
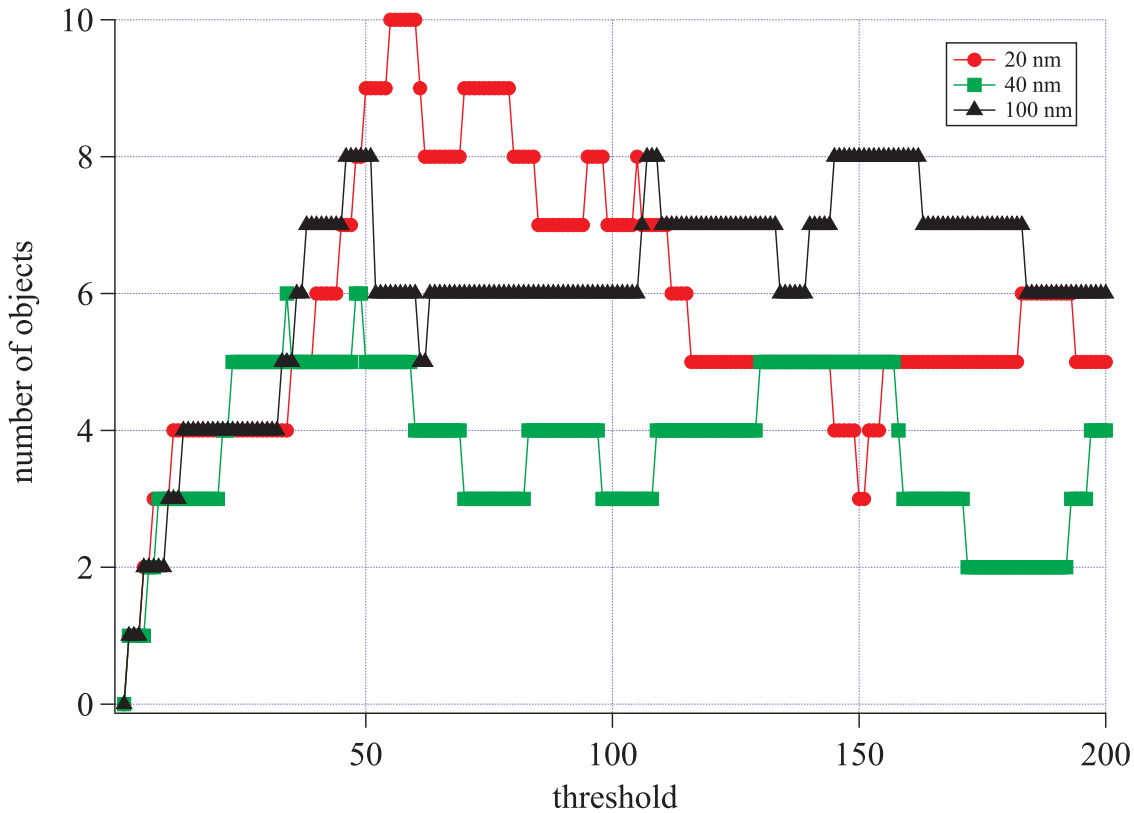
Figure 4.9: Number of objects as a function of threshold.

4.6 Characterization of the pixels dynamics

One way to characterize the pixel dynamics is to measure the distribution of lifetime of the pixels $\rho(\tau)$.

In order to do so, we compute a temporal correlation function defined by:

- Pick up a reference image

- For any time t count the number of pixels that remained illuminated between first image and time t.

I will call 1 the value of an illuminated pixel and 0 that of switched-off pixel. $C(t)$ is the probability that a given pixel, which was 1 at time $t = 0$, remains 1 during the interval $[0, t]$, as shown in Figure 4.11. $C(t)$ is related to $\rho(\tau)$ according to:
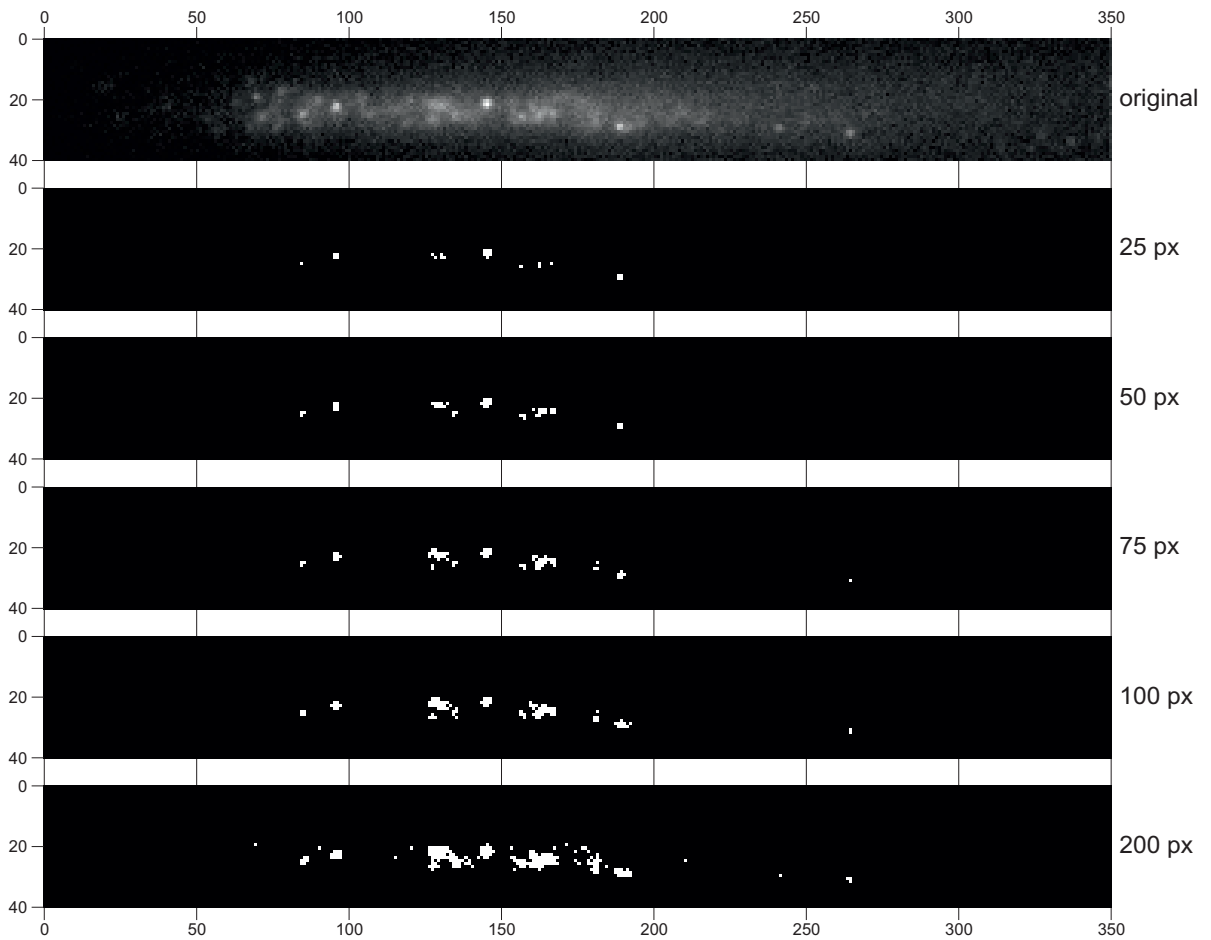
Figure 4.10: Comparison between binary images with 25, 50, 75, 100 and 200 most intense pixels. Example for 20 nm particles.

$$C(t) = \int_0^\infty \rho(\tau) \mathrm{P}(t|\tau) d\tau \tag{4.8}$$

where $\mathrm{P}(\delta t|\tau)$ is the probability that a pixel, whose lifetime is τ, which was illuminated at $t = 0$ is still illuminated at time δt. As shown in Figure 4.12 the probability for a pixel that was illuminated at time $t = 0$ to be still excited at time δt is the ratio of the red region over τ:

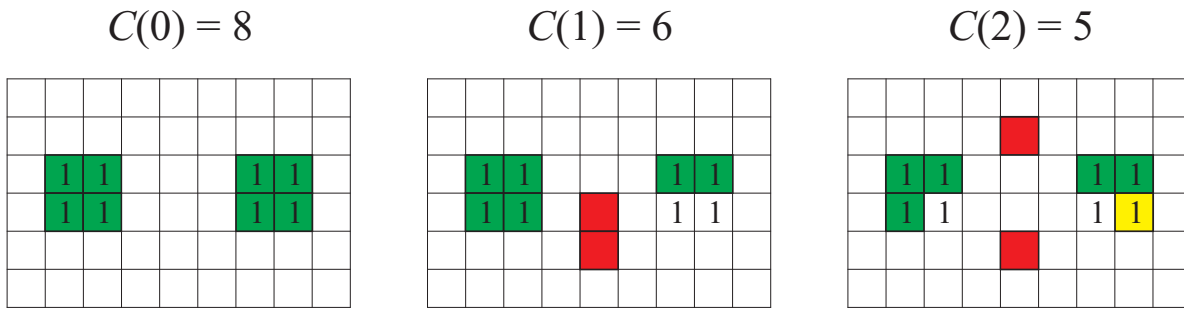$$C(0) = 8 \qquad\qquad C(1) = 6 \qquad\qquad C(2) = 5$$

Figure 4.11: The example of temporal correlation function. Digit 1 stands in places of the illuminated pixels from the first image. Green color represents the pixels, which have been illuminated since the first frame. Red color shows the illuminated pixels which have not been illuminated in the first frame. Yellow color indicates the pixels, which were illuminated in the first frame, but were not illuminated in at least one frame preceding current frame. The sum of green, red and yellow indicators is always the same, meaning there is always the same number of the illuminated pixels.

$$P(\delta t | \tau) = \begin{cases} \frac{\tau - \delta t}{\tau}, & \text{if } t < \tau \\ 0, & \text{if } t > \tau \end{cases} \tag{4.9}$$
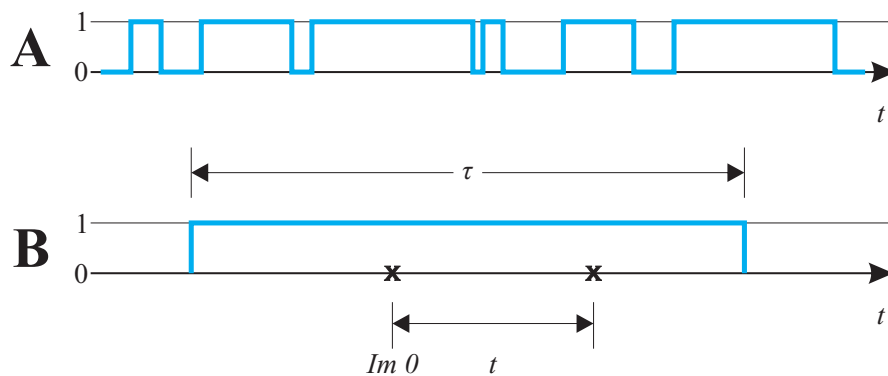

Figure 4.12: (**A**)The example of pixel's state changes. 0 and 1 indicate pixel's switched-off and illuminated states. (**B**) The example of a choice of *Im 0* that leads to an illuminated pixel at time δt. (**C**) The example of a choice of *Im 0* that leads to a switched-off pixel at time δt. If *Im 0* is placed in the red region, the pixel will be switched-off before time δt passes.

Consequently:

$$C(t) = \int_t^\infty \rho(\tau)\frac{\tau - t}{\tau}d\tau \tag{4.10}$$

In particular, for pixels having a unique lifetime τ_0:

$$\rho(\tau) = \delta\left(\tau - \tau_0\right) \tag{4.11}$$

then (see Figure 4.13):

$$C(t) = \frac{\tau_0 - t}{\tau_0} \tag{4.12}$$
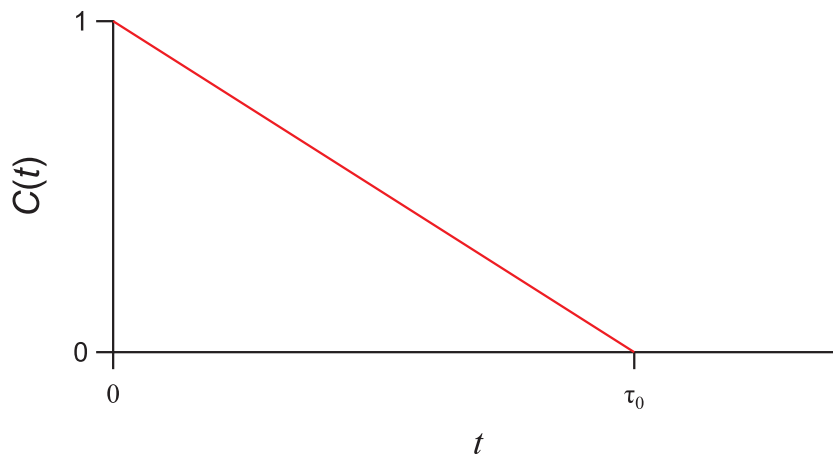

Figure 4.13: The lifetime of the pixels.

As a consequence, the slope of $C(t)$ is $-\frac{1}{\tau_0}$, the lifetime of the pixels and our correlation function thus provides a direct measurement of the pixel lifetime.

4.7   Data/light collection

Now we wish to compute the average number of pixels illuminated by a fixed particle which size ranges from 20 to 100 nm.
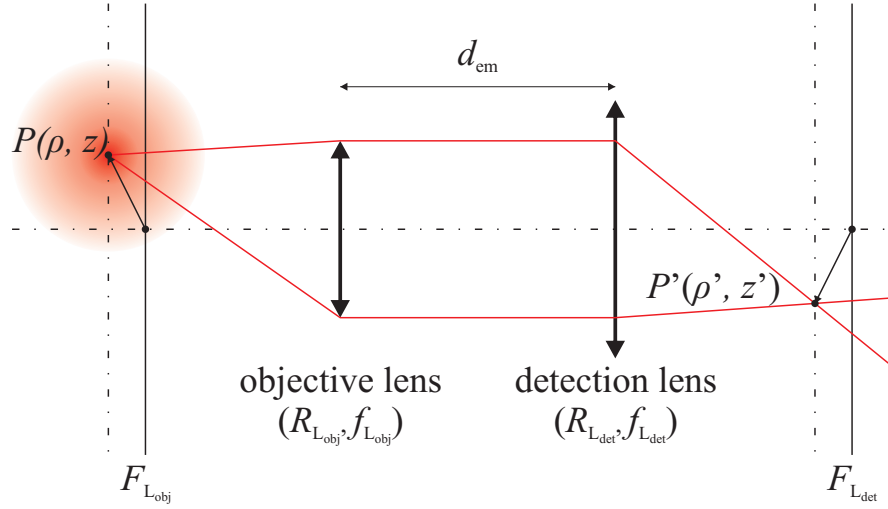
Figure 4.14: An example of path detection in the confocal microscope. The label P of the sample region emits a fluorescent light which is collected by the objective lens and imaged by the detection lens.[85]

A monochromatic point source is located at the point $P = (\overrightarrow{\rho}, z)$, which may be at the focal point of the objective. The geometrical image of the point P for the system of two lenses (the objective and the detection ones) is labeled $P' = (\overrightarrow{\rho'}, z')$ and the source's wavelength is λ_{em}. ρ and ρ' are the distances of points P and P' from the optical axis. z is the distance from P to the focal plane of the objective and z' is the distance from P' to the focal plane of the detection lens (see Figure 4.14). The position of the image of P in the detection area depends on the magnification of the lenses $\alpha = f_{\text{L}_{\text{det}}} / f_{\text{L}_{\text{obj}}}$ and the distance d_{em} between two lenses. In our case when $d_{\text{em}} = f_{\text{L}_{\text{det}}} + f_{\text{L}_{\text{obj}}}$, the coordinates of P' in the detector are as follows:

$$\overrightarrow{\rho'} = -\alpha \overrightarrow{\rho} \tag{4.13}$$

$$z' = -\alpha^2 z \tag{4.14}$$

Let us now consider a source of fluorescence of unitary intensity placed in point $P = F_{\text{L}_{\text{obj}}}$. Due to the diffraction of light by the diaphragms of the objective and the detection lenses, the intensity will be distributed around $P' = F_{\text{L}_{\text{det}}}$. Let us call M a point in the detection space, whose cylindrical coordinates are:

$$\vec{\rho_{\mathrm{D}}} = \overrightarrow{HM} \tag{4.15}$$

$$z_{\mathrm{D}} = F_{\mathrm{L_{det}}} H \tag{4.16}$$

where H is the orthogonal projection of M at the optical axis and $F_{\mathrm{L_{det}}}$ is the focal point of the detection lens.

Then, the intensity at M due to the unitary point source located at P is given by:

$$I_{\mathrm{em}}^0(M) = 4\pi^2 \mathrm{NA_{em}}^4 \left| \Psi\left(\vec{v_{\mathrm{D}}}, u_{\mathrm{D}}\right) \right|^2 \tag{4.17}$$

where Ψ is point spread function of the system of two lenses given by the formula:

$$\Psi\left(\vec{v}, u\right) = \int_0^1 \exp\left(\frac{iur^2}{2}\right) J_0(vr) r \, dr \tag{4.18}$$

$$\tag{4.19}$$

where J_0 is the zeroth order Bessel function.

u_{D} and $\vec{v_{\mathrm{D}}}$ are the optical coordinates of M in the detection space:

$$\vec{v_{\mathrm{D}}} \approx \frac{2\pi}{\lambda_{\mathrm{em}}} \vec{\rho_{\mathrm{D}}} \tag{4.20}$$

$$u_{\mathrm{D}} \approx \frac{2\pi \mathrm{NA_{em}}^2}{\lambda_{\mathrm{em}}} z_{\mathrm{D}} \tag{4.21}$$

with:

$$\mathrm{NA_{em}} = \frac{\min\left[R_{\mathrm{L_{obj}}}, R_{\mathrm{L_{det}}}\right]}{f_{\mathrm{L_{det}}}} \tag{4.22}$$

In particular case, if M is located in the focal detection plane, $z_{\mathrm{D}} = 0$ and:

$$\Psi\left(\overrightarrow{v_{\mathrm{D}}}, 0\right) = 4 \operatorname{sinc}\frac{v_{\mathrm{D}}}{4} \tag{4.23}$$

Experimentally, signal-to-noise ration (SNR) is around 3/2, which means that 2/3 of the intensity emitted by our point in the sample cannot be distinguished from the noise. This value of the intensity corresponds to $v_{\mathrm{D}}/4 = 1.08$ and $\rho_{\mathrm{D}} \approx 8.8$ µm.

Diameters of the images of the 20 nm, 40 nm, and 100 nm diameter particles are approximately 18.8 µm, 20.0 µm and 22.6 µm, respectively.

Chapter 5

Results and discussion

5.1 Results

5.1.1 Introduction

Acquisition of films

The experiment were performed with 3 bead sizes (20, 40, and 100 nm diameter) simultaneously. One batch of Laponite solution was prepared and three samples with different bead sizes were created. It was very important that the physical conditions are identical for each sample. The detailed sample preparation is described in [59].

Figure 5.1 contains exact timing details of the experiment. The first measurement started with 20 nm beads, then was followed by 40 nm and 100 nm measurements. Each measurement, called later on a film, was saved as a set of images, called also the frames, with a frequency $f = 4$ Hz. The films 1–8 last 300 s, while the following (up to 24) last 900 s, which gives 1200 and 3600 frames, respectively. The intervals between consecutive measurements are not equal because of the need to change the samples manually on the microscope.

The experimental setup is the one described in Section 4.4. As mentioned above the frames were saved every 250 ms. The integration time for each frame was also 250 ms, meaning that the signal was gathered and summed up for this time. It helped increasing the signal to noise ratio and made the fluorescent objects better visible.

The overall experiment time is 59565 s. 24 films were acquired for each bead diameter, and were subsequently analyzed.
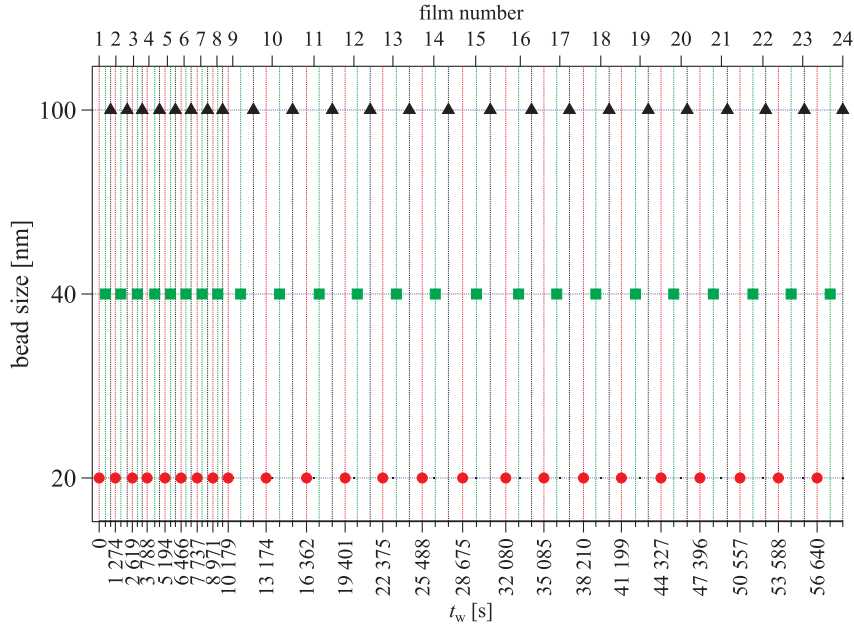

Figure 5.1: The experiment course. The markers indicate the beginning of each measurement, which lasted 300 s for films 1–8 or 900 s for films 9–24, for all the bead sizes. The bottom and the top axes are the waiting time t_{w} and film number for 20 nm diameter beads, respectively. The left axis shows the bead size (proportion not preserved).

Computation of the correlation function

For each film, a series of reference images, ranging from 125 to 224 s after the beginning of the film, was chosen. For each of these reference images, a correlation function is computed (with 50 most intense pixels of the reference image) with the following 300 images, corresponding to a measurement delay time equal to 75 s. Curves from film 18 are shown in Figure 5.2.

Every correlation curve consists of a succession of plateaus, separated by a decrease of 1/50. Each decrease of the correlation function corresponds to the loss of 1 pixel. Mostly we do not see two pixels disappearing simultaneously. For the smallest particles, the correlation functions reach zero at $t = 75$ s, whereas for 40 nm and 100 nm diameter particles a total decorrelation is not reached.

If we consider a set of correlation curves computed during one of these fits (that is

during a time interval of 175 s), strong fluctuations can be observed. We thus decided to average these curves over one film duration (thick curves in Figure 5.2).

The evolution of the averaged curves is given in Figure 5.3. At the very beginning of the experiment, all of the curves decorrelate completely in 75 s, whatever the size of the particle. Then, a different behavior is observed: the dynamics slows down. This leads to an incomplete decrease of the correlation.

More precisely, two relaxation modes are observed:

* ⋆ fast mode, up to a few seconds, that decorrelates the signal partly,

* ⋆ slow mode, of characteristic time ≈ 70 s or larger, whose amplitude depends on the size of the particles.
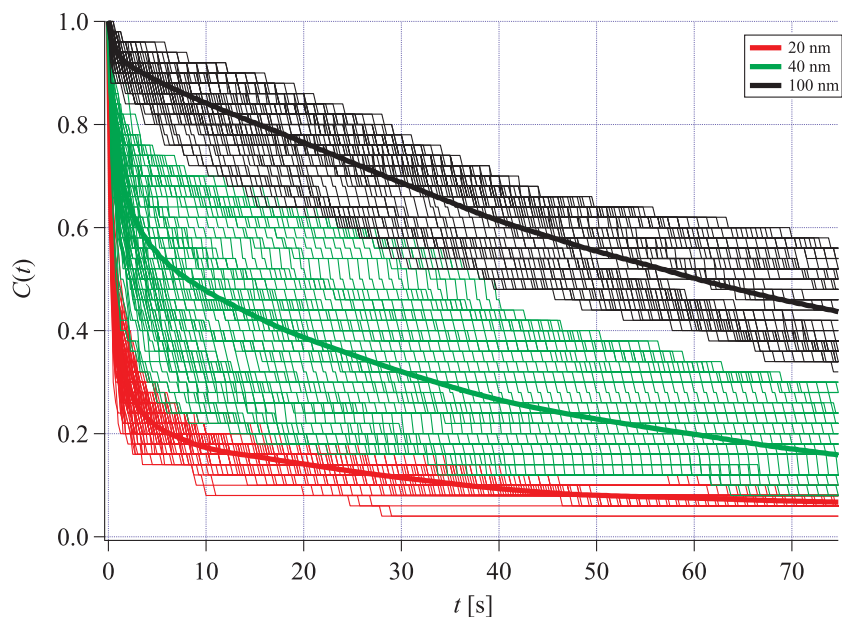

Figure 5.2: Raw (thin lines) and averaged (thick lines) correlation curves for 20, 40, and 100 nm diameter beads. The data for reference images 501–897 (every fourth) of film 18.

5.1.2 Fast relaxation mode

For a system that would exhibit a unique relaxation time τ, $C(t)$ would decrease linearly with time if a unique pixel lifetime exists.
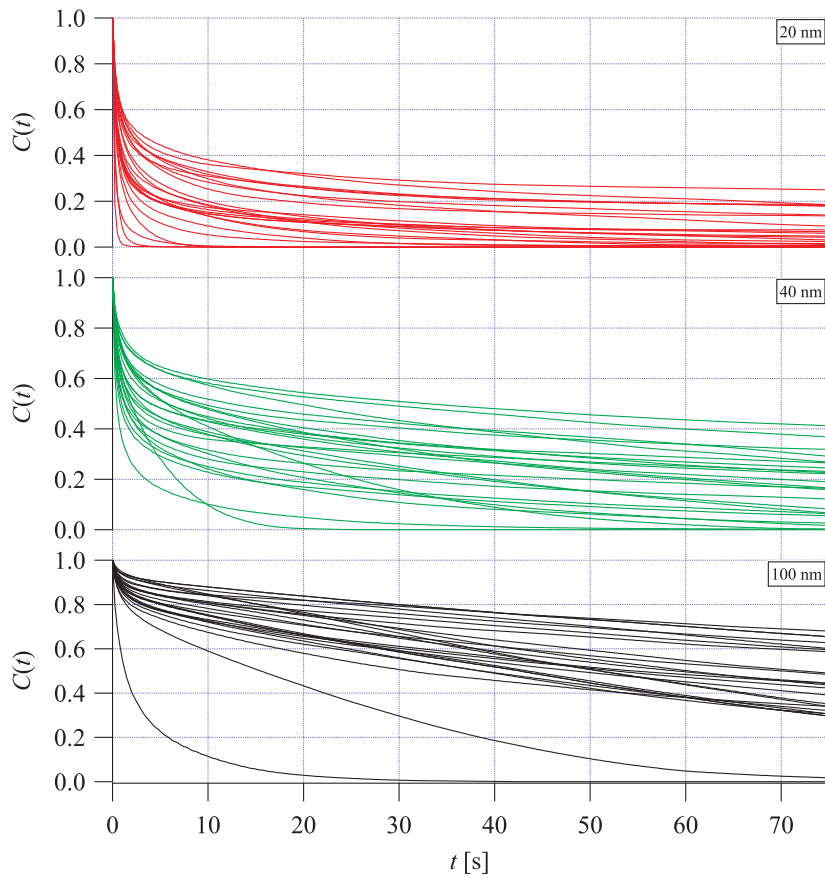
Figure 5.3: Averaged correlation curves for 20, 40, and 100 nm diameter beads. Each curve represents an average of 100 raw correlation curves. The data for reference images 501–897 of film 18.

In that case, we have (see Equation 4.12):

$$C(t) = 1 - \frac{t}{\tau} \tag{5.1}$$

But we observe that $C(t)$ exhibits a curvature at short time (see Figure 5.3):

$$\frac{\partial^2 C}{\partial t^2}\bigg|_{t \to 0} \neq 0 \tag{5.2}$$

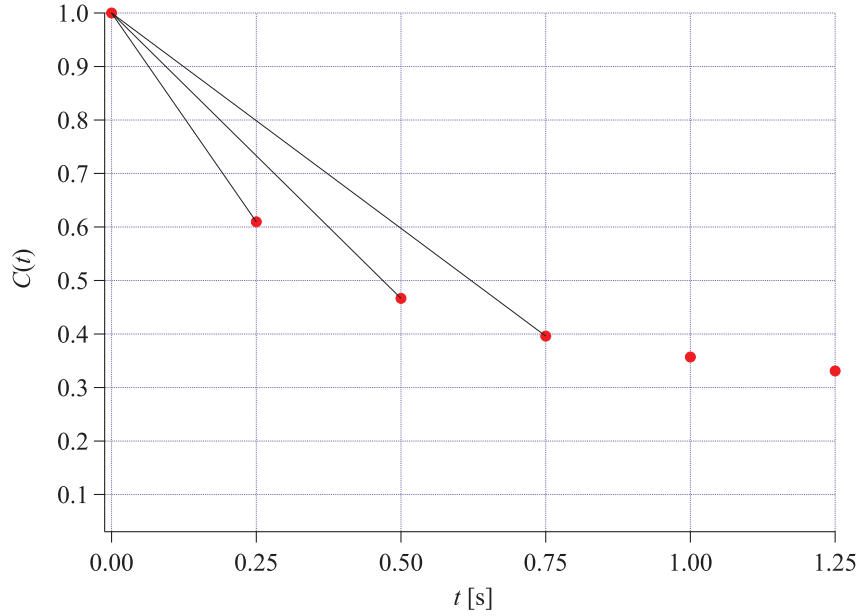We are interested in the limiting behavior of $C(t)$ when $t \to 0$. Let us assume that

Figure 5.4: The graphical explanation of calculating the apparent decay time $\tau_{\text{fast}_{\text{apparent}}}$. The lines represent the slopes between $C(0)$ and $C(t_{\text{n}})$ ($n \in [1,3]$).

when $t \to 0$, $C(t)$ may be expanded as $C(t) = 1 - t/\tau + \alpha t^2 + o(t^2)$.

Then the apparent slope of the correlation decrease between time 0 and time t writes as $s(t) = \frac{C(t) - C(0)}{t}$, so $\frac{1}{\tau}$ may be evaluated as $\lim_{t \to 0} s(t)$ (see Figure 5.6).

We will determine τ by taking the limit of $s(t)$ when $t \to 0$. We chose to take first 3 points after time 0 into consideration, as demonstrated in Figure 5.4. For any of these points $t_{\text{n}} (n \in [1,3])$ values of $s(t_{\text{n}}) = -\frac{1}{\tau} + \alpha t_{\text{n}}$. Then, to determine the apparent decay time associated with the first three points we calculate $\tau_{\text{fast}_{\text{apparent}}}$ as:

$$\tau_{\text{fast}_{\text{apparent}}}(n) = \left(\frac{1 - C(t_{\text{n}})}{n \delta \tau} \right)^{-1} \tag{5.3}$$

where n is the point number ($n \in [1,3]$) and $\delta \tau$ is the time between two successive images.

Figure 5.5 is the series of the values calculated with the above equation for 20 nm particles as a function of t. The calculations were performed identically for all the particle sizes and all the waiting times t_{w}. We observe that the $\tau_{\text{fast}_{\text{apparent}}}$ increases
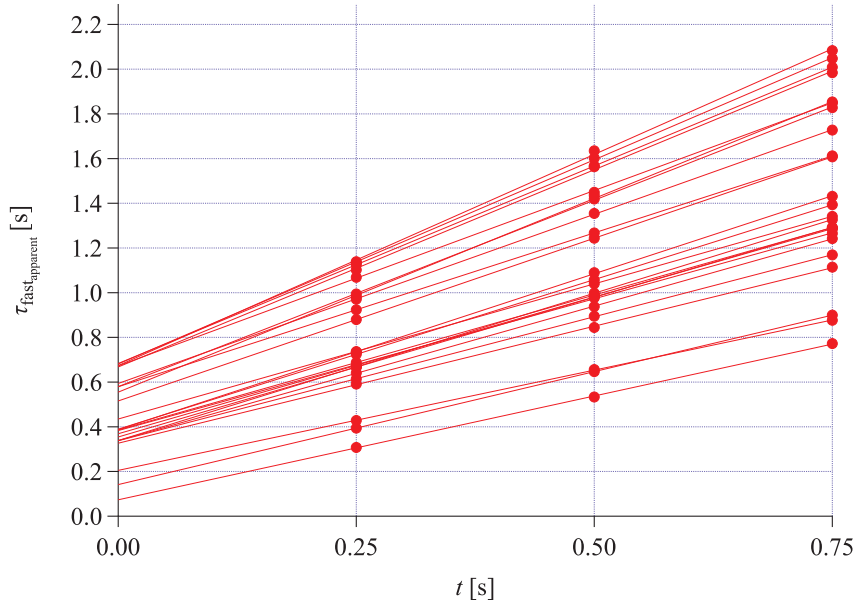
Figure 5.5: The apparent decay time $\tau_{\mathrm{fast_{apparent}}}$ curves for all 24 films of 20 nm beads. The lines are linear fits of 3-point sets. The intercepts with Y-axis are τ_{fast} values.

with n, meaning that the correlation function exhibits an upward curvature. As we are interested in the short time dynamics of the system we then fit these 3 points with line whose intercept with y-axis is τ_{fast}. Results are given in Figure 5.6.

τ_{fast} is proportional to the inverse of the radius (see Figure 5.7).

For $t_{\mathrm{w}} > 5000$ s, τ_{fast} is constant for each size, but exhibits a considerable noise—standard deviation is 29.8%, 37.1% and 33.0% of the average value for 20, 40, and 100 nm beads, respectively. At short waiting times ($t_{\mathrm{w}} < 5000$ s) an increase of τ_{fast} is observed for 20 and 100 nm diameter particles. This increase is small and difficult to study precisely due to the noise of the data and cannot be observed for 40 nm diameter particles. It may be due to the increase of the viscosity of the suspension over this time lapse.

We will now consider only the long waiting time behavior ($t_{\mathrm{w}} > 5000$ s). In this regime τ_{fast} does not depend on t_{w}. The average of $\tau_{\mathrm{fast}}(t_{\mathrm{w}})$ and its standard deviation for each bead size is given in Figure 5.7. We observe that τ_{fast} increases according to an affine relationship with the bead size.
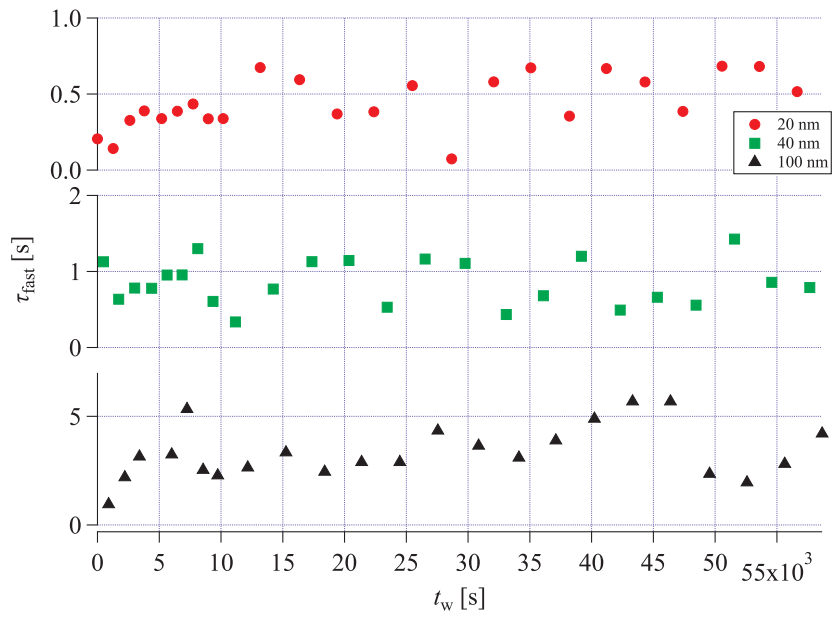
Figure 5.6: τ_{fast} values for 20, 40, and 100 nm diameter beads as a function of the waiting time t_{w}.
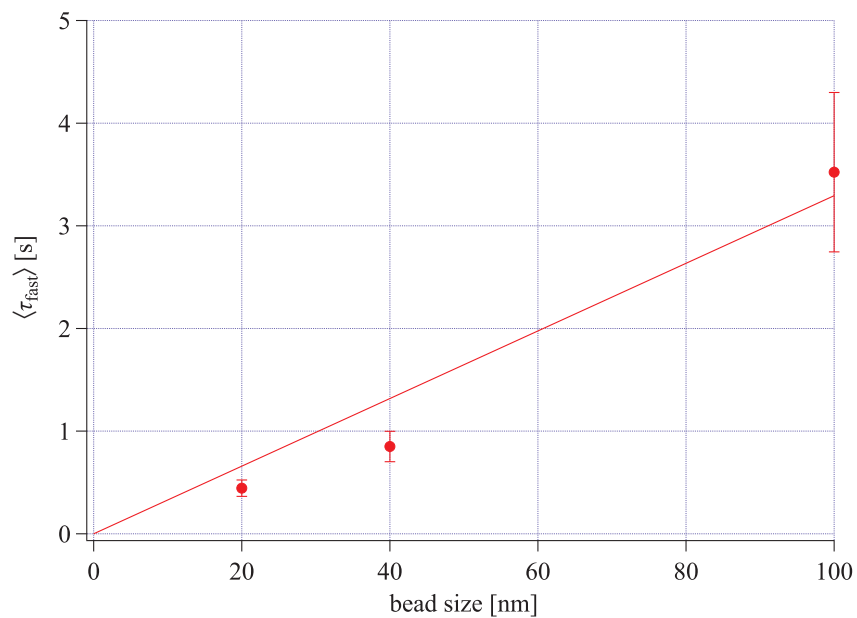

Figure 5.7: The values of τ_{fast} averaged over the last 20 films as a function of bead diameter. The line is the linear fit going through the origin. Error bars being 2 standard deviations.

5.1.3 Slow relaxation mode

Let us now consider the slow relaxation mode of the correlation. At long times, $C(t)$ may well be described by a linear decrease (see Figure 5.8) and we once again assume that the dynamics may be described by single relaxation mode, whose characteristic time is τ_{slow}.
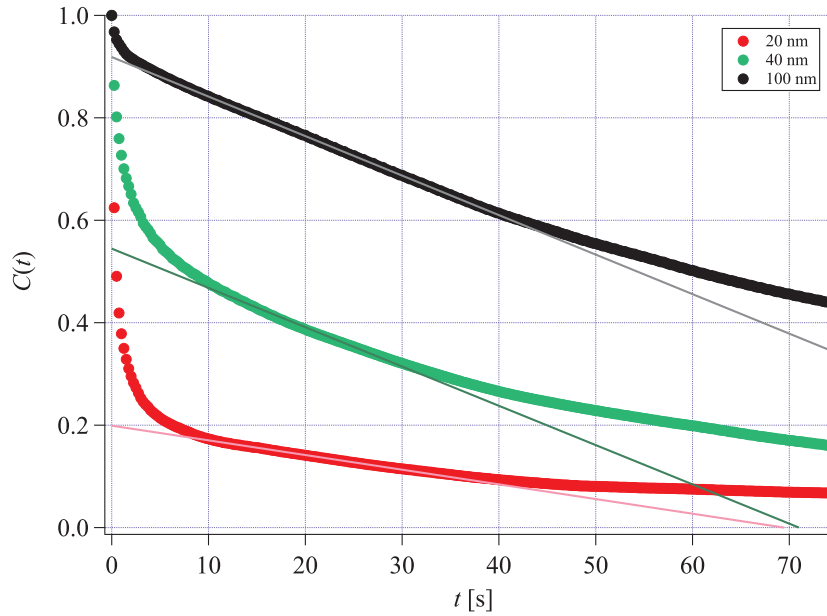

Figure 5.8: The correlation curves for 20, 40, and 100 nm diameter beads. The data for reference images 501–897 (every fourth) of film 18. The lines represent the linear fits for points in the range 10 s $< t <$ 30 s. The intercepts with Y-axis are α_{c} values.

We thus fit the correlation curve with a line for 10 s $< t <$ 30 s:

$$f(t) = \alpha_{\text{c}} \left(1 - \frac{t}{\tau_{\text{slow}}} \right) \tag{5.4}$$

from which we obtain the amplitude of the slow relaxation mode, α_{c}, and its characteristic time τ_{slow}.

For 20 nm beads at short waiting times ($t_{\text{w}} < 3000$ s), the decorrelation is total at long times and $C(t) = 0$ for $t > 10$ s. For 20 nm τ_{slow} is constant with time, whereas for 40 nm and 100 nm we see the increase of the factor of 2 of the slow decay time. τ_{slow} for
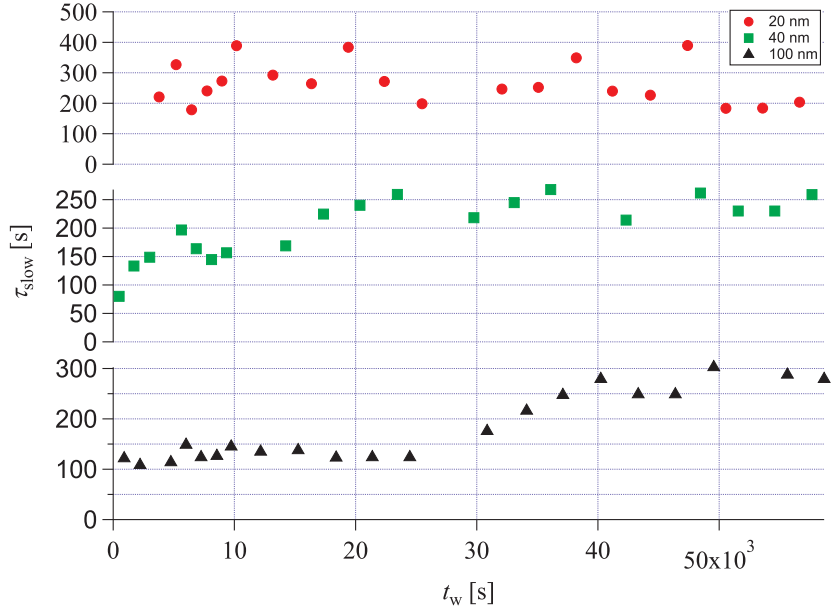
all the data set is given in Figure 5.9.

Figure 5.9: τ_{slow} values for 20, 40, and 100 nm diameter beads as a function of the waiting time t_{w}.

The long decay time of the 20 nm probes is very noisy, and any evolution with time cannot be detected. As for the 40 nm and 100 nm probe particles, their dynamics slows down between the initial time and the end of the experiment.

On the contrary the amplitude of the slow motion, α_{c}, depends strongly on the particle radius. It increases with the increasing diameter of the beads (see Figure 5.10). For $t_{\text{w}} > 5000$ s it does not depend on t_{w}. The average of α_{c} over t_{w} is shown in Figure 5.11.

5.2   Discussion

In the following section we will derive physical quantities from the measured dynamics of the beads. We will distinguish two modes of relaxation—at short distances, the particles exhibit fast motion, whereas over longer scales, a slower motion is observed. We will assume that in the fast regime the motion may be described as a Brownian displacement and will define the corresponding diffusion coefficient, D_{fast}.

We will also determine cross-over spatial scale between the two relaxation modes,
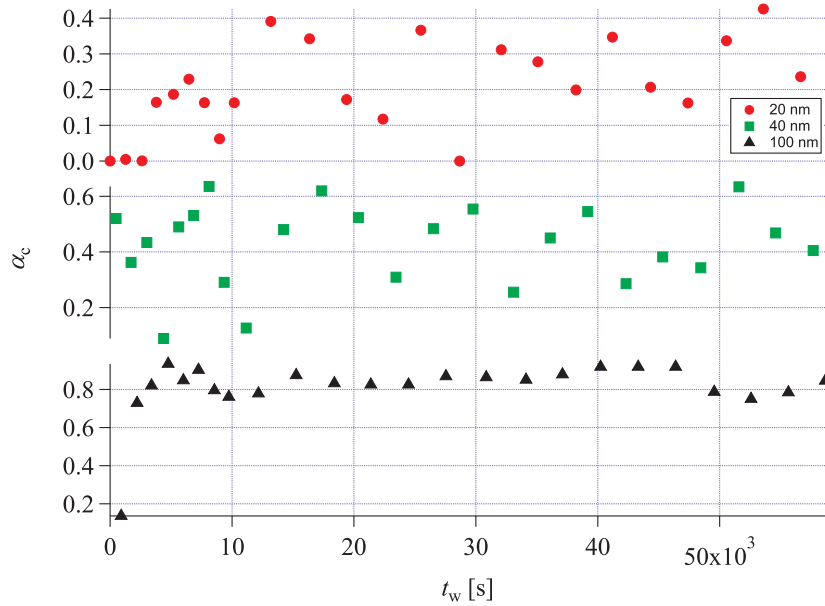
Figure 5.10: α_c values as a function of waiting time t_w. The α_c values are the values of the intercepts with Y-axis of the correlation fits, as shown in Figure 5.8.
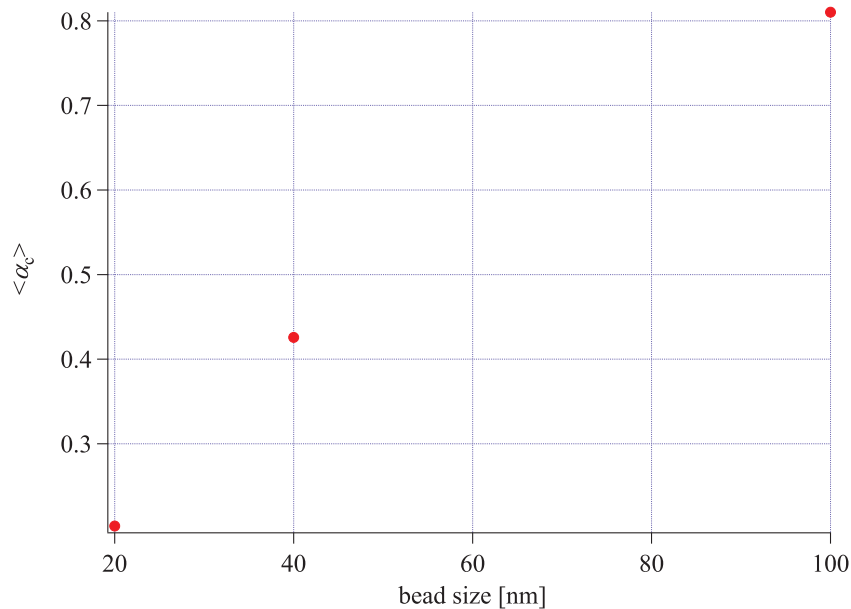

Figure 5.11: The average values of α_c for 20, 40, and 100 nm diameter beads. The line is the linear fit. Error bars being 2 standard deviations.

that we will call it a "cage" size.

5.2.1 Calculating diffusion coefficients and cage size

Derivation of the diffusion coefficients from the slope of $C(t)$

In the fast regime:

$$C(t) = \alpha \left(1 - \frac{t}{\tau_{\text{fast}}} \right) \tag{5.5}$$

where τ is the time needed for all pixels illuminated in the reference image to switch off (change state from 1 to 0) due to the motion of the beads. In other words, τ_{fast}, is the time for an illuminated spot onto the CCD camera to move by a distance of the order of its diameter[1]. We then have:

$$\delta_\tau^{\text{CCD}} = \sqrt{\tilde{\alpha}} d_{\text{p}} \tag{5.6}$$

where δ_τ^{CCD} is the displacement of a spot observed on the CCD plane in time τ_{fast} and $\sqrt{\tilde{\alpha}} d_{\text{p}}$ is the mean size of the spot. This corresponds to a bead displacement inside the sample, $\delta_\tau^{\text{sample}}$:

$$\delta_\tau^{\text{sample}} = \frac{1}{60} \sqrt{\tilde{\alpha}} d_{\text{p}} \tag{5.7}$$

This corresponds to a diffusion coefficient given by:

$$D_{\text{fast}} = \frac{(\delta_\tau^{\text{sample}})^2}{\tau} = \left(\frac{1}{60} \right)^2 \cdot \tilde{\alpha} A_{\text{p}} \frac{1}{\tau_{\text{fast}}} \tag{5.8}$$

---

[1]Let us insist on the fact that, due to the diffraction (see Section 4.7), this time is much longer than the time needed for a particle to move by its radius.

Derivation of the cage radius

When we observe pixels still illuminated after time t, this means that they have always been equal to 1 between time 0 and t. As a consequence, the spot associated to these pixels does not have moved enough to make them disappear. Let us assume that the spot is circular (see Figure 5.12) and that it is confined in a circular cage. Then we have:

$$R_{\text{cage}} = R_{\text{spot}} - R_1 \tag{5.9}$$

Consequently:

$$D_{\text{cage}} = 2R_{\text{cage}} = 2\left(R_{\text{spot}} - R_1\right) = 2R_{\text{spot}}\left(1 - \frac{R_1}{R_{\text{spot}}}\right) \tag{5.10}$$

The measurement of α_{c} gives us the fraction of pixels that remain equal to 1 and we have:

$$\alpha_{\text{c}} = \frac{R_1{}^2}{R_{\text{spot}}{}^2} \tag{5.11}$$

Then:

$$R_{cage}^{\text{CCD}} = \sqrt{\tilde{\alpha}}d_{\text{p}}\left(1 - \sqrt{\alpha_{\text{c}}}\right) \tag{5.12}$$

This corresponds to the amplitude of the displacement of the beads inside the sample equal to:

$$R_{cage}^{\text{sample}} = \frac{1}{60}\sqrt{\tilde{\alpha}}d_{\text{p}}\left(1 - \sqrt{\alpha_{\text{c}}}\right) \tag{5.13}$$
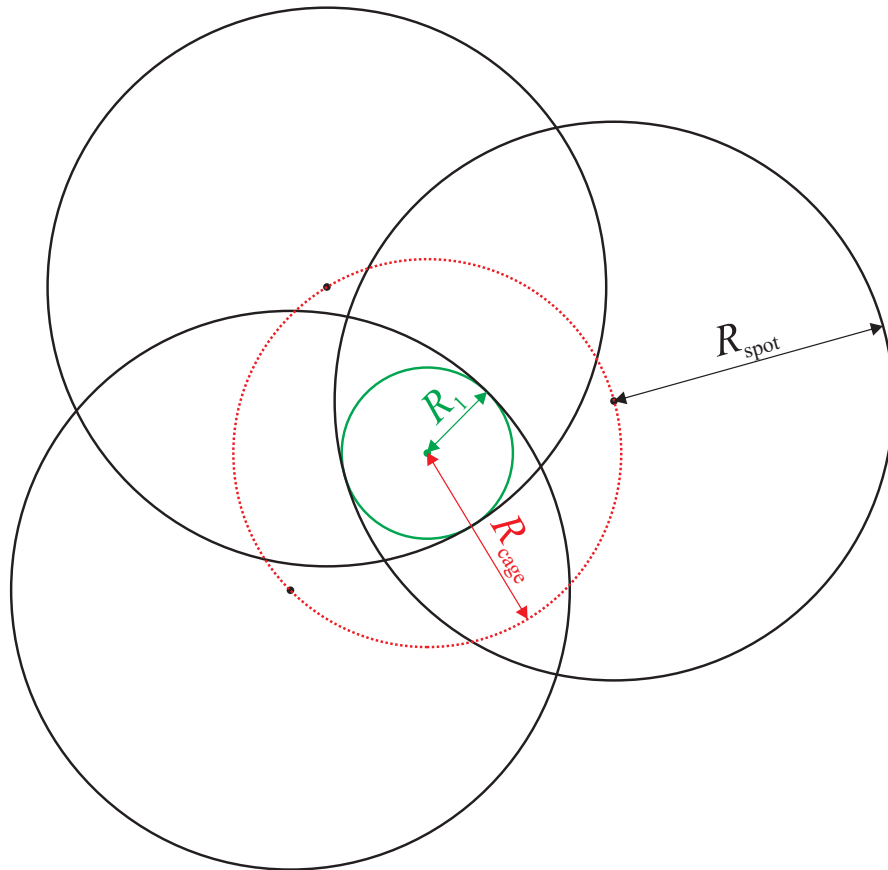
Figure 5.12: The graphical example of possible spot's positions and the common area. The black circles are demonstration of spot's position; the green circle is the common area of all the spots, which remains illuminated during the measurement; the dotted red circle is the cage. R_1 is the radius of the zone of pixels still being illuminated at long time t, R_{spot} is the radius of the spot, R_{cage} is the maximum displacement of the spot's center.

5.2.2 Discussion of the results

Fast relaxation mode

We observe that, for $t > 5000$ s, D_{fast} does not depend on t_w, but decreases with the particle radius (see Figure 5.13).

Slow relaxation mode

R_{cage} decreases while bead size increases.
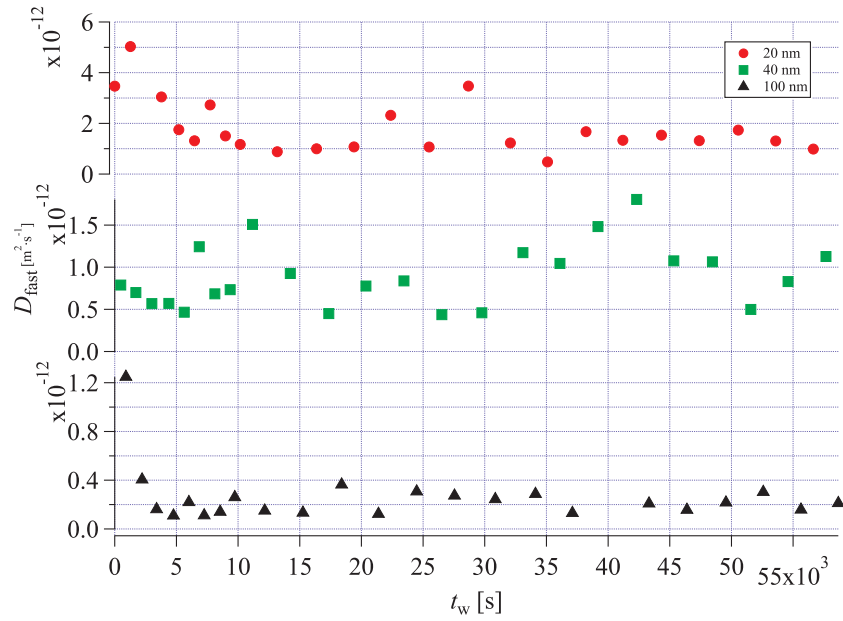
Figure 5.13: The diffusion coefficient D_{fast} as a function of waiting time t_{w}.
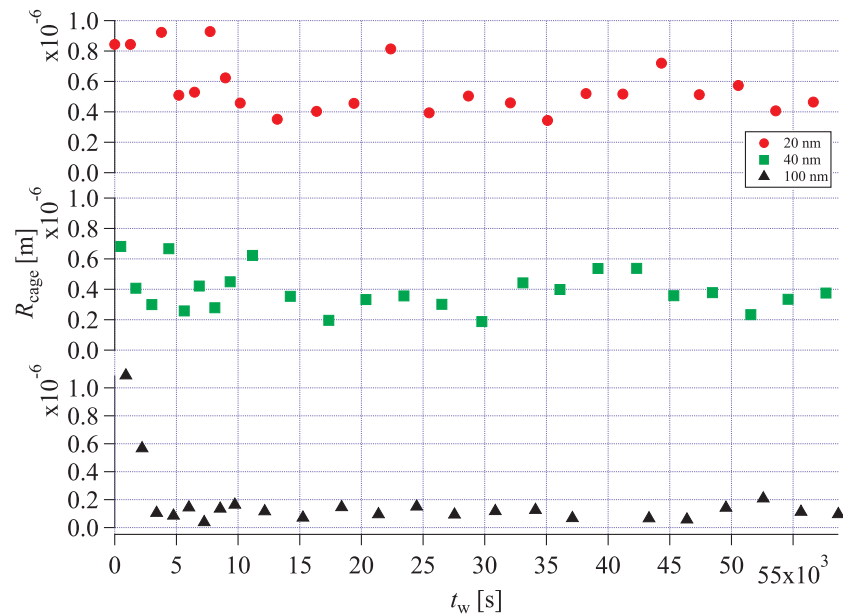

Figure 5.14: The cage radius R_{cage} as a function of waiting time t_{w}.

The displacement of 500 nm beads has been studied in [59] for which the cage radius $R_{\text{cage}} = 5 \cdot 10^{-9}$ m was obtained.

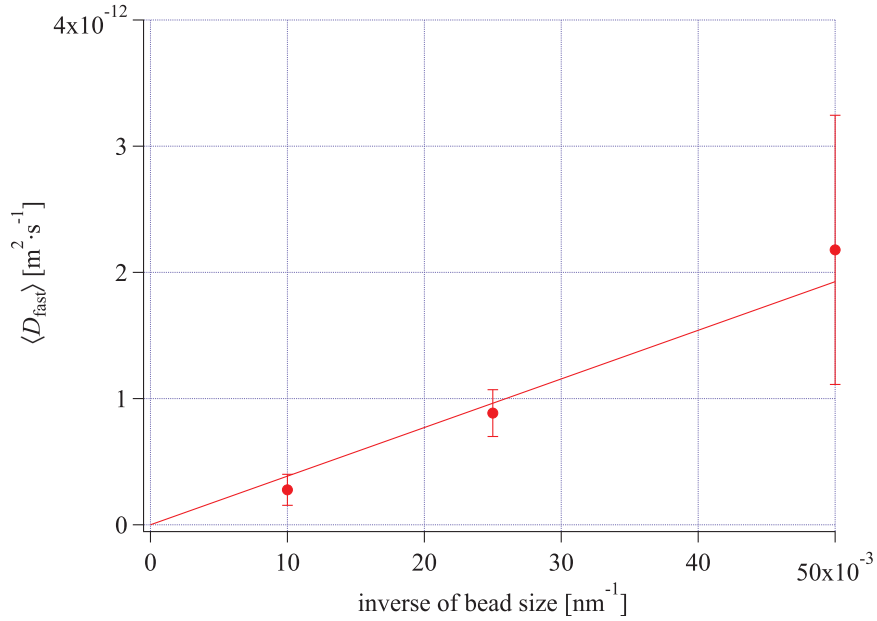Would the system be an elastic solid, we would have: [57]

Figure 5.15: The mean diffusion coefficient $\langle D_{\text{fast}} \rangle$ as a function of inverse of bead size.

$$R_{\text{cage}}{}^2 = \frac{k_{\text{B}}T}{6\pi G'R} \tag{5.14}$$

where G' is the elastic modulus. We do not obtain this scaling law, but observe that R_{cage} increases faster than $\frac{1}{\sqrt{R}}$. This means that the apparent elastic modulus experienced by small particles is softer than the one experienced by larger particles.

We have shown that the mechanical properties of the Laponite suspension and their aging with time depend on the probe particle used. The apparent elastic modulus of the Laponite suspension decreases when the particle's diameter decreases.

For 20 nm particles (that is for the particles smaller than the Laponite disks' diameter) we do not observe the aging, which we do for 40 nm and 100 nm particles.

Whatever their size, the dynamics of the probe particles is characterized by a rapid motion that does not evolve with the age of the sample. The characteristic decay time corresponding to this mode is inversely proportional to the radius of the particles. The amplitude of this rapid motion strongly depends on the diameter of the probe particles. From this amplitude, one can compute the apparent elastic modulus, at the scale of the
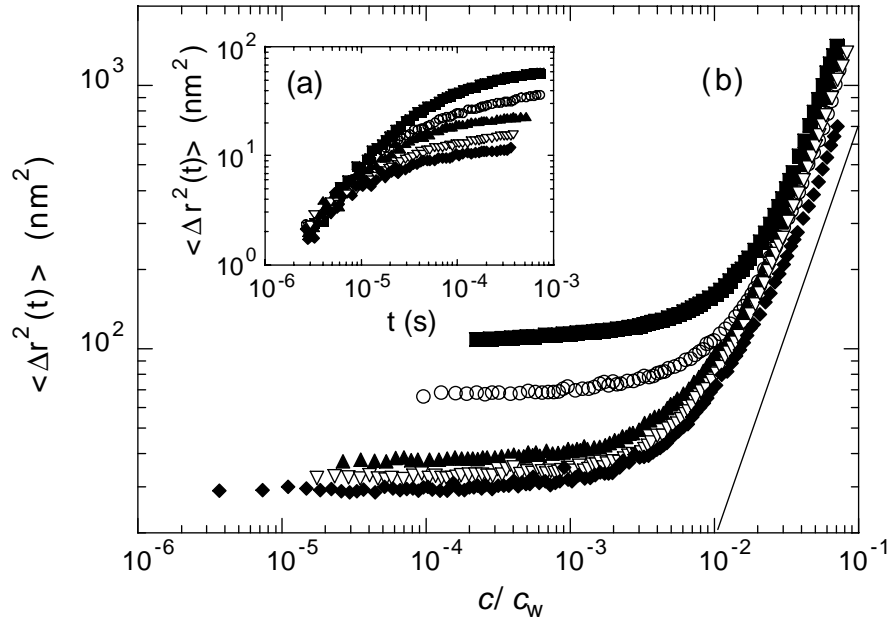
Figure 5.16: Mean-square displacement of the latex particles as a function of t/t_{w}. The late-time asymptotic regime corresponds to a scaling law with $\langle \Delta r^2(t_{\mathrm{w}}, t) \rangle = a(\phi)(t/t_{\mathrm{w}})^\gamma$, where $\gamma = 1.5 \pm 0.1$ and $a(\phi)$ is a concentration-dependent prefactor. Inset: the short-time mean-square displacements for various waiting times, showing that all $\langle \Delta r^2(t_{\mathrm{w}}, t) \rangle$ exhibit the same diffusive behavior at early times independent of sample age. The waiting times in (a) and (b) are, from top to bottom, 720 s, 1260 s, 4560 s, 6900 s and 10860 s. [59]

probe particle. The Laponite gel softens as the probe particle diameter is decreased. Then, a long time relaxation is observed. For the smallest particles, the fluctuations of the dynamics with time does not allow to measure any evolution of this relaxation mode with the aging of the system, but for the largest ones, the relaxation time appears to increase with the age of the system.

Figure 5.17: The evolution of the mean value of cage radius as a function of the bead size. The result for 500 nm is taken from [59].
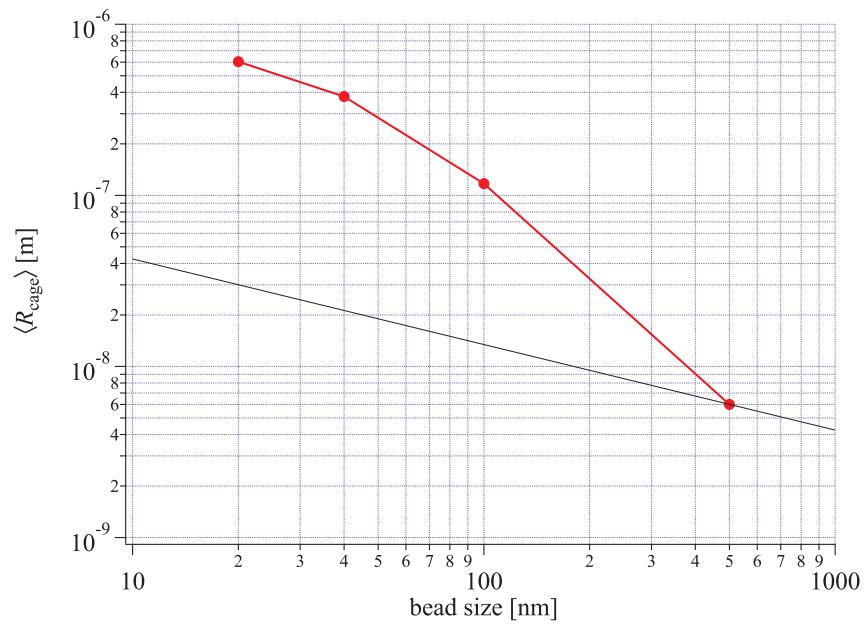
Summary

In this thesis we have studied the interaction of NCp7 protein and DNA. Our main result for the NCp7/DNA interaction is that the fraction of base pairs that have reacted, ϕ, is not a linear function of time at low ϕ. We observe instead that the rate of complexation per unit time $d\phi/dt$ has a maximum over time.

The simplest kinetic adsorption would lead to a constant rate of protein adsorption up to a level close to saturation. We interpret our results assuming that the adsorption of NCp7 on DNA is highly cooperative. We then derive the NCp7's adsorption coefficients on a sequence of base pairs surrounded by uncomplexed base pairs, k_0, and a sequence of base pairs adjacent to base pairs already complexed, k_1. We find that the ratio k_1/k_0 is of the order of 200.

We study dynamics of the probe particles of the colloidal glass suspension of Laponite. We find that, whatever their size, the motion of the probe particles can be described by a succession of two dynamic modes. The fastest mode corresponds to scattering of particles in a viscoelastic fluid. The apparent viscosity is not dependent on the diameter of the probe particle.

Instead, the apparent elastic modulus decreases as the particle diameter decreases. This shows the existence of a spatial structure, such as the elastic propagation of the constraint is more effective than the scale on which the measurement, is large.

Appendix A

Sample preparation protocols

A.1   DNA for optical trap

An EcoRI linearized pBR322 plasmid (see Figure A.1) is labeled with biotin or digoxigenin. We obtain two differently labeled types of DNA and apply to each of them a HindIII restriction. We purify this restriction product to keep only the 4.3 kb DNA. A final ligation between the two different DNA types leads us to a 50% concentration of a pBR322 dimer co-labeled with biotin and digoxigenin 8.6 kb long. This length is very suitable to single molecule measurements. Is large enough to observe all of the structural changes of dsDNA and small enough to avoid needless artefact. A first incubation with 1 μm streptavidin beads, followed by a second with an anti-digoxigenin coated coverslip results in the assembly of a molecular jokari. Initially coated with aminosilane, the coverslips are additionally treated with glutaraldehyde. It is followed by an anti-digoxigenin incubation. To prevent non-specific binding we finally use Bovine Serum Albumin. All experiments are performed at 20 °C, and the incubation of all the chemicals done in PBS1X. Once the DNA ends are attached to the surface, we perform the required buffer exchanges through a flow chamber.

A.1.1   Labeling of DNA with biotin and digoxigenin (cf. Figure A.2)

Protocols are given by the enzyme's (Fermentas) or particle's (Roche) manufacturer.

∝ Perform a restriction by EcoRI on the pBR322:

113

The graph was removed because of copyright restrictions.

Figure A.1: pBR322 cloning vector.

* 10 µl of pBR322 Vector (BioLabs)
* 2 µl of 10X FastDigest® Buffer
* 5 µl of FastDigest® EcoRI Enzyme (Fermentas)
* 3 µl of water

- incubate in 37 °C for 5 min,

- stop the enzyme activity 80 °C for 5 min,

- purify by QIAquick PCR Purification Kit (QIAGEN), receive 60 μl of DNA,

- divide into two tubes, 30 μl each.

∝ Perform labeling by biotin and digoxigenin with Klenow exo enzyme:

- ⋆ 30 μl of restricted pBR322
- ⋆ 12 μl biotin (1 tube) and digoxigenin (2 tube) (Roche Applied Science)
- ⋆ 6 μl of 10X Reaction Buffer
- ⋆ 3 μl of Klenow Fragment, exo⁻ (Fermentas)
- ⋆ 9 μl of dNTP mix:

  1 μl of C (BioLabs)
  1 μl of A (BioLabs)
  1 μl of G (BioLabs)
  97 μl of water

- incubate in 37 °C for 15 min,

- incubate in 70 °C for 20 min,

- purify each tube by QIAquick PCR Purification Kit (QIAGEN), receive 30 μl from each tube.

∝ Prepare sharp edges for ligation:

- ⋆ 30 μl of pBR322 with biotin or digoxigenin
- ⋆ 4 μl of 10X FastDigest® Buffer
- ⋆ 2 μl of FastDigest® HindIII Enzyme (Fermentas)
- ⋆ 4 μl of water

- incubate in 37 °C for 5 min,

- stop the enzyme activity in 70 °C for 10 min,

- purify each tube by QIAquick PCR Purification Kit (QIAGEN), receive 30 μl from each tube,

- mix both tubes together.

∝ Perform ligation:

- ⋆ 60 μl of pBR322 labeled by biotin and digoxigenin
- ⋆ 8 μl of 10X T4 DNA Ligase Buffer
- ⋆ 2 μl of T4 DNA Ligase Enzyme (Fermentas)

- incubate in 16 °C overnight,

- stop the enzyme activity in 70 °C for 10 min,

- purify each tube by QIAquick PCR Purification Kit (QIAGEN).
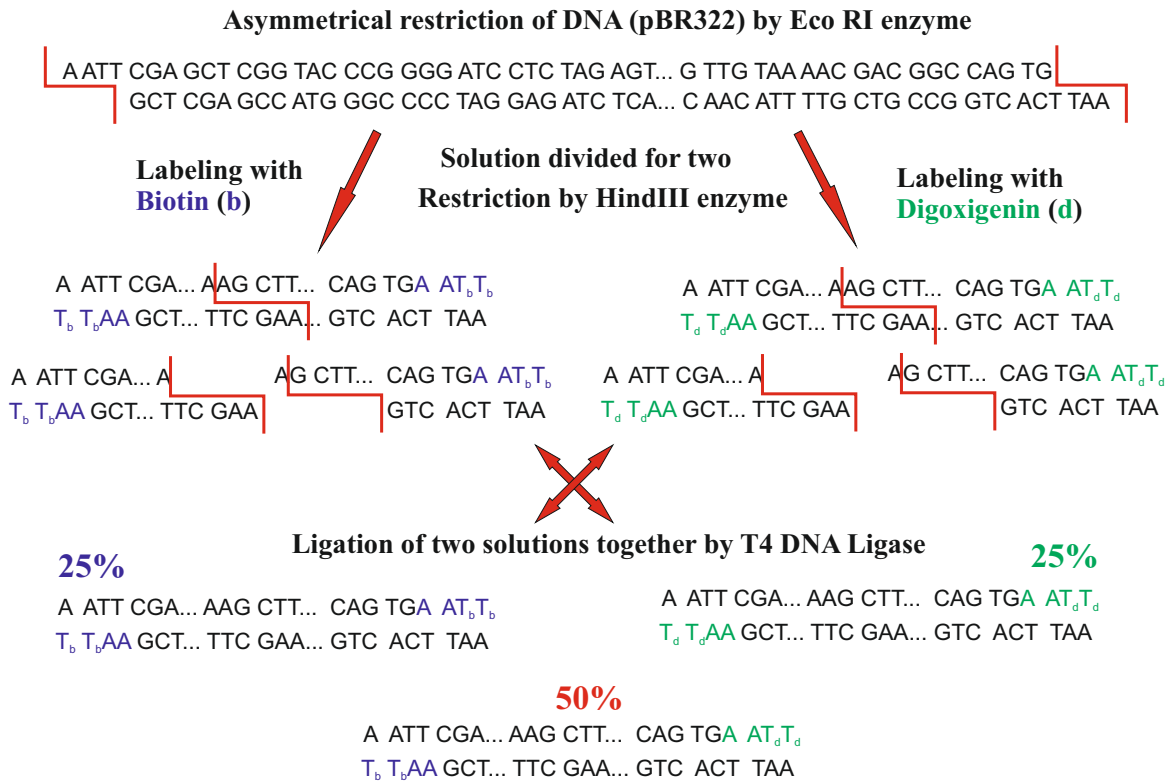
Figure A.2: Tagging DNA with biotin and digoxigenin.

A.1.2   Treatment of coverslips [35]

$\propto$ Wash the coverslips for 15 min in ultrasonic bath in the solution:

  - $\star$ 27 ml of sulfuric acid (96%)
  - $\star$ 13 ml of hydrogen peroxide—extra cleaning, charging positively the coverslip

  - wash them with water and next with ethanol,

  - dry them by nitrogen.

$\propto$ Perform the silanization by incubating the coverslips for 1 h in the following so-
   lution. This produces covalently bound amino groups on the glass surface. Glu-
   taraldehydes will covalently bind to these amino groups.:

  - $\star$ 1 ml of N-(3-trimethyloxysilylpropyl)diethyl enetriamine (Sigma-Aldrich)
  - $\star$ 45 ml of ethanol
  - $\star$ 4 ml of water

- wash coverslips in chloroform for 15 min in ultrasonic bath,

- dry them by nitrogen.

A.1.3   Attachment of DNA onto coverslips and particles (cf. Figure A.3)

- ⋆ 10 µl of DNA

- ⋆ 5 µl of streptavidin coated beads

- mix together and incubate for 2 h in the fridge.

- ⋆ 225 µl of glutaraldehyde (50% Electron Microscopy Sciences)

- ⋆ 25 µl of PBS10X

- mix together and suck into the cell by syringe,

- incubate for 30-40 min in a room temperature,

- wash by PBS1.

- ⋆ 10 µl of anti-digoxigenin (50 mg/ml, Roche)

- ⋆ 190 µl of PBS1

- mix together and suck into the cell by syringe, incubate for 1 h in a room temperature,

- wash by PBS1.

- ⋆ 2% of Bovine Serum Albumin (in solvent PBS1X)—blocks the specific binding

- suck into the cell by syringe,

- incubate for 1 h in a room temperature,

- wash by PBS1.

- ⋆ solution of DNA with beads

- ⋆ 500 µl of PBS1

- mix together and suck into the cell by syringe,

- incubate for 1 h in a room temperature (increasing the incubation time increases the number of beads anchored to the glass surface),
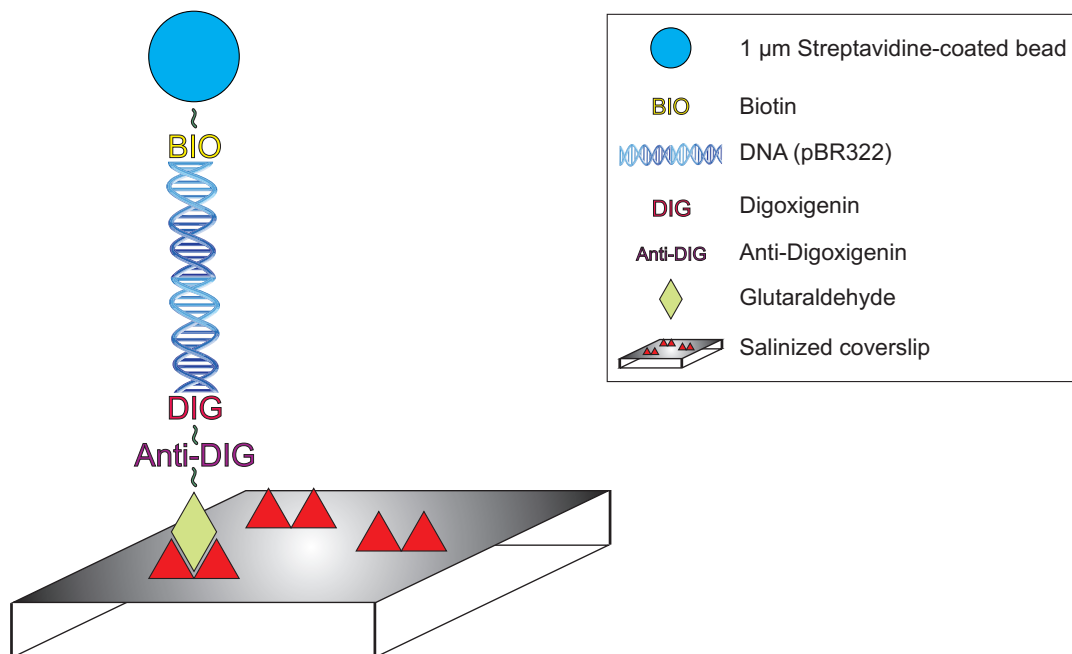
- wash by PBS1,

- wash by water.

Figure A.3: Scheme of optical trap sample.

Appendix B

The setups

B.1 Optical trap

As shown in Figure B.1 the polarized infra-red laser (Spectra Physics YAG 1064 nm) beam passes the dichroic mirror and is led to the oil immersion objective (O1, Zeiss 100/1.4). An immersion oil type FF (Electron Microscopy Sciences) is used to match the optical index of the microscope cover slips, of thickness 125 μm. This objective is mounted on a piezoelectric converter (Physics Instruments GmbH) with displacement range from 0 to 100 μm and resolution 0.2 nm. The beam is passing the sample and focused forming the optical trap. The 1m diameter solid-latex bead, bound to the one end of DNA, is held in the trap by focused laser beam which is being scattered, then collected by phase contrast objective (O2, Olympus 40/0.6) and finally detected by the photodiode (PD).

An optical fiber delivers to the setup the white light which is next collimated with the objective O3 (x10, NA 0.3). The sample is visualized by two CCD cameras (C1+C2; Kappa CF8/4, 740x582 pixels) with acquisition frequency 25 Hz, using a lens of 180-mm focal length. C2 is used to visualize the trapped bead, whereas the stuck bead by C1.[37]

The graph was removed because of copyright restrictions.

Figure B.1: Optical Tweezers setup. <u>Trapping path</u>: Laser Millenia YAG 1064nm, L1L2 telescope, DM dichroic mirror, O1 objective1 (100X NA 1.3), O2 objective2 (60X NA 0,6), L4 imaging lens, PD position diode. <u>Imaging path</u>: WL white light, O3 objective3(20X NA 0,3), CM cold mirror, C. CCD camera. <u>Signal Acquisition</u>: FG frame grabber, AB acquisition board(NI6135), PC personal computer.

Bibliography

NCp7

[1] B. H. Zimm, J. K. Bragg. *Theory of the Phase Transition between Helix and Random Coil in Polypeptide Chains.* Journal of Chemical Physics **1959** (31(2):526–535)
DOI:10.1063/1.1730390

[2] J. B. Keller. *Reaction Kinetics of a Long Chain Molecule.* Journal of Chemical Physics **1962** (37(11):2584–2586)
DOI:10.1063/1.1733058

[3] R. Wing, H. Drew, T. Takano, C. Broka, C. Tanaka, K. Itakura, R. Dickerson. *Crystal structure analysis of a complete turn of B-DNA.* Nature **1980** (287(5784):755–758)
DOI:10.1038/287755a0

[4] H. M. Berman, P. R. Young. *The Interaction of Intercalating Drugs with Nucleic Acids.* Annual Review of Biophysics and Bioengineering **1981** (10:87–114)
DOI:10.1146/annurev.bb.10.060181.000511

[5] S. B. Smith, L. Finzi, C. Bustamante. *Direct mechanical measurements of the elasticity of single DNA molecules by using magnetic beads.* Science **1992** (258(5085):1122–1126)
DOI:10.1126/science.1439819

[6] R. Schleif. *DNA Looping.* Annual Review of Biochemistry **1992** (61:199–223)
DOI:10.1146/annurev.bi.61.070192.001215

[7] M. Lapadat-Tapolsky, H. De Rocquigny, D. Van Gent, B. Roques, R. Plasterk, J.-L. Darlix. *Interactions between HIV-1 nucleocapsid protein and viral DNA may have

important functions in the viral life cycle. Nucleic Acids Research **1993** (21(4):831–839)

DOI:10.1093/nar/21.4.831

[8] C. Bustamante, J. F. Marko, E. D. Siggia, S. Smith. *Entropic Elasticity of λ-Phage DNA.* Science **1994** (265(5178):1599–1600)
DOI:10.1126/science.8079175

[9] J. F. Marko, E. D. Siggia. *Stretching DNA.* Macromolecules **1995** (28(26):8759–8770)
DOI:10.1021/ma00130a008

[10] H. C. M. Nelson. *Structure and function of DNA-binding proteins.* Current Opinion in Genetics & Development **1995** (5(2):180–189)
DOI:10.1016/0959-437X(95)80006-9

[11] P. Cluzel, A. Lebrun, C. Heller, R. Lavery, J.-L. Viovy, D. Chatenay, F. Caron. *DNA: An Extensible Molecule.* Science **1996** (271(5250):792–794)
DOI:10.1126/science.271.5250.792

[12] S. B. Smith, Y. Cui, C. Bustamante. *Overstretching B-DNA: The Elastic Response of Individual Double-Stranded and Single-Stranded DNA Molecules.* Science **1996** (271(5250):795–799)
DOI:10.1126/science.271.5250.795

[13] C. Baumann, S. B. Smith, V. A. Bloomfield, C. Bustamante. *Ionic Effects on the Elasticity of Single DNA Molecules.* PNAS **1997** (94(12):6185–6190)

[14] I. Rouzina, V. A. Bloomfield. *DNA Bending by Small, Mobile Multivalent Cations.* Biophysical Journal **1998** (74(6):3152–3164)
DOI:10.1016/S0006-3495(98)78021-X

[15] J. Rudnick, R. Bruinsma. *DNA-Protein Cooperative Binding through Variable-Range Elastic Coupling.* Biophysical Journal **1999** (76(4):1725–1733)
DOI:10.1016/S0006-3495(99)77334-0

[16] C. Bouchiat, M. D. Wang, J.-F. Allemand, T. Strick, S. M. Block, V. Croquette. *Estimating the Persistence Length of a Worm-Like Chain Molecule from Force-Extension Measurements.* Biophysical Journal **1999** (76(1):409–413)
DOI:10.1016/S0006-3495(99)77207-3

[17] M. Hegner, S. B. Smith, C. Bustamante. *Polymerization and mechanical properties of single RecADNA filaments.* PNAS **1999** (96(18):10109–10114)

[18] R. Krautbauer, H. Clausen-Schaumann, H. E. Gaub. *Cisplatin Changes the Mechanics of Single DNA Molecules.* Angewandte Chemie International Edition **2000** (39(21):3912–3915)
DOI:10.1002/1521-3773(20001103)39:21<3912::AID-ANIE3912>3.0.CO;2-5

[19] C. Bustamante, S. B. Smith, J. Liphardt, D. Smith. *Single-molecule studies of DNA mechanics.* Current Opinion in Structural Biology **2000** (10(3):279–285)
DOI:10.1016/S0959-440X(00)00085-3

[20] I. Rouzina, V. A. Bloomfield. *Force-Induced Melting of the DNA Double Helix. 1. Thermodynamic Analysis.* Biophysical Journal **2001** (80(2):882–893)
DOI:10.1016/S0006-3495(01)76067-5

[21] I. Rouzina, V. A. Bloomfield. *Force-Induced Melting of the DNA Double Helix. 2. Effect of Solution Conditions.* Biophysical Journal **2001** (80(2):894–900)
DOI:10.1016/S0006-3495(01)76068-7

[22] M. C. Williams, I. Rouzina, J. R. Wenner, R. J. Gorelick, K. Musier-Forsyth, V. A. Bloomfield. *Mechanism for nucleic acid chaperone activity of HIV-1 nucleocapsid protein revealed by single molecule stretching.* PNAS **2001** (98(11):6121–6126)
DOI:10.1073/pnas.101033198

[23] R. Krautbauer, L. H. Pope, T. E. Schrader, S. Allen, H. E. Gaub. *Discriminating small molecule DNA binding modes by single molecule force spectroscopy.* FEBS Letters **2002** (510(3):154–158)
DOI:10.1016/S0014-5793(01)03257-4

[24] M. C. Williams, R. J. Gorelick, K. Musier-Forsyth. *Specific zinc-finger architecture required for HIV-1 nucleocapsid proteins nucleic acid chaperone function.* PNAS **2002** (99(13):8614–8619)
DOI:10.1073/pnas.132128999

[25] L. Poljak, S. M. Batson, D. Ficheux, B. P. Roques, J.-L. Darlix, E. Käs. *Analysis of NCp7-dependent Activation of HIV-1 cDNA Integration and its Conservation Among Retroviral Nucleocapsid Proteins.* Journal of Molecular Biology **2003**

(329(3):411–421)
DOI:10.1016/S0022-2836(03)00472-8

[26] K. Pant, R. L. Karpel, M. C. Williams. *Kinetic Regulation of Single DNA Molecule Denaturation by T4 Gene 32 Protein Structural Domains.* Journal of Molecular Biology **2003** (327(3):571–578)
DOI:10.1016/S0022-2836(03)00153-0

[27] C. Storm, P. C. Nelson. *Theory of high-force DNA stretching and overstretching.* Physical Review E **2003** (67:051906-1–12)
DOI:10.1103/PhysRevE.67.051906

[28] K. Pant, R. L. Karpel, I. Rouzina, M. C. Williams. *Mechanical Measurement of Single-molecule Binding Rates: Kinetics of DNA Helix-destabilization by T4 Gene 32 Protein.* Journal of Molecular Biology **2004** (336(4):851–870)
DOI:10.1016/j.jmb.2003.12.025

[29] K. Pant, R. L. Karpel, I. Rouzina, M. C. Williams. *Salt Dependent Binding of T4 Gene 32 Protein to Single and Double-stranded DNA: Single Molecule Force Spectroscopy Measurements.* Journal of Molecular Biology **2005** (349(2):317–330)
DOI:10.1016/j.jmb.2005.03.065

[30] P. T. Underhill, P. S. Doyle. *Alternative spring force law for bead-spring chain models of the worm-like chain.* Journal of Rheology **2006** (50(4):513–529)
DOI:10.1122/1.2206713

[31] R. Podgornik. *Polymer Physics: DNA off the Hooke.* Nature Nanotechnology **2006** (1(2):100–101)
DOI:10.1038/nnano.2006.114

[32] M. Cruceanu, M. A. Urbaneja, C. V. Hixson, D. G. Johnson, S. A. Datta, M. J. Fivash, A. G. Stephen, R. J. Fisher, R. J. Gorelick, J. R. Casas-Finet, A. Rein, I. Rouzina, M. C. Williams. *Nucleic acid binding and chaperone properties of HIV-1 Gag and nucleocapsid proteins.* Nucleic Acids Research **2006** (34(2):593–605)
DOI:10.1093/nar/gkj458

[33] M. Cruceanu, A. G. Stephen, P. J. Beuning, R. J. Gorelick, R. J. Fisher, M. C. Williams. *Single DNA molecule stretching measures the activity of chemicals that target the HIV-1 nucleocapsid protein.* Analytical Biochemistry **2006**

(358(2):159–170)
DOI:10.1016/j.ab.2006.08.037

[34] I. D. Vladescu, M. J. McCauley, M. E. Nuñez, I. Rouzina, M. C. Williams. *Quantifying force-dependent and zero-force DNA intercalation by single-molecule stretching.* Nature Methods **2007** (4(6):517–522)
DOI:10.1038/nmeth1044

[35] H. Labit, A. Goldar, G. Guilbaud, C. Douarche, O. Hyrien, K. Marheineke. *A simple and optimized method of producing silanized surfaces for FISH and replication mapping on combed DNA fibers.* BioTechniques **2008** (45(6):649–658)
DOI:DOI

[36] S. Bourbigot, N. Ramalanjaona, C. Boudier, G. F. J. Salgado, B. P. Roques, Y. Mély, S. Bouaziz, N. Morellet. *How the HIV-1 Nucleocapsid Protein Binds and Destabilises the (-)Primer Binding Site During Reverse Transcription.* Journal of Molecular Biology **2008** (383(5):1112–1128)
DOI:10.1016/j.jmb.2008.08.046

[37] S. Drobczynski, P. Hebraud, J.-P. Munch, S. Harlepp. *Design and realization of a high-stability optical tweezers.* Optical Engineering **2009** (48(11):113601–113605)
DOI:10.1117/1.3257269

[38] K. R. Chaurasiya, T. Paramanathan, M. J. McCauley, M. C. Williams. *Biophysical characterization of DNA binding from single molecule force measurements.* Physics of Life Reviews **2010** (7(3):299–341)
DOI:10.1016/j.plrev.2010.06.001

[39] M. Jalalirad, M. Laughrea. *Formation of immature and mature genomic RNA dimers in wild-type and protease-inactive HIV-1: Differential roles of the Gag polyprotein, nucleocapsid proteins NCp15, NCp9, NCp7, and the dimerization initiation site.* Virology **2010** (407(2):225–236)
DOI:10.1016/j.virol.2010.08.013

[40] T. Wu, S. A. K. Datta, M. Mitra, R. J. Gorelick, A. Rein, J. G. Levin. *Fundamental differences between the nucleic acid chaperone activities of HIV-1 nucleocapsid protein and Gag or Gag-derived proteins: Biological implications.* Virology **2010** (405(2):556–567)
DOI:10.1016/j.virol.2010.06.042

[41] J. V. Fritz, L. Briant, Y. Mély, S. Bouaziz, H. de Rocquigny. *HIV-1 viral protein r: from structure to function.* Future Virology **2010** (5(5):607–625)
DOI:10.2217/fvl.10.47

[42] J. G. Levin, M. Mitra, A. Mascarenhas, K. Musier-Forsyth. *Role of HIV-1 nucleo-capsid protein in HIV-1 reverse transcription.* RNA Biology **2010** (7(6):754–774)
DOI:10.4161/rna.7.6.14115

[43] R. F. Bruinsma
Physics of protein-DNA interaction
Departament of Physics and Astronomy, University of California; Institut-Lorenz for Theoretical Physics, Universiteit Leiden, **2002**

[44] A. Y. Grosberg, A. R. Khokhlov
Statistical Physics of Macromolecules
AIP Press **1994**
ISBN: 978-1-5639-6071-0

[45] W. Masters, V. E. Johnson, R. C. Kolodny
Human Sexuality, Fifth Edition
Allyn & Bacon **1997**
ISBN: 978-0-6734-6785-0

[46] M. C. Williams
Optical Tweezers: Measuring Piconewton Forces
Biophysical Society **2002**

[47] H. Lodish, A. Berk, P. Matsudaira, C. A. Kaiser, M. Krieger, M. P. Scott, L. Zipursky, J. Darnell
Molecular Cell Biology, 5th Edition
WHFreeman **2004**
ISBN: 978-07-16-74366-8

[48] P. C. Winter, G. I. Hickey, H. L. Fletcher
Genetyka. Krótkie wykłady (wyd. II) (Polish translation of Instant Notes Genetics)
Wydawnictwo Naukowe PWN **2006**
ISBN: 978-83-01-14259-9

[49] M. B. Jackson
Molecular and Cellular Biophysics

Cambridge University Press **2006**
ISBN: 978-05-21-62470-1

[50] J. M. Berg, L. Stryer, J. L. Tymoczko
Biochemia (wyd. III) (Polish translation of Biochemistry, Fifth edition)
Wydawnictwo Naukowe PWN **2007**
ISBN: 978-83-01-14379-4

[51] A. J. F. Griffiths, S. R. Wessler, R. C. Lewontin, S. B. Carroll
Introduction to Genetic Analysis, 9th Edition
W. H. Freeman **2007**
ISBN: 978-07-16-76887-6

[52] B. Alberts, A. Johnson, J. Lewis, M. Raff, K. Roberts, P. Walter
Molecular Biology of the Cell, Fifth Edition
Garland Science **2007**
ISBN: 978-0-8153-4105-5

[53] B. J. Kirby
Micro- and Nanoscale Fluid Mechanics, Transport in Microfluidic Devices
Cambridge University Press **2010**
ISBN: 978-05-21-11903-0

[54] http://www-lbp.unistra.fr/equipe-biophotonique/
Proteines-virales-structures-et/Proteine-de-la-nucleocapside-de/

Laponite

[55] D. Axelrod, T. P. Burghardt, N. L. Thompson. *Total Internal Reflection Fluorescence.* Annual Review of Biophysics and Bioengineering **1984** (13:247–268)
DOI:10.1146/annurev.bb.13.060184.001335

[56] D. W. Thompson, J. T. Butterworth. *The Nature of Laponite and Its Aqueous Dispersions.* Journal of Colloid and Interface Science **1992** (151(1):236–243)
DOI:10.1016/0021-9797(92)90254-J

[57] T. G. Mason, D. A. Weitz. *Optical Measurements of Frequency-Dependent Linear Viscoelastic Moduli of Complex Fluids.* Physical Review Letters **1995** (74(7):1250–

1253)
DOI:10.1103/PhysRevLett.74.1250

[58] A. Mourchid, E. Lécolier, H. Van Damme, P. Levitz. *On Viscoelastic, Birefringent, and Swelling Properties of Laponite Clay Suspensions: Revisited Phase Diagram.* Langmuir **1998** (14(17):4718–4723)
DOI:10.1021/la980117p

[59] A. Knaebel, M. Bellour, J.-P. Münch, V. Viasnoff, F. Lequeux, J. L. Harden. *Aging behavior of Laponite clay particle suspensions.* Europhysics Letters **2000** (52(1):73–79)
DOI:10.1209/epl/i2000-00406-6

[60] A. J. Levine, T. C. Lubensky. *One- and Two-Particle Microrheology.* Physical Review Letters **2000** (85(8):1774–1777)
DOI:10.1103/PhysRevLett.85.1774

[61] L. Cipelletti, S. Manley, R. C. Ball, D. A. Weitz. *Universal Aging Features in the Restructuring of Fractal Colloidal Gels.* Physical Review Letters **2000** (84(10):2275–2278)
DOI:10.1103/PhysRevLett.84.2275

[62] B. Abou, D. Bonn, J. Meunier. *Aging dynamics in a colloidal glass.* Physical Review E **2001** (64(2):021510-1–6)
DOI:10.1103/PhysRevE.64.021510

[63] M. Bellour, A. Knaebel, J. L. Harden, F. Lequeux, J.-P. Munch. *Aging processes and scale dependence in soft glassy colloidal suspensions.* Physical Review E **2003** (67(3):031405-1–8)
DOI:10.1103/PhysRevE.67.031405

[64] F. Ozon, T. Narita, A. Knaebel, G. Debrégeas, P. Hébraud, J.-P. Munch. *Partial rejuvenation of a colloidal glass.* Physical Review E **2003** (68(3):032401-1–4)
DOI:10.1103/PhysRevE.68.032401

[65] A. B. Morgan, L.-L. Chu, J. D. Harris. *A flammability performance comparison between synthetic and natural clays in polystyrene nanocomposites.* Fire and Materials **2004** (29:213–229)
DOI:10.1002/fam.881

[66] M. T. Valentine, Z. E. Perlman, M. L. Gardel, J. H. Shin, P. Matsudaira, T. J. Mitchison, D. A. Weitz. *Colloid Surface Chemistry Critically Affects Multiple Particle Tracking Measurements of Biomaterials.* Biophysical Journal **2004** (86(6):4004–4014)
DOI:10.1529/biophysj.103.037812

[67] B. Ruzicka, L. Zulian, G. Ruocco. *Routes to Gelation in a Clay Suspension.* Physical Review Letters **2004** (93(25):258301-1–4)
DOI:10.1103/PhysRevLett.93.258301

[68] S. Kaloun, M. Skouri, A. Knaebel, J.-P. Münch, P. Hébraud. *Aging of a colloidal glass under a periodic shear.* Physical Review E **2005** (72(1):011401-1–5)
DOI:10.1103/PhysRevE.72.011401

[69] P. Mongondry, J. F. Tassin, T. Nicolai. *Revised state diagram of Laponite dispersions.* Journal of Colloid and Interface Science **2005** (283(2):397–405)
DOI:10.1016/j.jcis.2004.09.043

[70] S. Kaloun, R. Skouri, M. Skouri, J. P. Munch, F. Schosseler. *Successive exponential and full aging regimes evidenced by tracer diffusion in a colloidal glass.* Physical Review E **2005** (72(1):011403-1–5)
DOI:10.1103/PhysRevE.72.011403

[71] F. Schosseler, S. Kaloun, M. Skouri, J. P. Munch. *Diagram of the aging dynamics in laponite suspensions at low ionic strength.* Physical Review E **2006** (73(2):021401-1–9)
DOI:10.1103/PhysRevE.73.021401

[72] B. Ruzicka, L. Zulian, G. Ruocco. *More on the Phase Diagram of Laponite.* Langmuir **2006** (22(3):1106–1111)
DOI:10.1021/la0524418

[73] B. Ruzicka, L. Zulian, R. Angelini, M. Sztucki, A. Moussaïd, G. Ruocco. *Arrested state of clay-water suspensions: Gel or glass?.* Physical Review E **2008** (77(2):020402-1–4)
DOI:10.1103/PhysRevE.77.020402

[74] S. Jabbari-Farouji, H. Tanaka, G. H. Wegdam, D. Bonn. *Multiple nonergodic disordered states in Laponite suspensions: A phase diagram.* Physical Review E **2008**

(78(6):061405-1–10)
DOI:10.1103/PhysRevE.78.061405

[75] L. Petit, C. Barentin, J. Colombani, C. Ybert, L. Bocquet. *Size Dependence of Tracer Diffusion in a Laponite Colloidal Gel.* Langmuir **2009** (25(20):12048–12055)
DOI:10.1021/la901244v

[76] B. Ruzicka, L. Zulian, E. Zaccarelli, R. Angelini, M. Sztucki, A. Moussaïd, G. Ruocco. *Competing Interactions in Arrested States of Colloidal Clays.* Physical Review Letters **2010** (104(8):085701-1–4)
DOI:10.1103/PhysRevLett.104.085701

[77] B. Ruzicka, E. Zaccarelli, L. Zulian, R. Angelini, M. Sztucki, A. Moussaïd, T. Narayanan, F. Sciortino. *Observation of empty liquids and equilibrium gels in a colloidal clay.* Nature Materials **2011** (10(1):56–60)
DOI:10.1038/nmat2921

[78] B. Ruzicka, E. Zaccarelli. *A fresh look at the Laponite phase diagram.* Soft Matter **2011** (7(4):1268–1286)
DOI:10.1039/c0sm00590h

[79] Eds. F. Bergaya, B. K. G. Theng, G. Lagaly
Handbook of Clay Science
Elsevier Science **2006**
ISBN: 978-0-08-044183-2

[80] H. H. Murray
Applied Clay Mineralogy
Elsevier Science **2007**
ISBN: 978-0-44-451701-2

[81] V. Viasnoff
Influence d'un cisaillement oscillant sur la dynamique microscopique de vieillissement d'un verre colloïdal
Université Paris VI - Pierre et Marie Curie, Paris, France, **2003**

[82] P. Mongondry
Structure et comportement rhéologique des suspensions aqueuses de Laponite en présence de plusieurs additifs
Université du Maine, Le Mans, France, **2003**

[83] S. Kaloun

Vieillissement d'un verre colloïdal. Variations sur les techniques de diffusion de la lumière.

Université Cadi Ayyad, Semlalia-Marrakech, Morocco and Université Louis Pasteur, Strasbourg, France, **2005**

[84] F. Ianni

Complex behavior of colloidal suspensions under shear: dynamics investigation through light scattering techniques

Università "La Sapienza" Di Roma, Italy and Université Paris VI, France, **2007**

[85] R. Sarcia

Suspensions colloïdales concentrées sous contrainte

Université Paris VI - Pierre et Marie Curie, Paris, France, **2007**

[86] http://www.scprod.com/pdfs/LaponiteTechnologyFeb2010.pdf

Piotr Marek KLAJNER

**Experimental study of the kinetics of two systems:
DNA complexation by the NCp7 protein and probe
dynamics in a glassy colloidal suspension**

Résumé

Dans la première partie de cette thèse, nous étudions la cinétique de la complexation d'un double brin d'ADN par la protéine NCp7. Pour ce faire, nous étudions l'évolution des propriétés mécaniques de l'ADN au fur et à mesure de sa complexation, en étirant la complexe ADN/NCp7 à l'aide d'un montage de piégeage optique. Nous avons observé que la longueur de persistance du complexe diminue au fur et à mesure de la complexation. En utilisant un modèle statistique décrivant l'évolution de la flexibilité de l'ADN complexé par NCp7. Notre principal résultat est que la fraction //phi de paires de bases ayant réagi n'est pas une fonction linéaire du temps aux faibles //phi. Nous interprétons nos résultats en supposant que l'adsorption de NCp7 sur l'ADN est fortement coopérative. Dans deuxième chapitre, nous décrivons la dynamique de particules sondes dans une suspension vitreuse colloïdale de Laponite. La Laponite est une particule colloïdale discoïdale de 25 nm de diamètre et de 0.92 nm d'épaisseur. Nous utilisons une expérience de microscopie en onde évanescente, et suivons le mouvement de particules fluorescentes de latex. Nous imageons ensuite ces particules. Nous montrons que, pour un mouvement possédant une seule échelle de temps caractéristique, elle est simplement une fonction linéaire du temps. Nous obtenons que, quelle que soit leur taille, le mouvement des particules sondes peut être décrit par une succession de deux modes dynamiques, où le mode le plus rapide correspond à la diffusion des particules dans un fluide viscoélastique.

Résumé en anglais

In the first part of this thesis, we study the kinetics of the complexation of a double-stranded DNA by NCp7 protein. To do this, we study the evolution of mechanical properties of DNA and its complexation by stretching the DNA/NCp7 complex with a optical trap. We observed that the persistence length of the complex decreases progressively during the complexation. Using a statistical model we describe the evolution of the flexibility of DNA complexed with NCp7. Our main result is that the fraction phi of base pairs that have reacted is not a linear function of time at low phi. We interpret our results assuming that the adsorption of NCp7 on DNA is highly cooperative. In the second chapter, we describe the dynamics of probe particles in a colloidal glassy suspension of Laponite. Laponite is a colloidal discoidal particle of 25 nm in diameter and 0.92 nm thick. We take advantage of evanescent wave microscopy, and follow the movement of fluorescent latex particles. Then we image these particles. We show that for a movement that has a single characteristic time scale, it is simply a linear function of time. We find that, whatever their size, the motion of probe particles can be described by a succession of two dynamic modes, where the fastest mode corresponds to the diffusion of particles in a viscoelastic fluid.